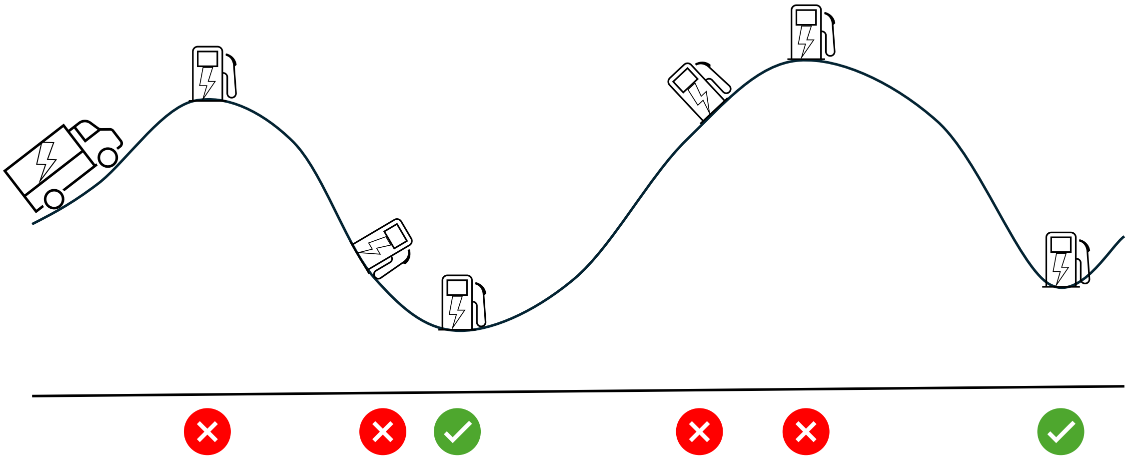

Hierarchical Optimization for Charge Planning and Thermal Management of Battery Electric Trucks

Master's thesis in Systems, Control, and Mechatronics

ISAC BORGHED

DEPARTMENT OF ELECTRICAL ENGINEERING

CHALMERS UNIVERSITY OF TECHNOLOGY
Gothenburg, Sweden 2024
www.chalmers.se

Master's thesis 2024

Hierarchical Optimization for Charge Planning and Thermal Management of Battery Electric Trucks

ISAC BORGHED

Department of Electrical Engineering
Division of Systems and Control
Chalmers University of Technology
Gothenburg, Sweden 2024

Hierarchical Optimization for Charge Planning and Thermal Management of Battery Electric Trucks
ISAC BORGHED

Supervisors: Olof Lindgärde, Saurabh Suman, AB Volvo
Examiner: Nikolce Murgovski, Department of Electrical Engineering

Master's Thesis 2024
Department of Electrical Engineering
Division of Systems and Control
Chalmers University of Technology
SE-412 96 Gothenburg
Telephone +46 31 772 1000

Cover: Illustration of the charge planning problem for battery electric trucks.

Typeset in LaTeX
Printed by Chalmers Reproservice
Gothenburg, Sweden 2024

Hierarchical Optimization for Charge Planning and Thermal Management of Battery Electric Trucks
ISAC BORGHED
Department of Electrical Engineering
Chalmers University of Technology

Abstract

To meet the climate goals set by the UN and the EU the shift from vehicles driven by fossil fuels to zero- and low-emission vehicles (ZLEV) needs to be accelerated. One such focus area is the adoption of battery-electric vehicles (BEVs). At the moment, electric trucks suffer from a range disadvantage compared to internal combustion engine (ICE) trucks, and since the recharging times are long the optimal planning of charging becomes a complex logistical problem. In this thesis the problem of optimal charge planning and thermal management for a specific route and speed profile is studied, where the objective of the optimization is to minimize the total cost of operation (TCOP), taking into consideration stochastic uncertainties such as traffic speed and charging station queuing times. The optimization problem is formulated as a mixed-integer nonlinear programming (MINLP) problem, which is solved by decomposing the problem into two layers. The top layer is solved using stochastic dynamic programming (SDP) for a simplified version of the MINLP. The charging decisions found using SDP are sent to the lower layer which can then be formulated as a nonlinear programming (NLP) problem which is solved using the FORCESPRO NLP solver using a more comprehensive model of the truck's dynamics. The mission planner is evaluated on a 460 km route and a 660 km route, with both including recharging stations. It is found that the hierarchical mission manager reduces costs by up to 7.8% compared to a previously developed mission manager which simplified the MINLP to an NLP using a sigmoid activation function to represent charging decisions. The hierarchical solver has also been found to improve the solution's robustness and can consider time-varying disturbances such as traffic speed and charging prices.

Keywords: Mixed integer nonlinear optimization, Stochastic optimal control, Battery electric vehicles.

Acknowledgements

First and foremost I would like to express my most sincere gratitude to my supervisors at AB Volvo, Olof Lindgärde and Saurabh Suman. Throughout the whole thesis work they have always provided great support and advice. Their insight and experience in the area of energy management has provided me with motivation and inspired me to investigate the many interesting areas which have been covered in this project. I would also like to thank my examiner at Chalmers, Professor Nikolce Murgovski, for providing his invaluable experience in numerical optimal control theory and for providing his continuous assistance. Finally I would also like to thank my fellow master thesis students at AB Volvo, Ilya Kuangaliyev and Oscar Mark, for their fantastic cooperation and the many insightful discussions we have had.

Isac Borghed, Gothenburg, June 2024

List of Acronyms

Below is the list of acronyms that have been used throughout this thesis listed in alphabetical order:

BEV	Battery Electric Vehicle
BMU	Battery Management Unit
CI	Confidence Interval
COP21	UN Climate Change Conference 2021
DP	Dynamic Programming
DDP	Deterministic Dynamic Programming
EM	Electric Motor
EU	European Union
EV	Electric Vehicle
EVRP	Electric Vehicle Routing Problem
FCEV	Fuel Cell Electric Vehicle
FONC	First Order Necessary Condition for optimality
GHG	Greenhouse Gases
GK	Genoa Karlsruhe route
GR	Gothenburg Rødby route
GVRP	Green Vehicle Routing Problem
HEV	Hybrid Electric Vehicle
ICE	Internal Combustion Engine
IP	Interior Point method
KKT	Karush-Kuhn-Tucker optimality conditions
LEV	Low Emission Vehicle
LICQ	Linear Independence Constraint Qualification
LTO	Lithium Titanium Oxide
MDP	Markov Decision Process
MILP	Mixed Integer Linear Program
MINLP	Mixed Integer Nonlinear Program
MIP	Mixed Integer Program
MPC	Model Predictive Control
NLP	Nonlinear Program
NMPC	Nonlinear Model Predictive Control
OCP	Optimal Control Problem
ODE	Ordinary Differential Equation

PDIP	Primal-Dual Interior Point method
RC	Resistance Capacitance model
RMSE	Root Mean Squared Error
RHC	Receding Horizon Control
SBRB	School Bus Routing Problem
SDP	Stochastic Dynamic Programming
SMPC	Stochastic Model Predictive Control
SoC	Battery State of Charge
SoE	Battery State of Energy
SQP	Sequential Quadratic Programming
TCOP	Total Cost of Operation
PEM	Predictive Energy Management
PMP	Pontryagin Minimum Principle
ZEV	Zero Emission Vehicle
ZLEV	Zero and Low Emission Vehicles
QP	Quadratic Program
VRP	Vehicle Routing Problem

Nomenclature

Below is the nomenclature of indices, functions, sets, parameters, and variables that have been used throughout this thesis listed in alphabetical order.

Indices

i	Charging station index
k	Stage index in the OCP
N	Total number of stages in the OCP
N_{chg}	Total number of charging stations
n	Total number of optimization variables
n_{soc}	Number of discretized SoC states
n_{tchg}	Number of discretized charging time samples
n_u	Number of OCP control inputs
n_w	Number of stochastic variables
n_x	Number of OCP states
m	Number of inequality constraints
p	Number of equality constraints
s	Space sample in the OCP
s_i	Space sample of charging station i
s_i^+	Space sample of charging station i, vehicle leaving station
s_0	Initial space sample
s_N	Final space sample

Functions

$\boldsymbol{\pi}(\cdot)$	OCP policy
$\mu(\cdot)$	OCP control function

$\mathbf{f}(\cdot)$	State dynamics
$\mathbf{g}(\cdot)$	Inequality constraints
$\mathbf{h}(\cdot)$	Equality constraints
$J(\cdot)$	Objective function to minimize
$J_{\boldsymbol{\pi}}(\cdot)$	OCP objective function for policy $\boldsymbol{\pi}$
$J_N(\cdot)$	Final stage cost
$\mathcal{L}(\cdot)$	Lagrangian function
$l(\cdot)$	Stage objective function
$\mathcal{N}(\cdot)$	Gaussian distribution
$\mathrm{Pois}(\cdot)$	Poisson distribution
$\mathrm{Pr}(\cdot)$	Probability mass
$p(\cdot)$	Probability density
$V_{\boldsymbol{\pi}}(\cdot)$	OCP Value function for policy $\boldsymbol{\pi}$

Sets

Π	Set of possible OCP policies
Ω	Probability sample space
$\mathcal{A}$	Index set of active inequality constraints
$\mathscr{F}$	Probability event space
$\mathcal{I}$	Set of charging stations
$\mathcal{N}$	Set of neighboring points
$\mathcal{S}$	Set of all space samples
$\mathcal{S}_{chg}$	Set of space samples which contains a charging station
$\mathcal{S}_{drv}$	Set of space samples which do not contain a charging station
$\mathcal{T}$	Feasible set of time
$\mathcal{T}_{chg}^{i}$	Set of time instances during charging at station i
$\mathcal{T}_{drv}$	Set of time instances during driving
$\mathcal{U}$	Control input constraints in the OCP
$\mathcal{W}$	Value set of stochastic disturbance $\mathbf{w}$
$\mathcal{X}$	Set of feasible states in the OCP
$\mathcal{X}_0$	Feasible initial states in the OCP
$\mathcal{X}_N$	Feasible terminal states in the OCP
$\mathcal{Z}$	Set feasible optimization variables

Parameters

α	Road gradient	[rad]
$\Delta\tau$	Normalized charging time discretization step size	[$\cdot$]
ε	Mission maximum risk of failure	[$\cdot$]
η_c	Battery Coloumbic efficiency	[$\cdot$]
$\eta_{EM}(v, F_T)$	Electric motor efficiency	[$\cdot$]
η_{tm}	Transmission efficiency	[$\cdot$]
θ	Vehicle heading	[rad]
θ_{wind}	Wind direction	[rad]
κ	KKT tolerances	[$\cdot$]
$\boldsymbol{\lambda}_q$	Average queuing times at stations	[s]
$\boldsymbol{\mu}_v$	Average velocity disturbances	[m/s]
$\boldsymbol{\Sigma}_v$	Variance of velocity disturbance	[$(\text{m/s})^2$]
ρ_a	Air density	[kg/m^3]
$\text{CdA}(\beta)$	Air drag and frontal area spline	[m^2]
$C_1, C_2(\text{soc}, T_b)$	Battery internal capacitances	[F]
C_b	Maximum capacity of battery	[Ah]
C_{rr}	Rolling resistance coefficient	[$\cdot$]
c_δ	Cost of constraint violation	[SEK]
c_ζ	Cost of stopping at charging station	[SEK]
c_b	Cost of friction brake usage	[SEK/N^2]
$c_c^i(t)$	Time and station dependent charging cost	[SEK/kWh]
c_{cr}	Cost on C-rate during charging	[SEK/CK^2]
c_d	Cost of driving	[SEK/m]
$c_{p,b}$	Specific heat of battery	[J/(kgK)]
c_t	Time cost	[SEK/s]
E_{cap}	Battery energy capacity	[J]
$F_T^{max}(v)$	Maximum traction effort at velocity v	[N]
$F_T^{min}(v)$	Minimum traction effort at velocity v	[N]
g	Gravitational acceleration	[m/s^2]
L_{detour}	Charging station detour distance	[m]
L_s	Spatial sampling distance	[m]
m	Total vehicle mass	[kg]

m_b	Battery mass	[kg]
m_e	Vehicle equivalent mass including inertia	[kg]
n_p	Number of battery cells in parallel	[$\cdot$]
n_s	Number of battery cells in series	[$\cdot$]
P_{aux}	Auxiliary power consumption	[W]
$P_{b,ch}^{min}$	Battery minimum power input	[W]
$P_{b,dch}^{max}$	Battery maximum power output	[W]
P_{chg}^{max}	Vehicle maximum charging power	[W]
$P_{hc}(T_b, T_b^{ref})$	Power consumption of the thermal system	[W]
$P_{stat,i}^{max}$	Maximum charging power capacity of station i	[W]
q_i	Queuing time at station i	[s]
$R_0, R_1, R_2(\text{soc}, T_b)$	Battery internal resistances	[Ω]
R_{eq}	Battery cell equivalent resistance	[Ω]
r_{eff}	Effective tire radius	[m]
$r_{EM}(\gamma)$	Gear ratio of motor at gear γ	[$\cdot$]
r_{tm}	Transmission gear ratio	[$\cdot$]
soc^{max}	Maximum battery SoC	[$\cdot$]
soc^{min}	Minimum battery SoC	[$\cdot$]
soc_N^{min}	Minimum final battery SoC	[$\cdot$]
T_{amb}	Ambient temperature	[K]
T_b^{max}	Maximum battery temperature	[K]
T_b^{min}	Minimum battery temperature	[K]
t^{max}	Maximum trip time	[s]
t_{chg}^{max}	Maximum charging time	[s]
t_N	Arrival time	[s]
$u_{oc}(\text{soc}, T_b)$	Battery open-circuit voltage	[V]
$V_N(\text{soc})$	Terminal cost	[SEK]
V_{max}	Maximum cost	[SEK]
v	Vehicle longitudinal velocity	[m/s]
v_{wind}	Wind speed	[m/s]

Variables

β	Wind angle of impact	[rad]

γ	Selected gear	$[\cdot]$
Δt	Time difference between succeeding stages	[s]
δ	Arbitrary slack variables	$[\cdot]$
ζ	Charging decision variable	$[\cdot]$
τ	IP method barrier parameter	$[\cdot]$
τ_{EM}	EM torque	[Nm]
τ	Normalized charging time	$[\cdot]$
ω_{EM}	EM angular velocity	[rad/s]
ω_w	Wheel angular velocity	[1/s]
C_r	Battery C-rate	[C]
d_{EM}	Direction of EM operation	$[\cdot]$
E_{chg}	Total charged energy	[J]
E_{con}	Total consumed energy	[J]
F_{air}	Air resistance force	[N]
F_{brake}	Vehicle braking force using disc brakes	[N]
F_g	Gravitational force	[N]
F_{grad}	Slope gradient force	[N]
F_{rr}	Rolling resistance force	[N]
F_T	Wheel traction force	[N]
$F_{T,loss}$	Traction force losses in the EM	[N]
H	Battery throughput	[J]
$i_1.i_2, i_3, i_4$	Battery internal currents	[A]
i	Battery cell current	[A]
i_b	Battery current	[A]
P_b	Battery power output	[W]
$P_{b,cell}$	Total cell power	[W]
$P_{b,loss}$	Battery power losses	[W]
$P_{b,loss,cell}$	Cell power losses	[W]
$P_{b,tot}$	Total battery power	[W]
P_{EM}	Propulsive power of the EM	[W]
P_{stat}	Charging power	[W]
Q	Battery charge level	[C]
Q_{act}	Thermal system heat flow	[W]
Q_{gen}	Generated battery heat from losses	[W]

soc	Battery State of Charge	[·]
T_b	Battery temperature	[°C]
T_b^{ref}	Thermal system reference temperature	[°C]
t	Time	[s]
t_0	Departure time	[s]
t_{chg}	Charging time	[s]
u_1, u_2	Battery internal voltages	[V]
u_b	Battery voltage	[V]
u_t	Battery cell terminal voltage	[V]
v_{rel}	Relative wind speed	[m/s]

Contents

List of Acronyms ix

Nomenclature xi

List of Figures xix

List of Algorithms xxv

List of Tables xxvii

1 Introduction 1
- 1.1 Literature review 2
  - 1.1.1 Electric vehicle routing problem 2
  - 1.1.2 Mission management 4
- 1.2 Purpose 6
- 1.3 Limitations 7
- 1.4 Research questions 7

2 Modeling 9
- 2.1 Vehicle dynamics 9
- 2.2 Powertrain structure 10
  - 2.2.1 Battery modeling 11
  - 2.2.2 Mechanical modeling 16
  - 2.2.3 Thermal modeling 19

3 Optimal control theory 21
- 3.1 Deterministic optimal control 21
  - 3.1.1 Nonlinear optimization 22
  - 3.1.2 Interior point methods 23
  - 3.1.3 Multiple shooting 25
- 3.2 Stochastic optimal control 25
  - 3.2.1 Stochastic decision models 25
  - 3.2.2 Stochastic dynamic programming 26

4 Problem formulation 27
- 4.1 Continuous time problem formulation 27
- 4.2 Hybrid dynamical system formulation 30

4.2.1 Driving mode . . . 31
4.2.2 Charging mode . . . 32
4.3 Bounds on inputs and variables . . . 33
4.4 Objective function . . . 33
4.4.1 Driving mode . . . 33
4.4.2 Charging mode . . . 34
4.5 Full optimization problem . . . 34
4.6 Hierarchical formulation . . . 35
4.6.1 Upper level - station selection . . . 35
4.6.2 Lower level - battery management . . . 39
4.7 Stochastic parameters . . . 40
4.8 Discretization . . . 40

5 Simulation setup 43
5.1 Full solver evaluation . . . 44
5.1.1 Gothenburg-Rødby . . . 47
5.1.2 Genoa-Karlsruhe . . . 49
5.1.3 Stochastic disturbances . . . 50
5.2 Model mismatch evaluation . . . 50
5.3 Station selection evaluation . . . 51
5.4 Battery health evaluation . . . 51

6 Simulation results 53
6.1 Evaluation of full hierarchical solver . . . 53
6.1.1 Gothenburg-Rødby . . . 53
6.1.2 Genoa-Karlsruhe . . . 54
6.2 Evaluation of station selection layer . . . 56
6.3 Model mismatch evaluation . . . 60
6.4 Battery health evaluation . . . 63

7 Discussion 65
7.1 Full solver evaluation . . . 65
7.2 Robustness . . . 66
7.3 Battery health . . . 68
7.4 Vehicle dynamics . . . 68
7.5 Powertrain models . . . 69
7.6 Numerical optimization . . . 69
7.6.1 Convergence . . . 69
7.6.2 Computation times . . . 71
7.7 Simulation . . . 71

8 Conclusion 73

Bibliography 75

A Gothenburg-Rødby simulation plots I

B Genoa-Karlsruhe simulation plots IX

List of Figures

2.1 Different forces acting on a truck, red arrows represent external forces, blue arrows represent vehicular forces. The acceleration vector is represented by the green arrow. 9
2.2 Simplified schematic diagram of the studied electric powertrain, describing the electric power flow between the different electrical components in the truck. 11
2.3 Equivalent circuit used to model the battery cells. 11
2.4 **(a)**: Battery discharging open circuit voltage, dependent on the battery SoC soc and temperature T_b. **(b)**: Battery charging open circuit voltage, dependent on the battery SoC soc and temperature T_b. . . . 13
2.5 **(a)**: Battery discharging internal resistance, dependent on the battery SoC and temperature T_b. **(b)**: Battery charging internal resistance, dependent on the battery SoC and temperature T_b. 14
2.6 **(a)**: Battery maximum discharging power, dependent on the battery SoC soc and temperature T_b. **(b)**: Absolute value of minimum battery charging power, dependent on the battery SoC soc and temperature T_b. 17
2.7 EM efficiency map for feasible pairs of motor torque and RPM. . . . 18
2.8 **(a)**: Speed and traction effort dependent optimal gear map as well as lower (blue) and upper (red) bounds on traction effort, $F_T^{min}(v)$ and $F_T^{max}(v)$. **(b)**: EM efficiency at optimal gear selection as well as lower (blue) and upper (red) bounds on traction effort, $F_T^{min}(v)$ and $F_T^{max}(v)$. 20

3.1 Schematic illustration of solutions to the barrier problem in (3.13) for smoothing parameters $\tau \in \{0.01, 0.1, 0.5, 1, 2\}$. The true cost function is given by $f(z) = 3(z-1)^3$ and it is optimized over the bounds $0 \leq z \leq 1$. Its optimum is given by $z^* = 0$, and for each τ the approximate solutions z_τ^* are shown alongside their respective approximate cost functions $f_\tau(z)$. 24

4.1 Illustration of the hybrid dynamics used in the optimization problem. 30
4.2 Hierarchical decomposition of the mission management optimization problem, showing the two layers and their states, inputs and outputs as well as the sampling structures and the solutions strategies of each layer. 35

5.1 Charging price multiplier depending on the time of day. The charging price is 20% higher during peak power demand and 20% lower during off-peak demand. 44
5.2 Topographical relief maps of the routes which are studied in this thesis. Both maps are made available by OpenStreetMap contributors [59], retrieved from `https://www.openstreetmap.org/` on 2024-04-23. ODbL. 46
5.3 Altitude profile and speed limits of the Gothenburg-Rødby route. The locations of the charging stations listed in table 5.1 are shown as green dots in the plot. 47
5.4 Updated speed limits compared to original speed limits for the Gothenburg-Rødby route. 48
5.5 Altitude profile and speed limits of the Genoa-Karlsruhe route. The locations of the charging stations listed in table 5.2 are shown as green dots in the plot. 49
5.6 Updated speed limits compared to original speed limits for the Genoa-Karlsruhe route. 49

6.1 Plot of the time-varying speed limit for the GR route with the different trip time trajectories for disturbance cases a-c described in section 5.1 represented by the red area plot. 54
6.2 Plot of the time-varying speed limit for the GK route with the different trip time trajectories for disturbance cases a-c described in section 5.1 represented by the red area plot. 55
6.3 Speed and SoC trajectory outputs from the upper layer for the GR route with time-dependent charging prices and **(a)** soc(0) = 0.85, **(b)** soc(0) = 0.7. Each case is simulated 10 times and the means and 95% CIs of the trajectories are plotted. 56
6.4 Speed and SoC trajectory outputs from the upper layer for the GR route with time-dependent charging prices and **(a)** soc(0) = 0.55, **(b)** soc(0) = 0.4. Each case is simulated 10 times and the means and 95% CIs of the trajectories are plotted. 57
6.5 Surface plot of the value function in the station selection layer with SoC trajectories for initial SoC levels 40%, 55%, 70%, and 85%. . . . 58
6.6 Illustration of the charging time policy in the station selection layer with SoC trajectories for initial SoC levels 40%, 55%, 70%, and 85%. The color of the graph represents the charging power capacities of the stations in table 5.1. 59
6.7 Plot of the time mapping resulting from using the policy in 6.6 and the final time $t_N = 17.00$ with plots of SoC trajectories for initial SoC levels 40%, 55%, 70% and 85%. The transparent regions of the plot represent regions of infeasibility. 59
6.8 The departure time using the optimal policy shown in figure 6.6 with initial time shown for SoC levels 40%, 55%, 70% and 85%. 60

6.9 Plot SoC and battery temperature mean and 95% CI from the 100 simulations on the GR route including the model mismatch described in section 5.2, plotted against the SoC and temperature trajectories given control inputs from the FORCESPRO solver output. The absolute error plots represent the absolute distance between the mean state trajectory and the simulation output in each stage, and the size of the 95% CI is plotted in the same graphs. The hierarchical solution was used in **(a)** and the sigmoid approximation was used in **(b)**. . . . 61

6.10 Plots of SoC and battery temperature mean and 95% CI from the 100 simulations on the GK route using the erroneous plant model described in section 5.2, plotted against the SoC and temperature trajectories given control inputs from the FORCESPRO solver output. The absolute error plots represent the absolute distance between the mean state trajectory and the simulation output in each stage, and the size of the 95% CI is plotted in the same graphs. The hierarchical solution was used in **(a)** and the sigmoid approximation was used in **(b)**. 62

6.11 C-rate and battery temperature trajectories during charging for the **(a)** GR route, **(b)** GK route. Two simulations are plotted for each route, one where the C-rate is included in the cost function (represented by the fully drawn lines, case 1) and one without it (represented by the dashed lines, case 2). 63

7.1 Infinity norm of the equality constraint residuals (`res_eq`), the inequality constraint residuals (`res_ineq`), the stationarity condition (`rsnorm`) and the complementarity condition violations (`rcompnorm`) for each solver iteration during optimization on the GK route. It can be noted that the residuals more or less stop converging after about ~ 350 iterations. 70

7.2 Comparison of state trajectories from the multiple-shooting simulation output of the FORCESPRO solver and a single-shooting simulation using the same plant model and optimal control inputs. 70

A.1 Altitude profile, speed limits, and truck speed for the GR route. The optimal charging station is marked green in the plots, representing station 7 in table 5.1, the other station locations are shown as the unfilled black markers. Sub figures **(a)**-**(c)** represent the disturbance cases a-c which are described in section 5.1. II

A.2 Battery power and SoC trajectories for the GR route with no time-dependent parameters. Sub figures **(a)**-**(c)** represent the disturbance cases a-c which are described in section 5.1. The optimal solutions are to charge for 51, 53.2 respectively 41.2 minutes at station 7, where the queuing time is 14.4, 17.9 respectively 11 minutes. III

A.3 Traction effort, friction brake usage, battery temperature, and heat flow for the GR route. Friction brake usage is minimal for this case and the temperature is mostly kept around 24 − 25 °C. Sub figures **(a)**-**(c)** represent the disturbance cases a-c which are described in section 5.1. IV

A.4 Plots of the charging power, battery SoC, and temperature for the GR route. The plots are the state and input trajectories during charging at the selected station at 265 km. Sub figures **(a)**-**(c)** represent the disturbance cases a-c which are described in section 5.1. V

A.5 Speed, battery, and temperature profiles for GR route using the sigmoid approximation to solve the problem. Note that the solution in this case is to instead charge for 20.6 minutes at station 4 and 33.6 minutes at station 7. The sigmoid solution does not include charging dynamics and thus the station profile is not present. VI

A.6 Speed, battery, and temperature profiles for LR route using the heuristics algorithm to solve the problem. The suggested solution in this case is to charge for 80 minutes at station 12. The heuristics solution does not include charging dynamics and thus the station profile is not present. VII

B.1 Altitude profile, speed limits, and truck speed for the GK route. The optimal charging stations are marked green in the plot, representing stations 10 and 22 in table 5.2, the other station locations are shown as the unfilled black markers. Sub figures **(a)**-**(c)** represent the disturbance cases a-c which are described in section 5.1. X

B.2 Battery power and SoC trajectories for the GK route. Sub figures **(a)**-**(c)** represent the disturbance cases a-c which are described in section 5.1. It is optimal to charge for 55.1, 47 respectively 38.9 minutes at station 10, where the queuing time is 36.47, 41.9 respectively 31 minutes, and for 43.3, 48.3 respectively 45.7 minutes at station 22, where the queuing time is 30, 35 respectively 25 minutes. XI

B.3 Traction effort, friction brake usage, battery temperature, and heat flow for the GK route. It can be noted that the friction brake usage is minimal for this case and that the temperature is mostly kept around 24 − 25 °C. Sub figures **(a)**-**(c)** represent the disturbance cases a-c which are described in section 5.1. XII

B.4 Plots of the charging power, battery SoC, and temperature for the GK route. The plots are the state and input trajectories during charging at the selected stations at 236 and 566 km. Sub figures **(a)**-**(c)** represent the disturbance cases a-c which are described in section 5.1. XIII

B.5 Speed, battery, and temperature profiles for GK route using the sigmoid approximation to solve the problem. Note that the solution in this case is to instead charge for 82.4 minutes at station 10, 24.9 minutes at station 13 and 13.2 minutes at station 23. XIV

B.6 Speed, battery, and temperature profiles for GK route using the heuristics algorithm to solve the problem. The suggested solution is to charge for 52.14 minutes at station 10 and for 67.6 minutes at station 23. XV

List of Algorithms

1 Backward recursion of the dynamic programming. Note that for brevity, no constraint validation is shown in the algorithm. At all stages the constraints are checked to be satisfied with probability $1 - \varepsilon$, if not then the cost is set to V_{max}. 38

2 Forward simulation of the dynamic programming. Again the constraint validation is not shown to keep the explanation short. 39

3 Heuristic solution to the mission management problem, which is used to emulate driver behavior. It simulates the truck driving dynamics until the SoC is below 10%, and then backtracks until the last passed charging station. Once a station is found, it charges until full on that station and then continues driving, repeating the same charging decision process until the end of the trip. 45

4 Speed limit pre-processing. Recalculates the speed limits to satisfy the constraints of the truck model. Assumes that the battery temperature is 25 °C and the SoC is 0.5 for all stages. 48

List of Tables

5.1 Station positions and parameters for the route Gothenburg-Rødby. . . 47
5.2 Station positions and parameters for the route Genoa-Karlsruhe. . . . 50

6.1 Summary of mission results for the GR route. Note that the computation time for the hierarchical solvers does not include the backward time of the SDP. The results of the hierarchical solver for the disturbance cases a-c described in section 5.1 are marked with bold. 54
6.2 Summary of mission results for the GK route. Note that the computation time for the hierarchical solvers does not include the backward time of the SDP. The results of the hierarchical solver for the disturbance cases a-c described in section 5.1 are marked with bold. 55
6.3 Comparison of mission results from the station selection layer for different initial SoC values. All uncertainties are represented by the 95% CI of the metrics, and the objective function values are normalized such that the largest mean cost is set to 1. The F_bL_s metric represents total energy losses from friction brake usage. 58
6.4 Comparison of the RMSE of the SoC and battery temperature for the solutions based on the full hierarchical solver and the sigmoid approximation, with absolute errors plotted in figures 6.9a and 6.9b. . 60
6.5 Normalized battery throughput during charging for the GR and GK routes, for the cost function including C-rate (case 1) and the cost function excluding C-rate (case 2). 63

1

Introduction

In November 2016, the Paris Agreement entered into force. It is a legally binding international treaty on climate change which was adopted by 196 nations at the UN Climate Change Conference (COP21) in Paris [1] and has the goal to limit the increase in global average temperature to 1.5°C above the pre-industrial levels. To achieve the goals of this agreement it was found that the emissions of greenhouse gases (GHG) must peak by 2025 at the latest and decline by 43% by 2030. To reach this goal, the EU adopted the European Green Deal in July 2021, which set the target of at least a 55% reduction in total GHG emissions by 2030 [2], and through the "Fit for 55" package it set out a clear path to reach it [3]. This package has now been fully adopted since 2023 and includes legally binding climate goals spanning all sectors. One of them is the REPowerEU plan [4], which is helping the EU save energy, diversify energy supplies, and produce cleaner energy. However, the demand for fossil fuels must also be reduced to complete the transition to carbon neutrality within the energy sector. Thus new reductions on CO_2 emissions have been proposed for heavy-duty trucks [5], and these would restrict emissions 30% further than the already existing emission standard (that imposes a 30% reduction by 2030 [6]). This reduction poses one of the largest challenges yet in the automotive industry. For it to be achievable a wide-scale transition needs to happen from fossil fuel-powered internal combustion engine (ICE) vehicles to zero- and low-emission vehicles (ZLEV), and this is especially important since heavy-duty trucks account for more than 73% of all CO_2 emissions from heavy-duty vehicles.

One type of zero-emission vehicle (ZEV) that exists on the market today is the battery-electric vehicle (BEV) truck, and typically a BEV truck has a range of around 300 km to 400 km [7], [8]. This means that modern-day electric trucks can perform much of the medium-range transport, given that the routes are planned smartly to consider the truck's maximum ranges. One drawback of electric trucks is that the charging takes a long time, and prices can vary depending on the time of place, type of charger, country of origin, and more [9]. Because of this, the task of planning long-haul missions for electric trucks (where one or more charging stops are needed) quickly becomes very complex. For example, in Sweden alone there are more than 2500 charging stations throughout the country [10], with a higher concentration of stations in the south and more sparsely spread out in the north. Since many different combinations of chargers can be used on a mission, it is of interest to find an optimal charging plan and vehicle route to minimize costs, save energy, and maximize the range of the trucks. This problem is called the electric vehicle routing problem (EVRP) and it is well-studied within the literature, see for instance [11] and [12].

In this thesis, a simplified version of the EVRP will be studied, where a fixed route is used between a set of specified waypoints. This problem is hereafter referred to as optimal mission management, and the goal of the mission manager is to select cost-optimal charging stations along the route as well as suggest how much to charge at each station. The thesis is structured as follows: In chapter 1 an overview of the problem is presented and a literature review is performed, after which the research questions of the thesis are presented. In chapter 2 the modeling of the electric truck is presented. In chapter 3 optimal control theory is reviewed. In chapter 4 the optimal mission management problem is formulated mathematically and in chapter 5 a description of the simulation setup is found. In chapter 6 the results of the simulations are presented, and these results are then discussed in chapter 7. Finally, the conclusions of the thesis and future work are presented in chapter 8.

1.1 Literature review

In the following section, an extensive literature review is presented within related areas to the optimal electric vehicle charging problem. The review begins by describing the origin of the EVRP and several variations of it in section 1.1.1. It then proceeds by describing the mission management problem and its relations to predictive energy management (PEM) in section 1.1.2.

1.1.1 Electric vehicle routing problem

As mentioned above, BEVs have been widely researched in recent years as they provide a clean alternative to ICE vehicles and lower running costs. One of the main challenges currently facing the electromotive industry is the energy management of these vehicles since their reduced range necessitates more recharging stops during long trips. Because charging prices vary widely depending on many factors [9], and since different chargers provide different charging capabilities, the problem of deciding an optimal recharging plan quickly becomes complex. It is also common to include optimal routing in the problem formulation, one example being to optimally plan delivery missions and ensure that the BEV does not run out of charge during the trip. This leads to the formulation of the EVRP as an optimal routing strategy that minimizes both travel time and energy costs. A general formulation for this problem is provided by Lin *et al* [11], who in the paper provide an optimal routing solution for a fleet of electric vehicles. The proposed problem can be seen as a variant of the traveling salesman problem, where all possible routes are represented by a graph containing customer nodes that need to be serviced. The proposed EVRP also includes recharging stations, where electric vehicles can stop and charge to make the full trip, and a depot where all routes start and end. This paper also generalized the fleet optimization problem by allowing for heterogeneous fleets, multiple visits to any of the available charging stations, and extended modeling for the battery consumption by considering the effect of load and vehicle speed.

The EVRP is essentially an extension of the green vehicle routing problem (GVRP) as proposed by Erdogan and Miller-Hooks [13] which considers optimal vehicle routing for vehicles with alternative fuel sources and limited range. Both papers allow for multiple visits to each charging station, but in the GVRP formulation, they do not include a cost for energy consumption and assume fixed refueling times. The energy model is however still simplified and models the energy consumption as parametric where each arc in the graph network has a fixed energy consumption related to it, instead of considering the vehicle dynamics. This is expanded on by Shao, Guan, and Bi [12], who model the energy consumption by considering the longitudinal dynamics of the electric vehicle. In the article, the vehicle velocity depends on the currently driven arc and is considered a piece-wise linear function with linear acceleration between each arc. This then allows for the calculation of the energy consumption for each path in the network. They also assume that the charging time is fixed at each station and further assume that the vehicles always start the trip at full charge. No final time constraint is included in the problem formulation, but optimization is performed on both elapsed time and consumed energy.

Further development in the energy estimation has been performed by Basso *et al.* [14] by considering more detailed speed profiles and topography of the paths between each node in the graphs. The paper's authors expand upon the speed estimation by dividing each arc of the graph into multiple road links, with varying speeds and constant acceleration between each link. The estimation also allows for the vehicle to stand completely still at traffic lights, but otherwise considers the speed to be constant for each link. The energy consumption is modeled based on the longitudinal dynamics of an electric truck and also allows for regenerative braking use, which allows for some paths to have a negatively associated energy cost. This deterministic energy model is expanded upon by the author in [15] using a probabilistic modeling framework based on Bayesian regression and the deterministic model described in [14]. By using Bayesian statistics, prior knowledge based on the deterministic model can be updated using measurement data on for instance traffic speed and used to make new predictions on energy consumption. By using a probabilistic model for energy consumption, more reliable charge planning can be performed since the planning considers the variability of the energy levels across the routes and also leads to energy savings for the same reason. Using this probabilistic model, Basso *et al.* presented a reinforcement learning-based dynamical routing in [16], where new customers can be added along a started route. The dynamical routing solution that was presented gives additional flexibility to the system, allowing the vehicle planner to react to real-time traffic scenarios such as accidents, and by using probabilistic models for customer requests it can anticipate additional requests along the route and safely plan charging to not run out. In this paper, the problem is modeled as a Markov decision process (MDP) and it is solved for energy-optimal routing.

There are many methods to solve the vehicle routing problem (VRP) and its derivatives. On the one hand, it could for instance be solved in one stage by directly solving the minimum energy problem by using for instance the Dijkstra algorithm [17] or directly solving the mixed integer programs (MIPs) as in [11]-[13]. On the other hand, other methods include for instance splitting the problem into multiple stages such as in [14]-[16], where the EVRP was solved by first minimizing the energy consumption for all paths in the network and then minimizing the energy for a selected route. A way to formulate the VRP as a hierarchical optimization problem is presented by Marinakis *et al.* [18], who defines two decision phases in the VRP and formulates them as a bilevel program. In the first phase, customers are assigned to vehicles without considering the routing of the vehicles. In the second phase, optimal routing is performed to reach all assigned customers in a cost-optimal way. Splitting the problem into two levels is shown to enable large computational gains and similar results are found by Calvete *et al.* [19] but for the school bus routing problem (SBRB). In the paper, the authors propose both a meta-heuristic solution to the bilevel SBRB and a mixed integer linear program (MILP) reformulation and show that the bilevel solution algorithm both finds better solutions and requires less computational effort.

1.1.2 Mission management

Mission management can in general be described as a set of tools that support the vehicle operation. This support can be strategic in terms of route selection and mission scheduling, but it can also be operational in terms of optimization for the battery state of charge (SoC) or powertrain split. In this thesis the focus will lie on the latter definition, meaning that the goal is to provide optimal vehicle state trajectories as suggestions for the driver to minimize costs. The mission manager will also output an optimal plan for charging along the route, meaning it suggests which stations the driver should stop at and for how long they should charge at each station.

Previous work in PEM, which mission management is part of, has mostly focused on the energy management of hybrid electric vehicles (HEV), both for fuel cell electric vehicles (FCEV) and ICE-HEVs. To minimize the fuel consumption of the HEV, a pre-optimized SoC trajectory is calculated to utilize the electric motor (EM) of the vehicle at its highest efficiency thus also minimizing the use of the ICE. In her master thesis, Katsargyri [20] utilized dynamic programming (DP) [21] to optimize the SoC trajectory of a HEV for a given reference route split into segments with road grade information. The optimized SoC trajectory was then sent to a lower-level controller that optimizes the powertrain split given the SoC, speed, and engine states. Using path forecasting to optimize the SoC leads to better fuel economy, and Katsargyri *et al.* [22] also investigated a receding horizon control (RHC) solution to the problem as well. The RHC solution performed better in terms of computation power, with a slight reduction in energy savings compared to the DP solution. Johannesson *et al.* [23] present a model predictive control (MPC) scheme that maximizes energy efficiency in real-time operation for long-haul HEV trucks, assuming only longitudinal dynamics apply. The problem is formulated as a mixed integer nonlinear program (MINLP), with gear selection as the integer variable. To enable fast solving, the problem is reformulated into three layers with the gear shifting and mode decision between full electric and hybrid being handled using DP. The constructed hierarchical controller shows fuel-saving benefits while still being efficient enough to be used in an online application and it considers topographic road data such as grade and speed limits. The top-level controller is based on solving a convex nonlinear program (NLP), where assumptions are made on constraints and dissipative forces to reach a convex problem. This paper was then expanded upon by Johannesson *et al.* [24] with predictive information about surrounding traffic by introducing bounds to the travel time of each prediction horizon.

To avoid the curse of dimensionality that DP suffers from, but still keep the exactness of the solution, Uebel *et al.* [25] proposed a combination of using the Pontryagin minimum principle (PMP) [26] to feed the co-states of time and energy to a DP optimizer that calculates speed, gear selection, and engine on/off. The hierarchical control then reaches the global optimum while still allowing for online applications. Lim and Su [27] propose another hierarchical control structure for HEVs where the top level optimizes SoC and velocity for a full trip and a lower-level controller re-optimizes the engine split and motor on/off with a shorter horizon while driving, using the higher-level solution as references. Their control scheme allows for adaptions of the power split for unexpected traffic changes to keep the optimal energy management while driving and uses a probabilistic approach to perform both levels of the optimization. A quadratic programming (QP) method for the optimal energy management of FCEVs was proposed by Zendegan *et al.* [28] which utilized route information to make predictions on the future energy consumption. The method maximizes the fuel cell efficiency considering constraints on the powertrain, battery, and fuel cell system given assumptions on vehicle speed and route topography. The optimized SoC trajectory for the whole trip is then fed to a lower-level online energy management system that optimizes the power split of the vehicle.

Stochastic methods have also been proposed for the control of HEVs. Vagg *et al.* [29] used stochastic dynamic programming (SDP) to robustly manage the energy during a driving cycle while also considering the battery health degradation by including the square of the battery throughput in the cost function, modeling the evolution of the speed, acceleration, and gear as a Markov process. Yang *et al.* [30] proposed a stochastic model predictive control (SMPC) based PEM strategy with rolling optimization for optimizing fuel efficiency while considering stochastic driving behaviors. In his PhD thesis, Le Rhun [31] proposes a stochastic optimal control policy for the energy management of HEVs under the influence of traffic conditions. The proposed energy management system is formulated as a bilevel optimization problem, where the top level consists of an offline infinite horizon SDP which optimizes power-split for stochastic traffic situations and an online discrete dynamic programming (DDP) optimizer to generate the optimal SoC profile for a given traffic situation. Road topography is not considered to simplify the energy model and approximates the traffic conditions with a Markov chain structure. In their article, Lin, Peng, and Grizzle [32] present an SDP-based energy management strategy for HEVs. It is shown that the infinite horizon SDP outperforms a deterministic rule-based approach based on DDP results when it comes to minimizing fuel consumption, where it can adapt to many different driving cycles.

In a paper by Souley *et al.* [33], a DP-based method was proposed to optimize the charging of a BEV, given that the vehicle charges at all charging stations and no stops are made except for at stations. The authors utilize a simplified model where only the state of energy (SoE) is considered as a state, and velocities are constant over road segments. Another simplification is that the vehicle is assumed to stop at every recharging station, but the amount of charged energy is optimized at each station. Similarly, Hamednia *et al.* [34] optimize the charging for a trip where the BEV stops at each station, but also includes the thermal management and optimizing the speed profile for eco-driving by formulating a hybrid dynamical system. This result was then extended by Hamednia *et al.* [35] by introducing integer charging decisions to enable the vehicle to not stop at each station, formulating a MINLP. A simplification in this article is that the speed was not optimized, where the vehicle follows a fixed speed trajectory.

This thesis is a continuation of the thesis written by Bragde and Sundberg [36], where an optimal mission planner was developed for heavy-duty FCEV trucks. In their thesis, the optimal mission management problem is formulated as an NLP that is solved by using nonlinear model predictive control (NMPC), generating optimal SoC, battery power, fuel cell power, and vehicle speed trajectories as well as refueling decisions for given routes, minimizing the total cost of operation (TCOP). To solve the problem, they smoothen the refueling decision by using a sigmoid activation function to avoid introducing an integer decision variable and formulate it as a full horizon NMPC problem. Besides this, they also assume a constant battery temperature and simplify the gear selection. The results of the mission manager are compared to receding horizon PEM controllers and show that the pre-optimized SoC trajectory can provide large energy savings (up to 17% reduced consumption). To improve the accuracy of the solution in this thesis, aside from working with BEV trucks instead, changes to the solution strategy have been made. The sigmoid activation function has been removed to treat the charging decisions as binary choices, reformulating the problem into a MINLP. This problem has then been decomposed into two subproblems structured into separated layers. The top layer solves the MINLP problem for a simplified mathematical model of the system, optimizing for fewer states using SDP to select optimal charging stations and optimize the starting time of the mission. This information is then sent to the lower layer which can now be solved as an NLP to optimize the full state problem given the charging decisions from the upper layer.

1.2 Purpose

The objective of this thesis is to improve upon the previously developed mission manager by Bragde and Sundberg [36] by introducing a hierarchical control structure to remove assumptions that were previously made to simplify the MINLP, and to make the station selection more robust by introducing stochastic disturbances in the optimization. This controller acts as a high-level advisory system that will suggest optimal charging stations to drivers of battery electric trucks to encourage energy-efficient charging and reduce the total costs of the missions.

1.3 Limitations

Only longitudinal dynamics will be considered in the problem formulation, which means that the road the truck is traveling is considered straight and forces only act along the axis the truck is driving on or perpendicular to it. Only one truck is considered in the optimization and no routing will be performed, meaning that the route is a pre-determined problem parameter. Further, the cruising speed of the truck will not be part of the optimization and will also be treated as a problem parameter.

Per EU regulation, truck drivers may not drive for more than 4 hours without a 45-minute break in between, and not more than 9 hours for a full day [37]. These and more regulations for driving times result in the scheduling of truck driving becoming a complex problem on its own, as is studied in [38]. To reduce the complexity of the mission management problem these legal limits will not be considered.

1.4 Research questions

The following research questions have been formulated to be answered in the thesis

- How can a hierarchical control structure be defined to solve the mixed integer formulation of the problem efficiently?
- How can the station selection be made robustly to account for uncertainties in power demand?
- How can time-varying parameters like traffic speed and charging prices at charging stations be incorporated into the problem formulation?
- How can battery health decay be minimized at a mission management level?

2

Modeling

In this thesis a long-haul battery electric truck is considered, using a lithium-ion battery as the energy source. The battery can be charged by either regenerative braking or at recharging stations. This chapter presents the modeling of the truck, considering the vehicle dynamics in section 2.1 and the powertrain in section 2.2.

2.1 Vehicle dynamics

Per the assumptions made in section 1.3, only longitudinal dynamics are considered. According to Newton's second law of motion, with the assumption of zero slip, these are described by

$$m_e\dot{v} = F_T - F_{rr} - F_{grad} - F_{brake} - F_{air}, \tag{2.1}$$

where m_e is the equivalent mass of the vehicle including vehicle mass and the inertia of rotating components in the gearbox, v is the longitudinal velocity of the vehicle, F_T is the traction force at the wheels generated by the EM, F_{rr} represents rolling resistance forces from all wheels, F_{grad} is the gravitational force from the road gradient, F_{brake} is the total retarding force from friction brake usage and F_{air} is total aerodynamic drag force. These force components are demonstrated in figure 2.1.

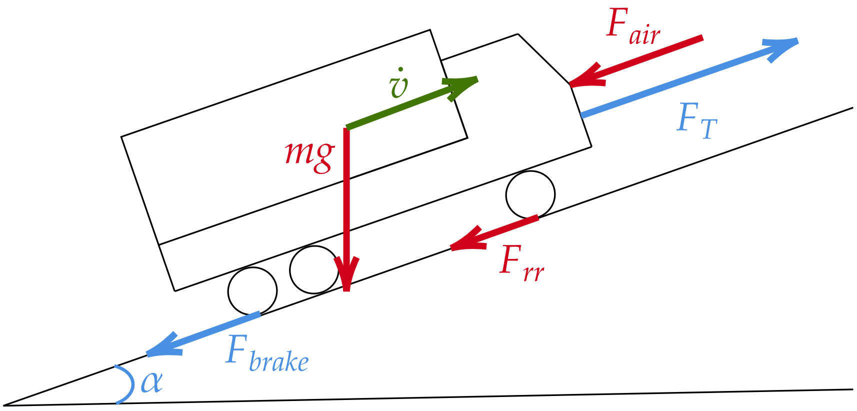

Figure 2.1: Different forces acting on a truck, red arrows represent external forces, blue arrows represent vehicular forces. The acceleration vector is represented by the green arrow.

Hereafter follows expressions for the different force components, except for the traction effort F_T which is described in section 2.2 where the powertrain is modeled. To enable regenerative braking using the electric motor, F_T is allowed to take both positive and negative values. The air resistance is assumed to be proportional to the squared difference between the vehicle velocity v and the wind speed, v_{wind}. To account for the relative direction between the vehicle heading θ and the wind direction θ_{wind}, the relative wind speed squared becomes

$$\begin{aligned} v_{rel}^2 &= \|\vec{v} - \vec{v}_{wind}\|^2 = (v\cos(\theta) - v_{wind}\cos(\theta_{wind}))^2 + (v\sin(\theta) - v_{wind}\sin(\theta_{wind}))^2 \\ &= v^2 + v_{wind}^2 - 2vv_{wind}\cos(\theta - \theta_{wind}). \end{aligned} \tag{2.2}$$

The relative wind direction β is given by

$$\beta = \arctan\left(\frac{v_{rel,y}}{v_{rel,x}}\right) = \arctan\left(\frac{v\cos(\theta) - v_{wind}\cos(\theta_{wind})}{v\sin(\theta) - v_{wind}\sin(\theta_{wind})}\right). \tag{2.3}$$

With this and the relative speed the air drag becomes

$$F_{air} = \frac{1}{2}\rho_a \mathrm{CdA}(\beta(t))v_{rel}^2, \tag{2.4}$$

where $\mathrm{CdA}(\beta)$ is a look-up table modeling the frontal area and air drag coefficient as a function of the relative wind direction β, ρ_a is the air density which depends on weather conditions and altitude.

The gradient and rolling resistance forces are both dependent on the road gradient α, and proportional to the gravitational force $F_g = mg$, where m is the vehicle mass and g is the gravitational acceleration $g \approx 9.81\,\mathrm{m/s^2}$. Their expressions are given by

$$F_{rr} = C_{rr}mg\cos(\alpha), \tag{2.5}$$

$$F_{grad} = mg\sin(\alpha), \tag{2.6}$$

where C_{rr} is the rolling resistance coefficient of each tire, which depends on the truck tires and road surface conditions [39], [40],[41]. For heavy-duty trucks and dry weather conditions it can be approximated to 0.0035 [40].

The braking force F_{brake} results from the disc brake usage and is treated as a user input in the model. Ideally, the friction braking usage should be kept low due to it resulting in loss of energy, compared to regenerative braking (from $F_T < 0$) which allows some of the energy to be restored, but this effect is examined closer in the following section.

2.2 Powertrain structure

A simplified schematic diagram of the studied powertrain is shown in figure 2.2. The powertrain includes propulsion components, such as the EM and the battery, a thermal management system that controls the battery temperature, and auxiliary systems such as the cabin heating system. The powertrain is structured into three domains, the electrical domain which is elaborated upon in section 2.2.1, the mechanical domain which is examined in section 2.2.2 and the thermal domain which is studied in section 2.2.3.

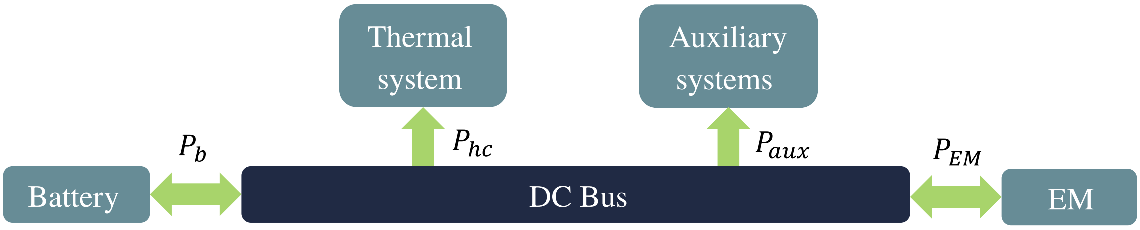

Figure 2.2: Simplified schematic diagram of the studied electric powertrain, describing the electric power flow between the different electrical components in the truck.

2.2.1 Battery modeling

The battery which is considered consists of lithium titanium oxide (LTO) cells that have high charge/discharge power limits and high cycle lifetimes, but lower terminal voltages than other lithium battery types [42]. The battery components consist of multiple LTO cells in series and parallel, and each cell is approximated using a second-order resistance-capacitance (RC) model which is shown in figure 2.3, which consists of a voltage source u_{oc}, an internal resistance R_0 and two RC pairs R_1, C_1 and R_2, C_2. This battery model is based on the work in [43] and [44], where much more in-depth thermal management methods are described. However, by assuming steady-state conditions within the battery, the introduction of additional voltage states can be avoided. The open circuit voltage u_{oc} is determined by the number of cells in parallel n_p and is dependent on the battery temperature T_b and the SoC, while the maximum capacity of the battery C_b is determined by the number of cells in series n_s.

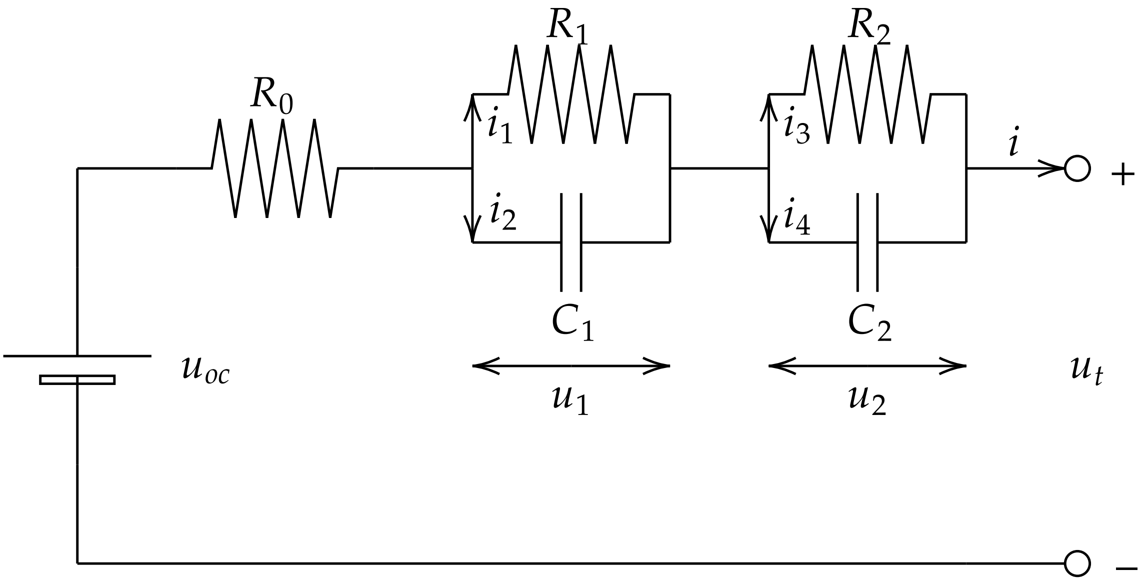

Figure 2.3: Equivalent circuit used to model the battery cells.

The SoC is defined as the relation between the current battery charge Q and the battery capacity C_b, with variable dependencies omitted for convenience

$$\mathrm{soc} = \frac{Q}{C_b}. \tag{2.7}$$

The instantaneous charge Q is often difficult to measure exactly, but the charge rate of change can be estimated by the output current from the battery i_b, which gives the derivative of the SoC as

$$\mathrm{s\dot{o}c} = \frac{\dot{Q}}{C_b} = -\frac{\eta_c i_b}{C_b}, \tag{2.8}$$

where i_b is the battery current, and η_c is the Coulombic efficiency of the battery, which depends on whether the battery is charging or discharging. Denote $P_b = i_b u_b$ as the total battery power flow, where u_b is the terminal voltage. By convention, a positive P_b discharges the battery. To find the total losses in the battery, the losses of each battery cell are summed together. Using Kirchoff's current law, the equations for an ideal capacitance and Ohm's law yields

$$i_1 = \frac{u_1}{R_1}, \tag{2.9}$$

$$i_2 = i - i_1 = C_2 \frac{\mathrm{d}u_1}{\mathrm{d}t}, \tag{2.10}$$

$$i_3 = \frac{u_2}{R_2}, \tag{2.11}$$

$$i_4 = i - i_3 = C_2 \frac{\mathrm{d}u_2}{\mathrm{d}t}, \tag{2.12}$$

which gives that

$$\begin{cases} \frac{\mathrm{d}u_1}{\mathrm{d}t} = -\frac{1}{R_1C_1}u_1 + \frac{1}{C_1}i & \Rightarrow u_1(t) = iR_1\left(1 - e^{-\frac{t}{R_1C_1}}\right)i + u_1(0), \\ \frac{\mathrm{d}u_2}{\mathrm{d}t} = -\frac{1}{R_2C_2}u_2 + \frac{1}{C_2} & \Rightarrow u_2(t) = iR_2\left(1 - e^{-\frac{t}{R_2C_2}}\right)i + u_2(0). \end{cases} \tag{2.13}$$

The resistances R_0, R_1, and R_2 vary with SoC and temperature but the dependency is omitted here to simplify the expression. The open circuit voltage u_{oc} also depends on SoC and temperature and is shown in figure 2.4. R_1 and R_2 also change depending on whether the cell is charging or discharging, this dependency is also omitted since it does not change the derivation of the expression, but the superscripts *ch* and *dch* are introduced to distinguish between the modes where the distinction is necessary. To find the cell current, the equivalent resistance of the circuit is calculated according to

$$R_{eq} = R_0 + R_1\left(1 - e^{-\frac{t}{R_1C_1}}\right) + R_2\left(1 - e^{-\frac{t}{R_2C_2}}\right) \approx R_0 + R_1 + R_2, \tag{2.14}$$

where the battery current is assumed to reach a steady state at all charging/discharging instances to simplify the dynamics, this resistance is plotted in figure 2.5. Using this the power balance equation for the battery cell becomes

$$P_{b,cell} = u_{oc} i - R_{eq} i^2, \tag{2.15}$$

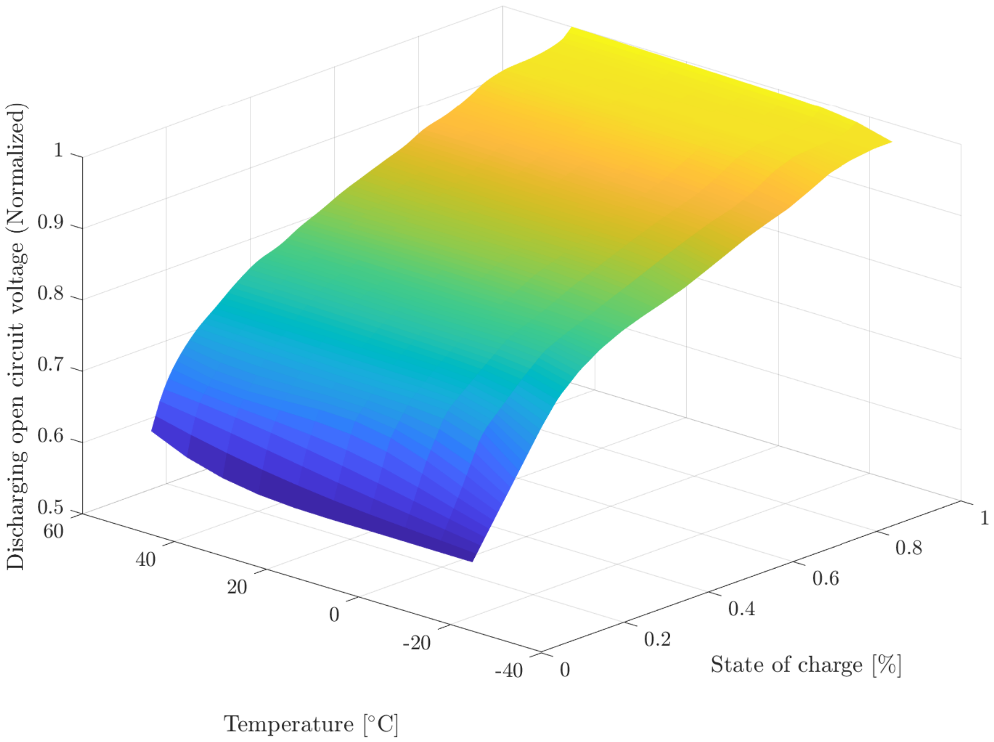

(a) Battery open circuit voltage while discharging.

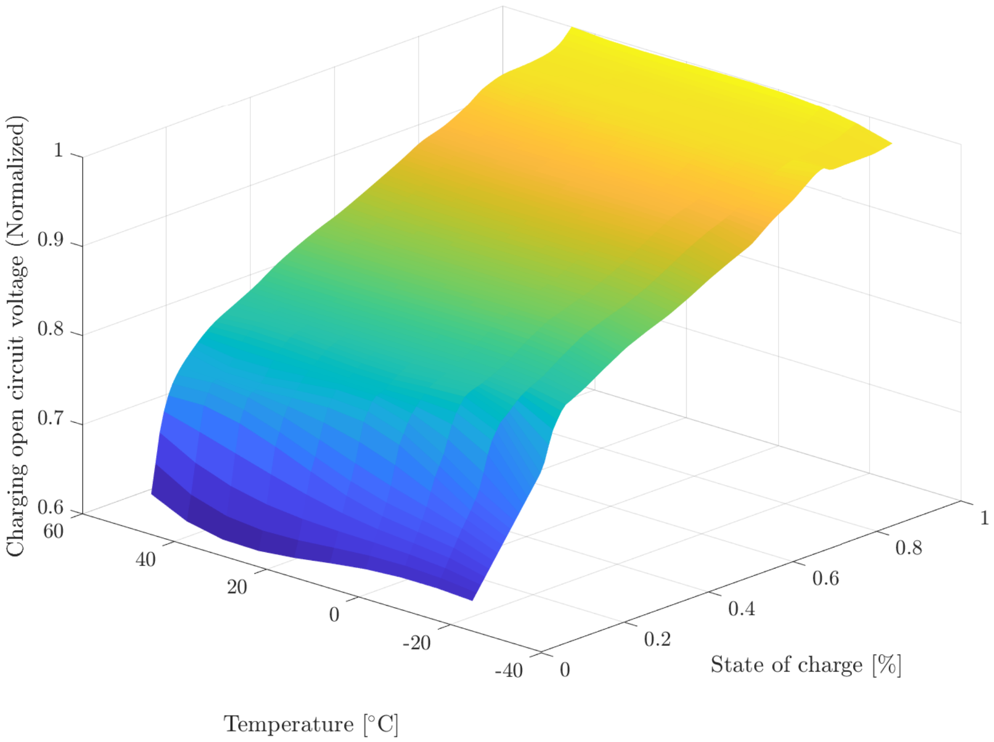

(b) Battery open circuit voltage while charging.

Figure 2.4: **(a)**: Battery discharging open circuit voltage, dependent on the battery SoC soc and temperature T_b. **(b)**: Battery charging open circuit voltage, dependent on the battery SoC soc and temperature T_b.

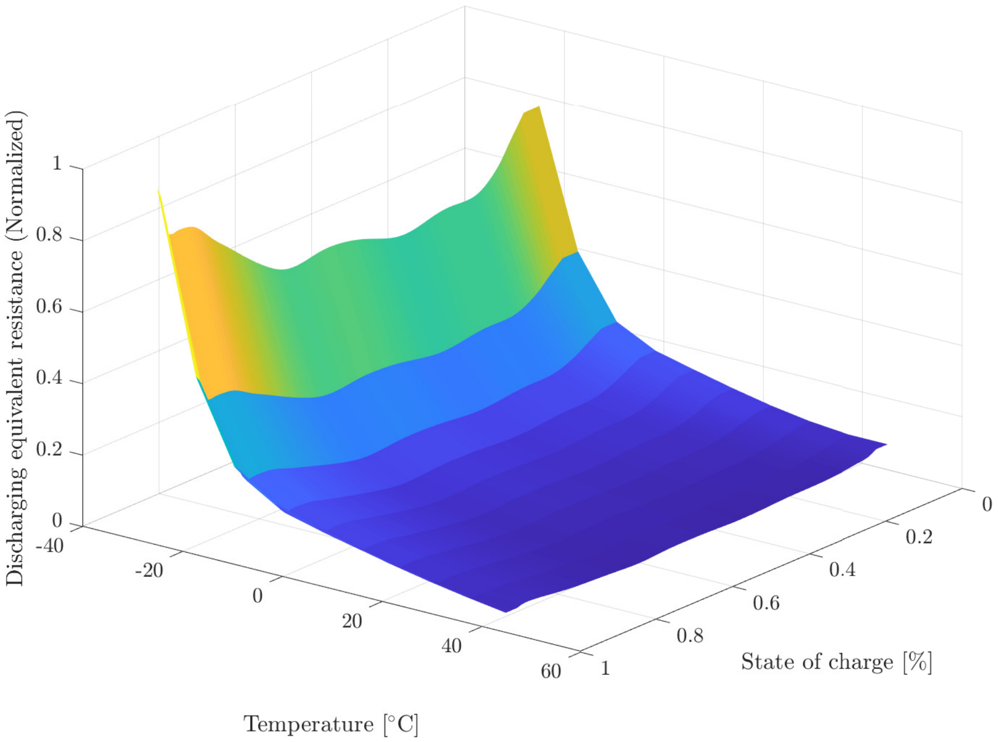

(a) Battery equivalent resistance while discharging.

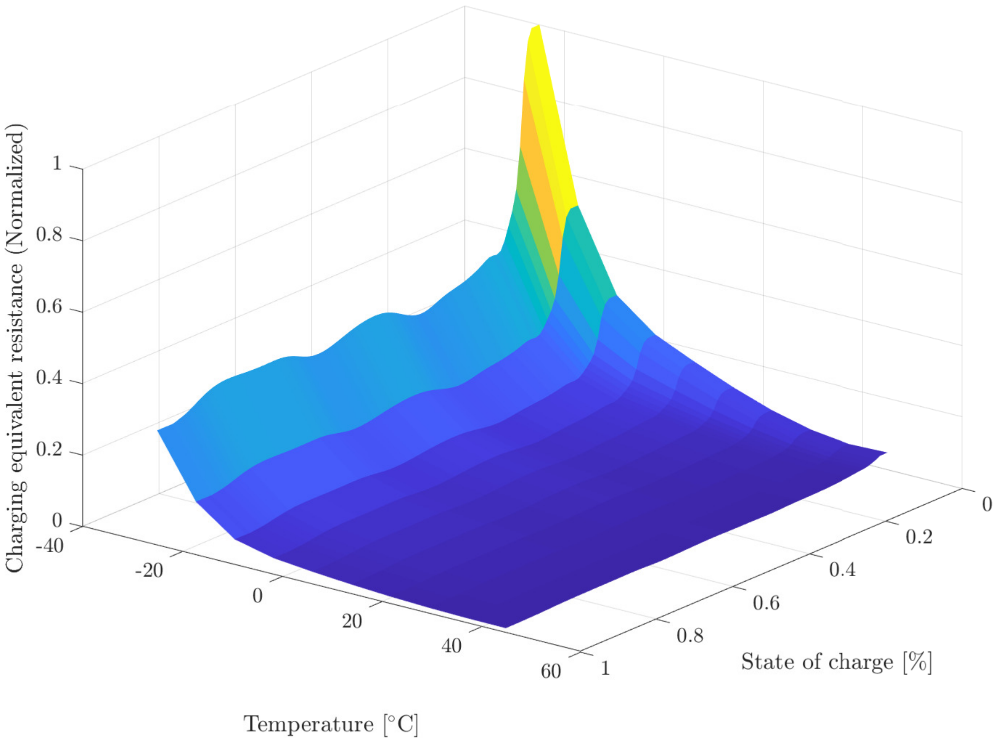

(b) Battery equivalent resistance while charging.

Figure 2.5: **(a)**: Battery discharging internal resistance, dependent on the battery SoC and temperature T_b. **(b)**: Battery charging internal resistance, dependent on the battery SoC and temperature T_b.

where $P_{b,cell} = P_b/(n_s n_p)$ is the requested power to the cell. Solving this equation for i results in the expression

$$i = \frac{u_{oc} - \sqrt{u_{oc}^2 - 4R_{eq}P_{b,cell}}}{2R_{eq}} \approx \frac{P_{b,cell}}{u_{oc}} + \frac{R_{eq}P_{b,cell}^2}{u_{oc}^3} = \frac{P_{b,cell} + P_{b,loss,cell}}{u_{oc}}, \tag{2.16}$$

where the approximation is made by assuming that the losses $P_{b,loss,cell}$ are small in comparison to the total cell power $P_{b,cell}$ and thus the second order Taylor expansion of the square root can be applied. The total current in the battery is found by multiplying the cell current i with n_p, which gives the SoC update equation

$$\dot{\text{soc}} = -\frac{\eta_c P_{b,tot}}{n_s C_b u_{oc}(\text{soc}, T_b)} \approx -\eta_c \frac{P_b + P_{b,loss}}{E_{cap}}, \tag{2.17}$$

where E_{cap} is the total energy capacity of the battery and $P_{b,loss}$ is the total power losses

$$P_{b,loss} = \frac{R_{eq}(\text{soc}, T_b)P_b^2}{n_s^2 u_{oc}^2(\text{soc}, T_b)}, \tag{2.18}$$

The battery power output P_b is split into propulsive power P_{EM}, auxiliary power to thermal management systems of the truck P_{hc}, other auxiliary power P_{aux} and charging power P_{stat} as is shown in figure 2.2, this results in the power balance equation

$$P_b = P_{EM} + P_{hc} + P_{aux} - P_{stat}, \tag{2.19}$$

where P_{EM} can be either positive or negative depending on the direction of EM operation. This finally gives the full expression for the SoC dynamics and the power balance

$$\dot{\text{soc}} = -\eta_c \frac{P_b + \frac{R_{eq}(\text{soc},T_b)P_b^2}{n_s^2 u_{oc}^2(\text{soc},T_b)}}{E_{cap}}, \tag{2.20a}$$

$$P_b + P_{stat} = P_{EM} + P_{hc} + P_{aux}. \tag{2.20b}$$

Battery capacity degrades quickly during high power charging and discharging and is more sensitive during low battery temperatures and SoC, as is seen in [45], [46], and [47]. For this reason, SoC and temperature-dependent charging and discharging limits are introduced to the total battery power to minimize degradation, which is handled by a battery management unit (BMU). For the truck that is studied in this thesis, the (normalized) power limits are shown in figure 2.6. For the battery that is studied, the ideal SoC range for high-power discharging is about $20\% - 100\%$ and the ideal range for charging is about $0\% - 60\%$. For both charging and discharging the ideal temperature range for high power availability is around $20\,°\text{C} - 40\,°\text{C}$. To measure the rate of charging or discharging, the charge rate (C-rate) is typically used

$$C_r = \frac{i_b}{C_b} \approx \frac{P_b + P_{b,loss}}{E_{cap}} = \dot{\text{soc}}. \tag{2.21}$$

The unit of the C-rate is C, which relates to the time to fully charge or discharge the battery according to $t = 1/C_r$, where t is the charging or discharging time in hours. Typically, for lithium-ion batteries, the battery temperature should be kept above 20 °C to avoid degradation while charging at high C-rates, as is shown in [47]. For this reason, the battery temperature is constrained. Another property that is related to battery degradation is the battery throughput, which is defined as the sum of charged and consumed battery energy

$$H = E_{chg} + E_{con}. \tag{2.22}$$

This means that H measures the total usage of the battery.

2.2.2 Mechanical modeling

Based on the forces acting upon the vehicle, as described in section 2.1, the traction force at the wheels is given by

$$F_T = m_e\dot{v} + mg(\sin(\alpha) + C_{rr}\cos(\alpha)) + \frac{1}{2}\rho_a \mathrm{CdA}(\beta)v_{rel}^2 + F_{brake}, \tag{2.23}$$

This can also be expressed as a force generated by the EM

$$F_T = \frac{\eta_{EM}(\omega_{EM}(\gamma), \tau_{EM})^{d_{EM}} r_{EM}(\gamma) r_{tm} \tau_{EM}}{r_{eff}}, \tag{2.24}$$

where η_{EM} is the efficiency of the EM and it's dependent on the torque τ_{EM} and rotation speed of the motor ω_{EM}, r_{EM} is the gear ratio of gear γ, r_{tm} is the fixed gear ratio of the transmission and r_{eff} is the effective tire radius. The term $d_{EM} \in \{-1, 1\}$ specifies the direction in which the motor is running. If it is propelling the vehicle then $d_{EM} = 1$, if it is operating as a generator then $d_{EM} = -1$. In figure 2.7 an efficiency map of all feasible pairs of motor torques and rotation speeds is shown. The gearbox has 12 gears and transmission losses between these are assumed to be constant, the relation between the wheel rotation speed ω_w and EM rotation speed ω_{EM} is

$$\omega_w = \frac{\omega_{EM}}{r_{tm} r_{EM}(\gamma)}. \tag{2.25}$$

Since zero slip is assumed, the rotation speed of the wheels is directly correlated to the speed of the vehicle which gives that

$$\omega_{EM} = \frac{r_{tm} v}{r_{EM}(\gamma) r_{eff}}. \tag{2.26}$$

The EM power is related to the torque and rotation speed as

$$P_{EM} = \omega_{EM}\tau_{EM}, \tag{2.27}$$

and this together with equations (2.24) and (2.26) gives the expression for traction effort as

$$F_T = \eta_{EM}(\omega_{EM}(\gamma), \tau_{EM})^{d_{EM}} \frac{P_{EM}}{v}, \tag{2.28}$$

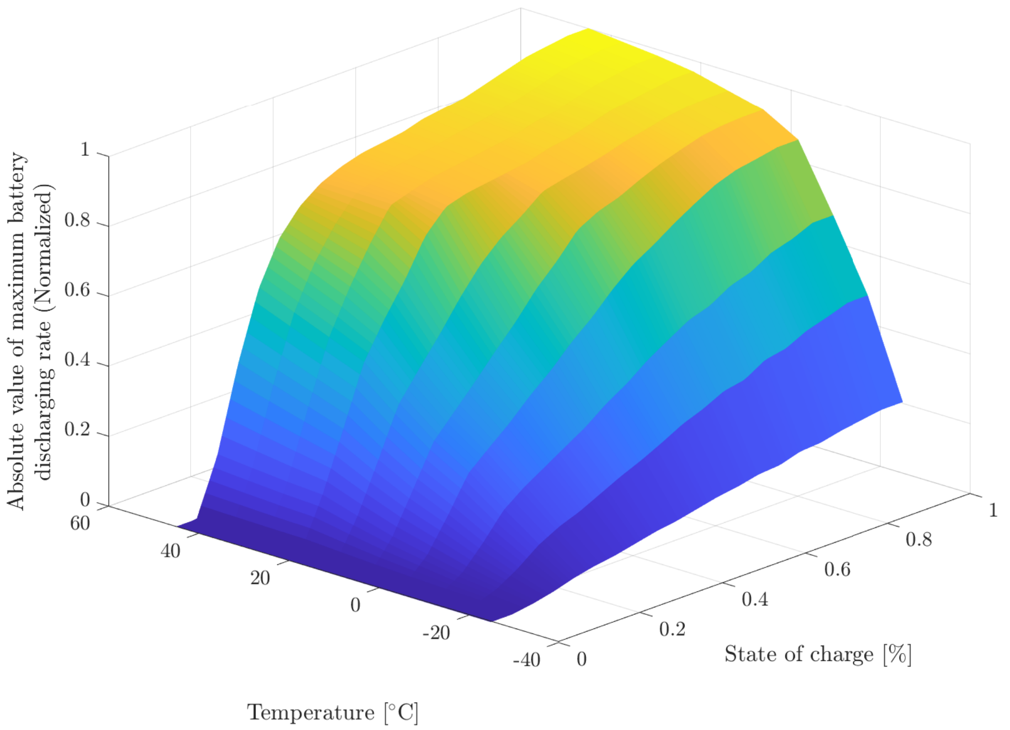

(a) The SoC and temperature dependent maximum discharge power limit.

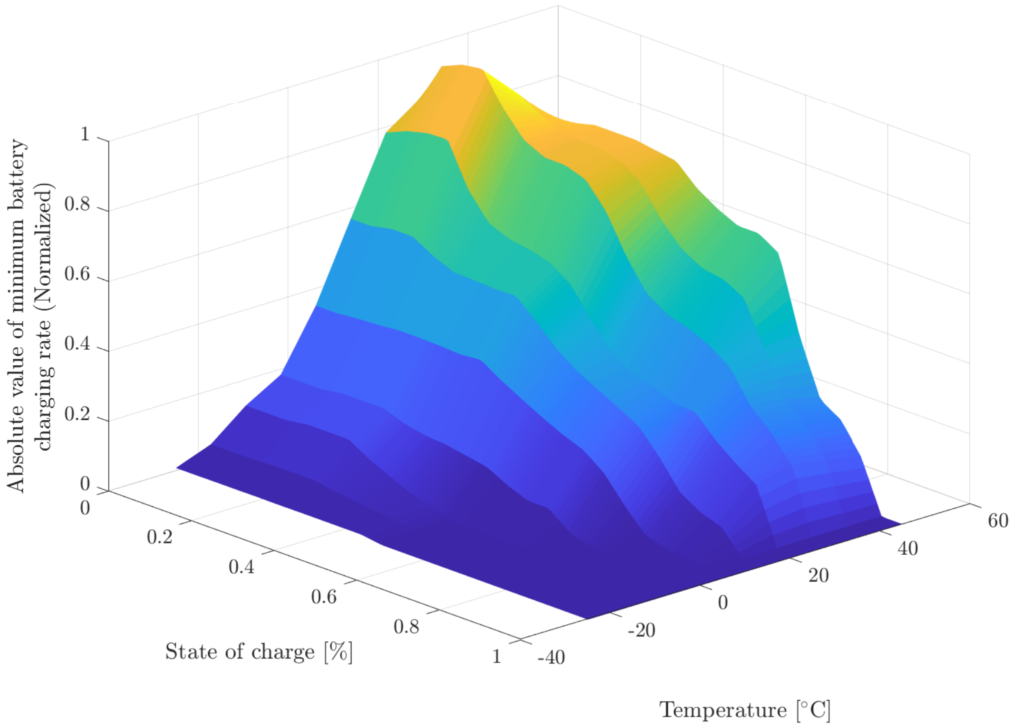

(b) The absolute value of the SoC and temperature-dependent minimum charge charge power limit.

Figure 2.6: **(a)**: Battery maximum discharging power, dependent on the battery SoC soc and temperature T_b. **(b)**: Absolute value of minimum battery charging power, dependent on the battery SoC soc and temperature T_b.

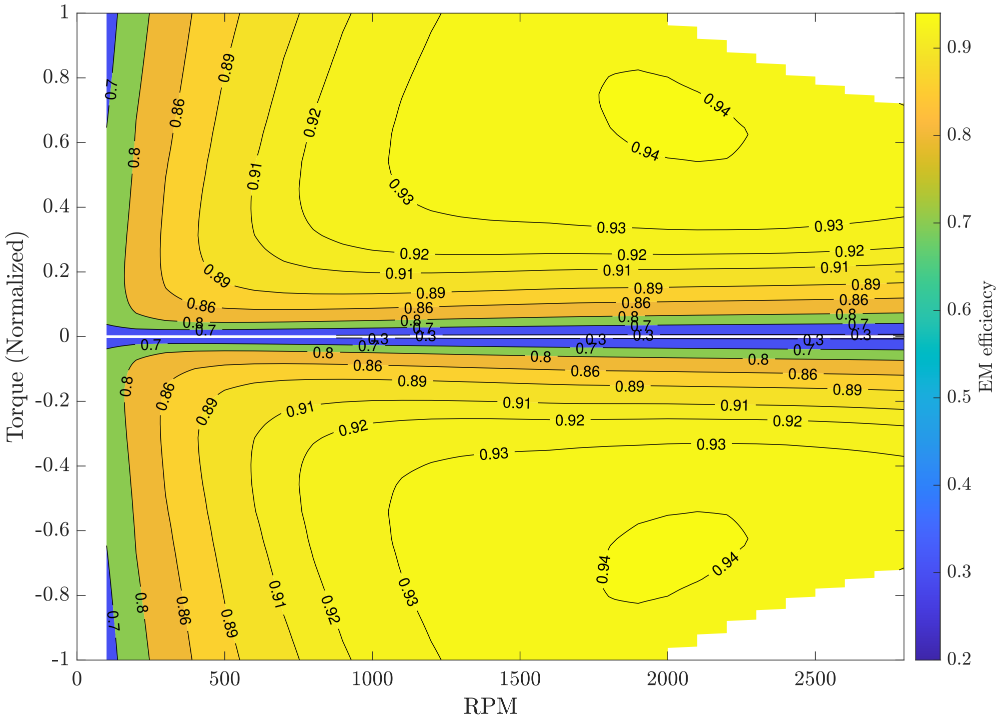

Figure 2.7: EM efficiency map for feasible pairs of motor torque and RPM.

Together with equation (2.23) this gives an expression for the EM power

$$\begin{aligned} P_{EM} = {} & \eta_{EM}(\omega_{EM}(\gamma), \tau_{EM})^{-d_{EM}}(m_e\dot{v} + mg(\sin(\alpha) + C_{rr}\cos(\alpha)) \\ & + \frac{1}{2}\rho_a \mathrm{CdA}(\beta) v_{rel}^2) + F_{brake})v, \end{aligned} \tag{2.29}$$

To avoid additional complexity arising from the selection of γ, which includes solving another MIP as in [48], it is assumed that a low-level controller always selects the efficiency-optimal gears. From this, an efficiency map can be built for feasible vehicle speed and traction pairs, giving the speed and traction effort-dependent expression for the propulsive power

$$P_{EM} = \eta_{EM}(v, F_T)^{-d_{EM}} \underbrace{(m_e\dot{v} + mg(\sin(\alpha) + C_{rr}\cos(\alpha)) + \frac{1}{2}\rho_a \mathrm{CdA}(\beta) v_{rel}^2 + F_{brake})}_{F_T} v, \tag{2.30}$$

To avoid numerical issues arising from the division $1/\eta_{EM}$ when the EM is propelling the vehicle, a conversion to working with motor losses directly is made. This means that we instead use the expression

$$P_{EM}(v, F_T) = (F_T + F_{T,loss}(v, F_T))v, \tag{2.31}$$

where $F_{T,loss}(v, F_T)$ is a positive dispersing force. To calculate the motor losses from the efficiency map, the following formula is used to ensure that the losses are always positive

$$F_{T,loss}(v, F_T) = \begin{cases} F_T(\eta_{EM}^{-1}(v, F_T) - 1), & F_T > 0, \\ -F_T(1 - \eta_{EM}(v, F_T)), & F_T < 0. \end{cases} \tag{2.32}$$

As is seen in figure 2.7, the maximum force that can be applied by the motor depends not only on the torque but also on the speed of the motor, which is related to the traveling speed of the vehicle v. Using the previous assumption on the gear selection gives speed and traction effort-dependent efficiency map in shown in figure 2.8, where the optimal gear selection is also demonstrated. This figure also shows the speed-dependent bounds on the traction effort $F_T^{max}(v)$ and $F_T^{min}(v)$.

2.2.3 Thermal modeling

The thermal dynamics are described through the formulation of a thermal energy balance equation, where a lumped-mass model is used for the battery temperature. This means that uneven battery temperatures caused by diffusion are not considered and the core temperature is set equal to the surface temperature. This gives rise to the following differential equation describing the rate of temperature change

$$\dot{T}_b = \frac{1}{c_{p,b} m_b} \left(Q_{gen}(\cdot) + Q_{act}(T_b, T_b^{ref}) \right), \tag{2.33}$$

where $c_{p,b}$ is the specific heat of the battery, m_b is the mass of the battery, Q_{gen} is the generated heat rate from the battery, and the electric powertrain losses $vF_{T,loss}$, Q_{act} is active heat rate resulting from the thermal management system, which uses the reference temperature T_b^{ref} as input and depends on the current battery temperature T_b. All losses in the powertrain are assumed to be converted to heat energy which needs to be cooled by the thermal system, meaning that the generated heat rate is expressed as

$$Q_{gen}(\cdot) = \frac{R_{eq}(\text{soc}, T_b) P_b^2}{n_s^2 u_{oc}^2(\text{soc}, T_b)} + vF_{T,loss}(F_T, v) + (1 - \eta_c)|P_b|. \tag{2.34}$$

The active heat rate $Q_{act}(T_b, T_b^{ref})$ and the power consumption of the thermal system $P_{hc}(T_b, T_b^{ref})$ are abstracted from a more advanced thermal model including the effects of speed-dependent heat exchange with the surrounding air, the power demand of the truck and the battery temperature. It also includes the thermal management of the EM, but to reduce the model complexity it is assumed that lower-level controllers handle the thermal management of the EM such that it always works at its highest efficiency. The power demand of this is thus included in the power balance equation of the battery, but the temperature of the EM is not controlled to reduce the model complexity.

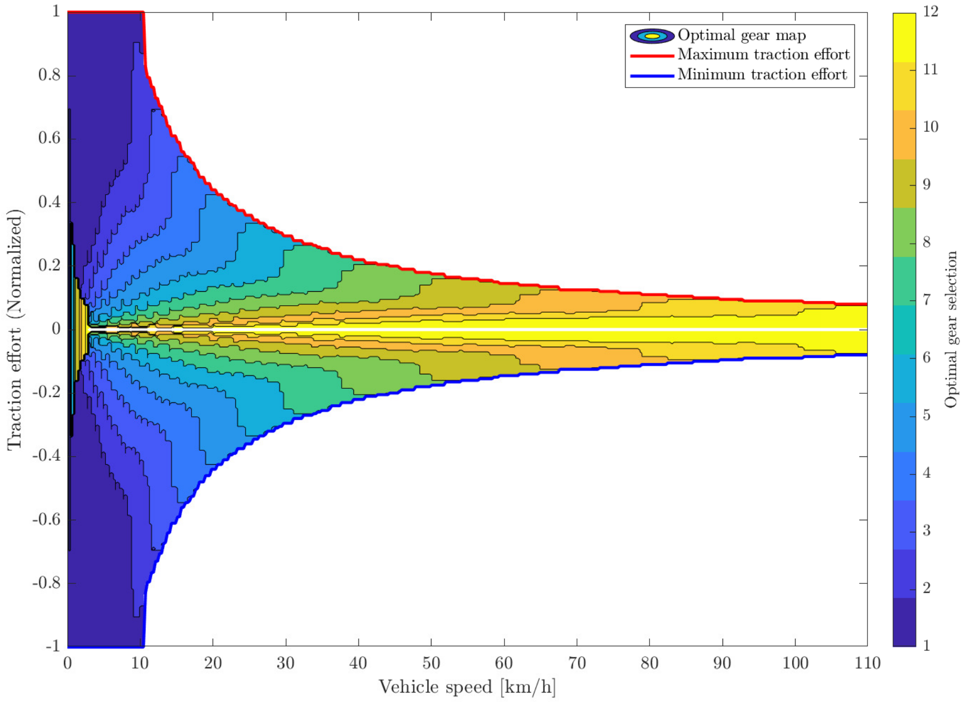

(a) Optimal gear map.

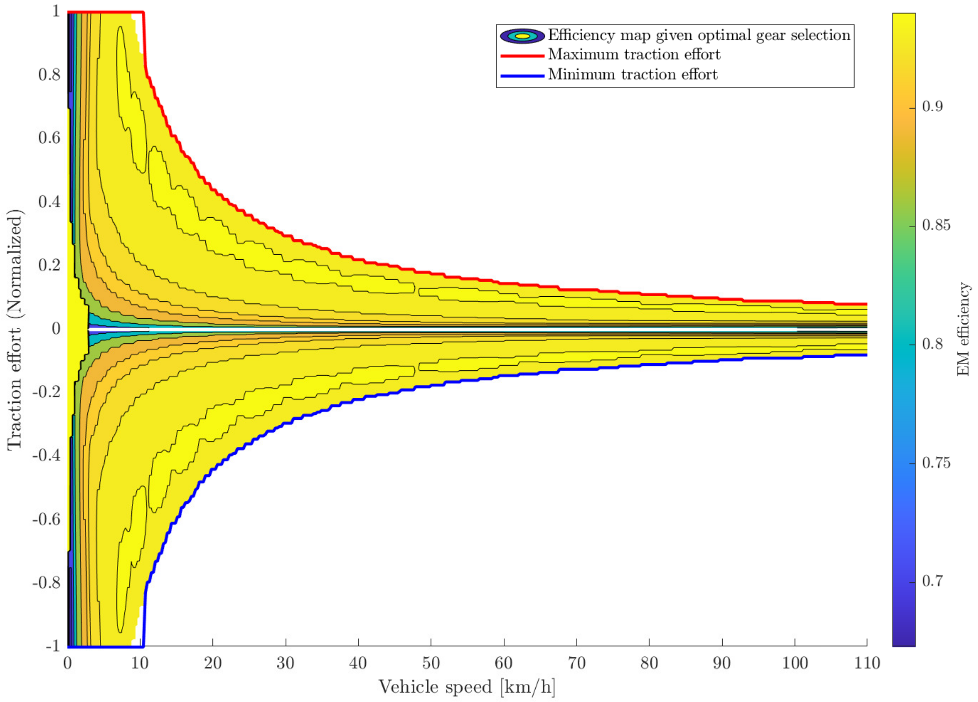

(b) Motor efficiency at optimal gear.

Figure 2.8: **(a)**: Speed and traction effort dependent optimal gear map as well as lower (blue) and upper (red) bounds on traction effort, $F_T^{min}(v)$ and $F_T^{max}(v)$. **(b)**: EM efficiency at optimal gear selection as well as lower (blue) and upper (red) bounds on traction effort, $F_T^{min}(v)$ and $F_T^{max}(v)$.

3

Optimal control theory

In the following chapter, some foundations of optimal control theory will be presented. The concepts will not be explained in full detail, nor will all concepts be covered, to reduce the length of the discussion. At first, an overview of deterministic optimal control will be explained, then stochastic optimal control will be covered. For a more detailed introduction to optimal control theory, see for instance [49] and [50]. Also, note that the inclusion of binary variables is omitted in the explanation.

3.1 Deterministic optimal control

The description of optimal control theory first begins with describing the systems which are to be controlled. In the case which is studied in this thesis, for continuous-time dynamics, these systems are defined by constrained ordinary differential equations (ODE)

$$\begin{aligned} \dot{\mathbf{x}}(t) &= \mathbf{f}(\mathbf{x}(t), \mathbf{u}(t), \mathbf{p}(t), t), && (3.1\text{a}) \\ 0 &\geq \mathbf{g}(\mathbf{x}(t), \mathbf{u}(t), \mathbf{p}(t), t), && (3.1\text{b}) \\ 0 &= \mathbf{h}(\mathbf{x}(t), \mathbf{u}(t), \mathbf{p}(t), t), && (3.1\text{c}) \end{aligned}$$

where $\mathbf{x} \in \mathcal{X} \subseteq \mathbb{R}^{n_x}$ is a vector of the current states in the system, $\mathbf{u} \in \mathcal{U}(\mathbf{x}) \subseteq \mathcal{U} \subseteq \mathbb{R}^{n_u}$ is the applied control input at time t, $\mathbf{p}$ is a vector containing system parameter values at the current time instance, and $t \in \mathcal{T} = [t_0, t_N]$ is the time state which is defined between an initial time t_0 and a terminal time t_N. The vector-valued function $\mathbf{f}$ represents the system dynamics, which is piece-wise Lipschitz continuous. The inequality constraint function $\mathbf{g}$ and the equality constraint function $\mathbf{h}$ are also vector-valued, nonlinear, and differentiable functions that describe the values which the states $\mathbf{x}$ and control inputs $\mathbf{u}$ can take, given the parameters $\mathbf{p}$ and the time t. At the initial time $t = t_0$, the initial state is given and defined as an additional constraint $\mathbf{x}(t_0) = \mathbf{x_0} \in \mathcal{X}_0$, and at the final time instant t_N the target set $\mathcal{X}_N$ defines the terminal constraints $\mathbf{x}(t_N) \in \mathcal{X}_N$. This gives the full system description as, for $t \in \mathcal{T}$,

$$\begin{aligned} \dot{\mathbf{x}}(t) &= \mathbf{f}(\mathbf{x}(t), \mathbf{u}(t), \mathbf{p}(t), t), && (3.2\text{a}) \\ 0 &\geq \mathbf{g}(\mathbf{x}(t), \mathbf{u}(t), \mathbf{p}(t), t), && (3.2\text{b}) \\ 0 &= \mathbf{h}(\mathbf{x}(t), \mathbf{u}(t), \mathbf{p}(t), t), && (3.2\text{c}) \\ \mathbf{x}(t_0) &= \mathbf{x}_0 \in \mathcal{X}_0, \quad \mathbf{x}(t_N) \in \mathcal{X}_N, && (3.2\text{d}) \\ \mathbf{x}(t) &\in \mathcal{X}, \quad \mathbf{u}(t) \in \mathcal{U}(\mathbf{x}(t)). && (3.2\text{e}) \end{aligned}$$

The overall task in an optimal control problem (OCP) is to determine what the "best" sequence of control actions is. To define which control actions are desirable, an objective function is used

$$J(\mathbf{x}(t_0), \mathbf{u}(\cdot)) = \int_{t_0}^{t_N} l(\mathbf{x}(t), \mathbf{u}(t), \mathbf{p}(t), t)\mathrm{d}t + J_N(\mathbf{x}(t_N)), \tag{3.3}$$

here $l(\cdot) : \mathcal{X} \times \mathcal{U} \times \mathcal{P} \rightarrow \mathbb{R}$ is the stage cost function, $J_N : \mathcal{X} \rightarrow \mathbb{R}$ is the terminal cost function, and $\mathbf{x}(t)$ is a solution to the ODE (3.2) for the control inputs $\mathbf{u}(t)$. Given the cost function, the optimal control is found by minimizing the cost, which means solving the optimization problem

$$\begin{aligned} \underset{\mathbf{x}(t), \mathbf{u}(t),}{\text{minimize}} \quad & J(\mathbf{x}(t_0), \mathbf{u}(\cdot)) \\ \text{subject to} \quad & \dot{\mathbf{x}}(t) = \mathbf{f}(\mathbf{x}(t), \mathbf{u}(t), \mathbf{p}(t)) \qquad t \in \mathcal{T}, \\ & 0 \geq \mathbf{g}(\mathbf{x}(t), \mathbf{u}(t), \mathbf{p}(t)) \qquad t \in \mathcal{T}, \\ & 0 = \mathbf{h}(\mathbf{x}(t), \mathbf{u}(t), \mathbf{p}(t)) \qquad t \in \mathcal{T}, \\ & \mathbf{x}(t) \in \mathcal{X}, \quad \mathbf{u}(t) \in \mathcal{U}(\mathbf{x}(t)) \qquad t \in \mathcal{T}, \\ & \mathbf{x}(t_0) = \mathbf{x}_0 \in \mathcal{X}_0, \quad \mathbf{x}(t_N) \in \mathcal{X}_N. \end{aligned} \tag{3.4}$$

The following sections will describe some common methods for solving optimization problems such as the one formulated in equation (3.4).

3.1.1 Nonlinear optimization

Once the optimal control problem (3.4) is formulated, it is commonly rewritten into the form

$$\begin{aligned} \underset{\mathbf{z}}{\text{minimize}} \quad & f(\mathbf{z}) \\ \text{subject to} \quad & h_i(\mathbf{z}) = 0, \quad i = 1, ..., p, \\ & g_j(\mathbf{z}) \leq 0, \quad j = 1, ..., m \end{aligned} \tag{3.5}$$

which is the standard form for a NLP. Here $\mathbf{z} = [z_1, ..., z_n]^\top$ are the optimization variables, $\mathbf{h}(\mathbf{z}) = [h_1(\mathbf{z}), ..., h_p(\mathbf{z})]^\top$ are the equality constraints, and $\mathbf{g}(\mathbf{z}) = [g_1(\mathbf{z}), ..., g_m(\mathbf{z})]^\top$ are the inequality constraints. The optimal solution to this problem $\mathbf{z}^*$ consists of the values of $\mathbf{z}$ which gives the lowest cost function value $f(\mathbf{z})$ and belongs to the feasibility set

$$\mathcal{Z} = \{\mathbf{z} \in \mathbb{R}^n \mid \mathbf{h}(\mathbf{z}) = \mathbf{0},\ \mathbf{g}(\mathbf{z}) \leq \mathbf{0}\}. \tag{3.6}$$

This means that the global minimum, $\mathbf{z}^*$, must fulfill that $\mathbf{z}^* \in \mathcal{Z}$ and $\forall \mathbf{z} \in \mathcal{Z} : f(\mathbf{z}) \geq f(\mathbf{z}^*)$. For convex functions the solution to this problem becomes simpler, as these only allow for one global optimum to exist which is also equal to all local minima. However, for non-convex problems, this condition is usually not fulfilled and there might exist multiple points which are only local minima, and not global ones. A local minimum $\mathbf{z}^* \in \mathcal{Z}$ is a point that satisfies the condition that there exists a neighborhood $\mathcal{N}$ of $\mathbf{z}^*$ such that $\forall \mathbf{z} \in \mathcal{Z} \cap \mathcal{N} : f(\mathbf{z}) \geq f(\mathbf{z}^*)$. These conditions for local optimality are usually utilized by optimization methods to find the optimal solution $\mathbf{z}^*$ since all global optimums must also be local ones. In the case of unconstrained optimization, the conditions for local optimality are

$$\begin{aligned} &\mathbf{z}^* \text{ is a stationary point} \Rightarrow \nabla f(\mathbf{z}^*) = 0, \\ &\mathbf{z}^* \text{ is a strict local minimum} \Rightarrow \nabla f(\mathbf{z}^*) = 0,\ \nabla^2 f(\mathbf{z}^*) \succ 0. \end{aligned} \tag{3.7}$$

When constraints are present in the optimization problem, the local optimality conditions are extended into Karush-Kuhn-Tucker (KKT) conditions

$$\nabla f(\mathbf{z}^*) + \nabla \mathbf{g}(\mathbf{z}^*)\boldsymbol{\mu}^* + \nabla \mathbf{h}(\mathbf{z}^*)\boldsymbol{\lambda}^* = 0, \tag{3.8a}$$

$$\mathbf{g}(\mathbf{z}^*) \leq 0, \tag{3.8b}$$

$$\mathbf{h}(\mathbf{z}^*) = 0, \tag{3.8c}$$

$$\boldsymbol{\mu}^* \geq 0, \tag{3.8d}$$

$$\boldsymbol{\mu}_j^* \mathbf{g}_j(\mathbf{z}^*) = 0, \quad j = 1, ..., m. \tag{3.8e}$$

These equations are the basis for many optimization algorithms used to solve NLPs, such as sequential quadratic programming (SQP) and interior point (IP) methods. In this thesis, IP methods are used to solve the OCP and these are further elaborated upon in section 3.1.2. The KKT conditions are the first order necessary conditions for optimally (FONC) and thus are equivalent to $\nabla f(\mathbf{z}^*) = 0$ in unconstrained optimization. The points that fulfill the KKT conditions are referred to as “KKT points”, and these points are thus good points for the global optimum $\mathbf{z}^*$, however further checks need to be made to ensure optimality. For instance, KKT points $\mathbf{z}^*$ are only local minimizers whenever the linear independence constraint qualification (LICQ) holds at $\mathbf{z}^*$. The LICQ holds at a point $\mathbf{z}^* \in \mathcal{Z}$ iff all vectors $\nabla h_i(\mathbf{z}^*)$ for $i \in \{1, ..., p\}$ and $\nabla g_j(\mathbf{z}^*)$ for $j \in \mathcal{A}(\mathbf{z}^*)$ are linearly independent, where $\mathcal{A}(\mathbf{z}^*)$ are all indices $j \in \{1, ..., m\}$ for which $g_j(\mathbf{z}^*) = 0$.

The KKT conditions are strongly related to the Lagrangian function

$$\mathcal{L}(\mathbf{z}, \boldsymbol{\mu}, \boldsymbol{\lambda}) = f(\mathbf{z}) + \boldsymbol{\mu}^\top \mathbf{g}(\mathbf{z}) + \boldsymbol{\lambda}^\top \mathbf{h}(\mathbf{z}), \tag{3.9}$$

where we again use the variables $\boldsymbol{\mu} \in \mathbb{R}^m$ and $\boldsymbol{\lambda} \in \mathbb{R}^p$ which are hereafter named the “dual variables”. In the KKT conditions, it can then be noted that the first condition (3.8a) can be rewritten as $\nabla_{\mathbf{z}} \mathcal{L}(\mathbf{z}^*, \boldsymbol{\mu}^*, \boldsymbol{\lambda}^*) = 0$, which now closely relates to the unconstrained optimality conditions (3.6), but with the added complementarity conditions (3.8c)-(3.8e).

3.1.2 Interior point methods

With interior point methods, the approach to finding a solution is to smoothly approximate the complementarity conditions (3.8c)-(3.8e), typically using hyperbolas. This can be done by introducing a smoothening constant $\tau > 0$ to the KKT conditions which results in the system

$$\nabla f(\mathbf{z}^*) + \nabla \mathbf{g}(\mathbf{z}^*)\boldsymbol{\mu}^* + \nabla \mathbf{h}(\mathbf{z}^*)\boldsymbol{\lambda}^* = 0, \tag{3.10a}$$

$$\mathbf{h}(\mathbf{z}^*) = 0, \tag{3.10b}$$

$$\boldsymbol{\mu}_j^* \mathbf{g}_j(\mathbf{z}^*) + \tau = 0, \quad j = 1, ..., m. \tag{3.10c}$$

As the name of the methods suggests, interior point methods assume that the point $\mathbf{z}^*$ is interior to the problem, which in the smoothed system implies that both $-g_j(\mathbf{z}^*)$ and $\boldsymbol{\mu}_j^*$ are positive. By using equation (3.10c), $\boldsymbol{\mu}_j^*$ becomes

$$\boldsymbol{\mu}_j^* = -\frac{\tau}{g_j(\mathbf{z}^*)} > 0, \tag{3.11}$$

and it can also be noted that

$$\nabla_{\mathbf{z}} \log(-g_j(\mathbf{z})) = \frac{1}{g_j(\mathbf{z})} \nabla_{\mathbf{z}} g_j(\mathbf{z}), \tag{3.12}$$

thus the smoothed KKT conditions (3.10) become the optimality conditions for the barrier problem

$$\begin{aligned} \underset{\mathbf{z} \in \mathbb{R}^n}{\text{minimize}} \quad & f_\tau(\mathbf{z}) = f(\mathbf{z}) - \tau \sum_{j=1}^{m} \log(-g_j(\mathbf{z})) \\ \text{subject to} \quad & h_i(\mathbf{z}) = 0, \quad i = 1, ..., p. \end{aligned} \tag{3.13}$$

It can be noted that the barrier problem always ensures that the inequalities are satisfied, since $f_\tau(\mathbf{z}) \to \infty$ whenever $g_j(\mathbf{z}) \to 0$. By solving the barrier problem using Newton-type optimization the primal IP method is found for the value τ. The error introduced for these methods is of order $\mathcal{O}(\tau)$, which means that the error decreases linearly as $\tau \to 0$. This is shown in the example optimization problem in figure 3.1.

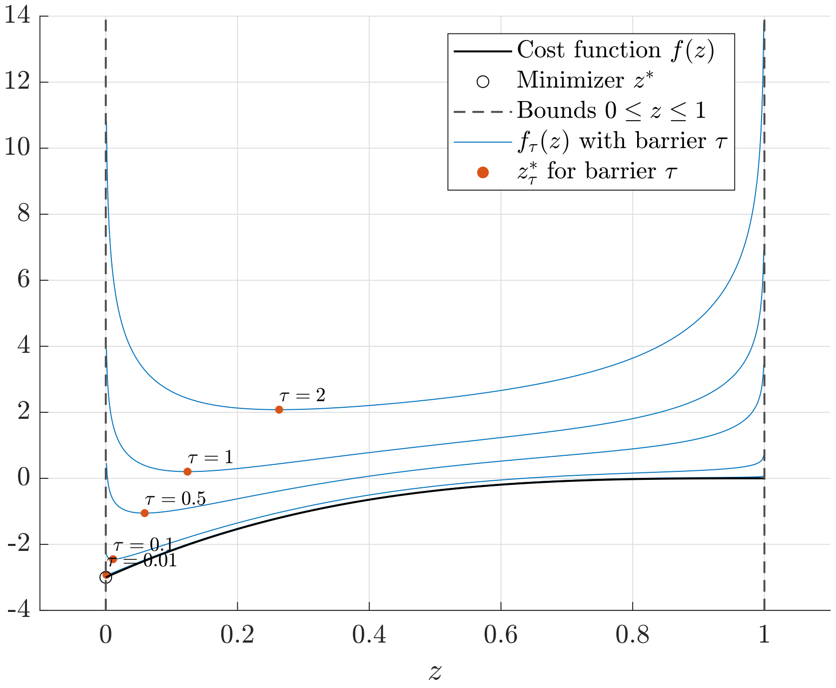

Figure 3.1: Schematic illustration of solutions to the barrier problem in (3.13) for smoothing parameters $\tau \in \{0.01, 0.1, 0.5, 1, 2\}$. The true cost function is given by $f(z) = 3(z-1)^3$ and it is optimized over the bounds $0 \leq z \leq 1$. Its optimum is given by $z^* = 0$, and for each τ the approximate solutions z_τ^* are shown alongside their respective approximate cost functions $f_\tau(z)$.

It can be noted that the same solutions $\mathbf{z}^*_\tau$ are yielded by solving both the barrier problem in (3.13) and the nonlinear equation system in (3.10). This gives rise to the primal-dual interior point method (PDIP) which solves the full equation system including the dual variables $\boldsymbol{\mu}$ typically using Newton iterations. The benefit of the PDIP over the primal IP method is that the KKT matrices become ill-conditioned for small values of τ in the primal IP method, which is avoided in the PDIP methods allowing for higher precision. In this thesis, PDIP methods are used to solve NLP problems that are encountered in mission management optimization.

3.1.3 Multiple shooting

It can be noted that performing long integrations of nonlinear system dynamics can introduce large numerical instabilities [50]. These kinds of integrations are commonly needed when discretizing continuous OCPs to solve them as NLPs and one way to improve stability is by using the "multiple shooting" method. In the multiple shooting method, each time interval $t \in [t_i, t_{i+1}]$ is then discretized using a pre-determined time grid, and for each interval, a separate ODE is solved. Additional constraints are then added such that continuity is ensured between each time interval, and by solving each interval separately better convergence properties can be achieved in comparison to solving an OCP for the complete time interval $\mathcal{T}$ [50].

3.2 Stochastic optimal control

In this section, an introduction will be given to stochastic optimal control theory, for more details of stochastic optimal control refer to [49], [51],[52],[53] and [54]. Only the theory for discrete-time stochastic optimal control will be presented here, and the theory of stochastic optimal control builds on the deterministic theory explained in the previous section.

3.2.1 Stochastic decision models

Consider a discrete-time stochastic system described by

$$\mathbf{x}_{k+1} = \mathbf{f}(\mathbf{x}_k, \mathbf{u}_k, \mathbf{w}_k), \tag{3.14}$$

where $\mathbf{x}_k$ and $\mathbf{x}_{k+1}$ represent a state and its succeeding state belonging to a state space $\mathcal{X} \subseteq \mathbb{R}^{n_x}$, $\mathbf{u}_k$ represents a decision variable chosen to fulfill a constraint set $\mathcal{U}(\mathbf{x}_k)$ which is a subset of all possible control inputs $\mathcal{U} \subseteq \mathbb{R}^{n_u}$. Let the disturbance $\mathbf{w}_k$ be a member of a probability space $(\Omega, \mathscr{F}, P)$, with a probability distribution $p(\mathrm{d}\mathbf{w}_k|\mathbf{w}_k, \mathbf{u}_k)$. This defines the sequences of random variables $\mathrm{w}_\infty : \Omega \to \mathcal{W}^\infty$, $\mathrm{w}_\infty = \{\mathbf{w}(k)\}_{k=0}^\infty$ for $\mathbf{w}(k) : \Omega \to \mathcal{W}$ with $\mathcal{W} \subseteq \mathbb{R}^{n_w}$. For a finite-horizon problem with N stages, we define the subsequence $\mathrm{w}_N : \Omega \to \mathcal{W}^N$ as $\mathrm{w}_N = \{\mathbf{w}(0), ..., \mathbf{w}(N-1)\}$. Further, it is assumed that all $\mathbf{w}(k)$ are i.i.d and that $\mathcal{W}$ is compact and contains the origin.

For each stage, the cost is defined by some function $l(\mathbf{x}_k, \mathbf{u}_k, \mathbf{w}_k)$, which is Borel measurable. For this cost function, the finite sequence of control functions (the policy) $\boldsymbol{\pi} = (\boldsymbol{\mu}_0, ..., \boldsymbol{\mu}_{N-1})$ is sought. The control functions $\boldsymbol{\mu}_k$ depends on the available information, meaning that for the first stage $\mathbf{u}_0 = \boldsymbol{\mu}_0(\mathbf{x}_0)$, after which the control action for stage k is given by

$$\mathbf{u}_k = \boldsymbol{\mu}_k(\mathbf{x}_0, \mathbf{u}_0, ..., \mathbf{u}_{k-1}, \mathbf{x}_k) \in \mathcal{U}(\mathbf{x}_k). \quad \forall k. \tag{3.15}$$

In contrast to deterministic optimal control, where the objective is to select an optimal sequence of control variables that minimizes the total cost over all stages N, in stochastic optimal control the goal is to select a policy $\boldsymbol{\pi}$ such that the expected value of the total cost is minimized. It is assumed that Markov properties hold for the stochastic system, which implies that we can simplify the expression for $\mathbf{u}_k$ to $\mathbf{u}_k = \boldsymbol{\mu}_k(\mathbf{x}_k)$. This means that we seek $\boldsymbol{\pi}$ which minimizes the expression

$$\begin{aligned} J_{N,\boldsymbol{\pi}}(\mathbf{x}_0) &= \mathbb{E}_{\mathbf{w}_k}\left[\sum_{k=0}^{N} l_k(\mathbf{x}_k, \boldsymbol{\mu}_k(\mathbf{x}_k), \mathbf{w}_k)\right] \\ &= J_N(\mathbf{x}_N)p(\mathbf{x}_N) + \sum_{k=0}^{N-1}\int_{\Omega} l(\mathbf{x}_k, \boldsymbol{\mu}_k(\mathbf{x}_k), \mathbf{w}_k)p(\mathrm{d}\mathbf{x}_k|\mathbf{x}_{k-1}, \boldsymbol{\mu}_{k-1}(\mathbf{x}_{k-1})), \end{aligned} \tag{3.16}$$

where $J_N(\cdot) = l_N$ represents the cost in the final stage, and for all other stages $l_k(\cdot) = l(\cdot)$. In the next section, the framework for stochastic dynamic programming will be presented, which can be used to solve stochastic optimal control problems.

3.2.2 Stochastic dynamic programming

The SDP algorithm utilizes Bellman's principle of optimality [21] to recursively find the optimal policy $\boldsymbol{\pi}^*$ which minimizes

$$J_{N,\boldsymbol{\pi}^*}(\mathbf{x}_0) = J_N^*(\mathbf{x}_0) = \min_{\boldsymbol{\pi}\in\Pi} J_{N,\boldsymbol{\pi}}(\mathbf{x}_0), \tag{3.17}$$

where Π is the set of all possible policies. The principle can be stated as follows, given a policy $\boldsymbol{\pi}^* = \{\boldsymbol{\mu}_0^*, ..., \boldsymbol{\mu}_{N-1}^*\}$ which minimizes the N-stage cost function in (3.15), then the "tail policy" $\boldsymbol{\pi}_i^* = \{\boldsymbol{\mu}_i^*, ..., \boldsymbol{\mu}_{N-1}^*\}$ is the optimal policy to the "tail subproblem"

$$J_{N,\boldsymbol{\pi}^*}(\mathbf{x}_i) = \min_{\boldsymbol{\pi}\in\Pi} J_{N,\boldsymbol{\pi}}(\mathbf{x}_i) = \min_{\boldsymbol{\pi}\in\Pi} \mathbb{E}_{\mathbf{w}_k}\left[J_N(\mathbf{x}_N) + \sum_{k=i}^{N-1} l(\mathbf{x}_k, \boldsymbol{\mu}_k(\mathbf{x}_k), \mathbf{w}_k)\right]. \tag{3.18}$$

The SDP algorithm then solves the OCP in (3.17) by the following steps. First start with a terminal state $\mathbf{x}_N$ and the terminal cost function

$$J_N(\mathbf{x}_N) = l_N(\mathbf{x}_N). \tag{3.19}$$

Then iterate backward until the first stage by

$$J_k(\mathbf{x}_k) = \min_{\mathbf{u}_k\in\mathcal{U}(\mathbf{x}_k)} \mathbb{E}_{\mathbf{w}_k}\left[l(\mathbf{x}_k, \mathbf{u}_k, \mathbf{w}_k) + J_{k+1}\left(f(\mathbf{x}_k, \mathbf{u}_k, \mathbf{w}_k)\right)\right], \quad k = N-1, ..., 0, \tag{3.20}$$

where $\mathbf{x}_k$ solves the stochastic ODE (3.14) and $\mathbf{x}_k$, $\mathbf{x}_{k+1} \in \mathcal{X}$ $\forall k$.

4

Problem formulation

In this chapter, the mission management optimization problem will be formulated using the dynamics described in chapter 2 and the optimal control theory in chapter 3.

4.1 Continuous time problem formulation

The purpose of the mission manager is to optimally plan charging concerning the battery SoC, temperature, and the time of day for a given speed trajectory. The battery temperature is controlled by a thermal system that uses the reference battery temperature T_b^{ref} as input. During driving the friction brake force F_{brake} is also a control input, which is heavily penalized to encourage regenerative braking instead, and during charging both the charging power P_{stat} and the total charging time t_{chg} are control inputs. These states and inputs are then summarized in the following vectors, shown together with the parameter vector $\mathbf{p}$

$$\mathbf{x}(t) = \begin{bmatrix} t \\ \mathrm{soc}(t) \\ T_b(t) \end{bmatrix}, \quad \mathbf{u}(t) = \begin{bmatrix} t_{chg}(t) \\ P_{stat}(t) \\ T_b^{ref}(t) \\ F_{brake}(t) \end{bmatrix}, \tag{4.1}$$

$$\mathbf{p}(t) = \begin{bmatrix} v(t) & \alpha(t) & \rho_a(t) & \theta_{wind}(t) & v_{wind}(t) & C_{rr}(t) & T_{amb}(t) & L_s(t) & q(t) \end{bmatrix}^\top,$$

where $q(t)$ is a function that represents the total station-dependent time that the truck needs to queue before it can start charging at a station. The dynamics of the states are found using the modeling presented in chapter 2. The SoC dynamics are given by equation (2.20)

$$\dot{\mathrm{soc}}(t) = -\eta_c \frac{P_b(t) + \frac{R_{eq}(\mathrm{soc}(t),T_b(t))P_b(t)^2}{n_s^2 u_{oc}^2(\mathrm{soc}(t),T_b(t))}}{E_{cap}}, \tag{4.2}$$

which also gives the power balance equation

$$P_b(t) + P_{stat}(t) = P_{hc}(T_b(t), T_b^{ref}(t) + P_{aux}(t) + P_{EM}(v(t), F_T(t)). \tag{4.3}$$

Here the charging power $P_{stat}(t)$ can only be applied at charging stations where a stop is made. To handle this, the charging decision variable

$$\zeta(t) = \begin{cases} 1, & t_{chg}(t) > 0, \\ 0, & \text{otherwise}, \end{cases} \tag{4.4}$$

is introduced, and from this the constraint on the charging power becomes

$$P_{stat}(t) \in \begin{cases} [0, \zeta(t) P_{stat}^{max}(s(t))], & s(t) \in \mathcal{S}_{chg}, \\ 0, & s(t) \in \mathcal{S}_{drv}, \end{cases} \tag{4.5}$$

where $s(t)$ is the current position of the truck, $\mathcal{S}_{chg}$ is a set representing the positions of all charging stations along the route, and $\mathcal{S}_{drv}$ is a set containing the remaining positions which do not contain charging stations. The charging power P_{stat}^{max} represents the capacity of the charging station and thus depends on which station the truck is currently being charged at. The battery thermal dynamics are given by equation (2.33)

$$\dot{T}_b(t) = \frac{1}{c_{p,b} m_b} \left(Q_{gen}(\cdot) + Q_{act}(T_b(t), T_b^{ref}(t)) \right). \tag{4.6}$$

The dynamics in equations (4.2) and (4.5), together with the trivial time dynamics $\dot{t}(t) = 1$, are summarized in the vector-valued function $\mathbf{f}(\cdot)$ defined by

$$\dot{\mathbf{x}}(t) = \mathbf{f}(\mathbf{x}(t), \mathbf{u}(t), \mathbf{p}(t)), \tag{4.7}$$

and the power balance equation (4.3) is summarized as the function

$$P_b(t) = h(\mathbf{x}(t), \mathbf{u}(t), \mathbf{p}(t)). \tag{4.8}$$

Because of physical limitations on the truck, not all pairs of inputs and outputs are allowed. Firstly, the traction effort is $F_T(t)$ is constrained by the speed-dependent traction effort bounds seen in figure 2.8, which is represented by the time-dependent inequalities

$$F_T^{min}(v(t)) \leq F_T(t) \leq F_T^{max}(v(t)). \tag{4.9}$$

Further, the battery power is limited by the lookup tables shown in figure 2.6, which gives the inequalities

$$P_{b,ch}^{min}(\text{soc}(t), T_b(t)) \leq P_b(t) \leq (1 - \zeta(t)) P_{b,dch}^{max}(\text{soc}(t), T_b(t)) \tag{4.10}$$

where the battery is not allowed to be discharged whenever the truck is stopped at a charging station, hence the upper limit of $P_b(t) \leq 0$ whenever $\zeta(t) = 1$. As was mentioned previously, each station has maximum capacity $P_{stat}^{max}(s(t))$, but the provided charging power is also limited by the maximum charging power of the truck which is denoted P_{chg}^{max} meaning that the limits on charging power are further expanded to

$$0 \leq P_{stat}(t) \leq \zeta(t) \min(P_{stat}^{max}(s(t)), P_{chg}^{max}) \tag{4.11}$$

The SoC is constrained to the range $\text{soc}^{min} - \text{soc}^{max}$ to limit battery degradation, meaning that

$$\text{soc}^{min} \leq \text{soc}(t) \leq \text{soc}^{max}, \tag{4.12}$$

and the battery temperature is kept in the range

$$T_b^{min} \leq T_b(t) \leq T_b^{max}. \tag{4.13}$$

The charging time $t_{chg}(t)$ is constrained to a maximum total charging time t_{chg}^{max}, which gives that

$$0 \leq t_{chg}(t) \leq t_{chg}^{max}. \tag{4.14}$$

The constraints are summarized in the vector-valued function $\mathbf{g}(\cdot)$ defined as

$$\mathbf{g}(\mathbf{x}(t), \mathbf{u}(t), \mathbf{p}(t)) = \begin{bmatrix} F_T(t) - F_T^{max}(v(t)) \\ F_T^{min}(v(t)) - F_T(t) \\ P_b(t) - (1 - \zeta(t)) P_{b,dch}^{max}(\mathrm{soc}(t), T_b(t)) \\ P_{b,ch}^{min}(\mathrm{soc}(t), T_b(t)) - P_b(t) \\ P_{stat}(t) - \zeta(t) \min(P_{stat}^{max}(s(t)), P_{chg}^{max}) \end{bmatrix}, \tag{4.15}$$

and the affine constraint sets $\mathcal{X}$ and $\mathcal{U}$, with $\mathcal{T} = [t_N - t_{max}, t_N]$ defining the allowed time span for the trip where t_N is the arrival time and t_{max} is the maximum trip time,

$$\begin{aligned} \mathcal{X} &= \{\mathbf{x} \in \mathbb{R}^3 \mid t \in \mathcal{T}, \mathrm{soc} \in [\mathrm{soc}^{min}, \mathrm{soc}^{max}], T_b \in [T_b^{min}, T_b^{max}]\}, \\ \mathcal{U} &= \{\mathbf{u} \in \mathbb{R}^4 \mid t_{chg} \in [0, t_{chg}^{max}], P_{stat} \in [0, P_{chg}^{max}], T_b^{ref} \in [T_b^{min}, T_b^{max}], F_{brake} \geq 0\}. \end{aligned} \tag{4.16}$$

The objective of the optimizer is to minimize the TCOP of the mission, which includes a mix of time and energy optimal control. In this thesis, the following formulation is used

$$\begin{aligned} J(\cdot) = \int_{t_0}^{t_N} \Big(& c_\delta \delta(t) + c_d L_s(t)(F_T(t) + F_{t,loss}(t)) + c_b F_{brake}^2(t) \\ & + \zeta(t)(c_\zeta + c_c(t) P_{stat}(t) + c_{cr} C_r(t)(27 - T_b(t))^2) + c_t \Big) \,\mathrm{d}t, \end{aligned} \tag{4.17}$$

where c_δ, c_d, c_t, c_{cr}, and c_b are constant cost parameters given in Swedish crowns. The charging cost $c_c^i(t)$ is both time and station-dependent and c_δ is a per-station detour cost to penalize each decision to stop at a station Here $\delta(t)$ represents slack variables, which are introduced for numerical stability to soften the constraints (4.15). This enables the solver to step outside of the feasibility set while searching for a solution, but these constraint violations are heavily penalized in the cost function. The objective function consists of the following parts

- $c_\delta \delta(t)$: a cost on constraint violations.
- $c_d L_s(t)(F_T(t) + F_{T,loss}(t))$: a cost on the energy consumption from driving, where $L_s(t)$ is the spatial discretization step.
- $c_b F_{brake}^2(t)$: a high penalty on the friction brake usage.
- $\zeta(t) c_\zeta$: a constant cost on detouring to stations.
- $\zeta(t) c_c(t) P_{stat}(t)$: the cost of charging energy at a station.
- $\zeta(t) c_{cr} C_r(t)(27 - T_b(t))^2$: a cost on high C-rate charging and temperature deviations.
- c_t: a cost on the trip time.

Using the dynamics $\mathbf{f}(\cdot)$, the power balance constraint $h(\cdot)$, the inequality constraints $\mathbf{g}(\cdot)$ and the cost function $J(\cdot)$, the mission management optimization problem is formulated as

$$\underset{\mathbf{u}(t), t_0, \zeta}{\text{minimize}} \quad J(\cdot) \tag{4.18a}$$

$$\begin{aligned}
\text{subject to} \quad \frac{\mathrm{d}\mathbf{x}_{drv}(s)}{\mathrm{d}s} &= \mathbf{f}(\mathbf{x}(t), \mathbf{u}(t), \mathbf{p}(t)) \quad && t \in \mathcal{T}, && \text{(4.18b)}\\
0 &\geq \mathbf{g}(\mathbf{x}(t), \mathbf{u}(t), \mathbf{p}(t)) \quad && t \in \mathcal{T}, && \text{(4.18c)}\\
P_b(t) &= h(\mathbf{x}(t), \mathbf{u}(t), \mathbf{p}(t)) \quad && t \in \mathcal{T}, && \text{(4.18d)}\\
\mathbf{x}(t) \in \mathcal{X}, &\quad \mathbf{u}(t) \in \mathcal{U} && t \in \mathcal{T}, && \text{(4.18e)}\\
t &\leq t_0 + t_{max} && t \in \mathcal{T}, && \text{(4.18f)}\\
\mathbf{x}(t_0) \in \mathcal{X}_0, &\quad \mathbf{x}(t_N) \in \mathcal{X}_N, && && \text{(4.18g)}
\end{aligned}$$

where $\mathcal{X}_0$ are allowed initial states and $\mathcal{X}_N$ are the final state constraints. The final time t_N is a mission-specific parameter that specifies when the truck should arrive at the latest, but the initial time t_0 is instead treated as a design parameter that specifies when the truck should depart.

4.2 Hybrid dynamical system formulation

To solve the optimization problem (4.18), both SDP and the FORCESPRO NLP [55], [56] solver will be used. Both methods require the continuous-time dynamics presented in section 4.1 to be discretized. The choice of sampling strategy is not trivial, during driving space sampling greatly simplifies the problem since this fixes the position of road topographies and the location of recharging stations in the optimization. However, during charging the battery states will change over time while the truck is standing still, which means that time sampling is appropriate while the truck is stopped at charging stations. Since fully charging truck batteries can take several hours, time-dependent parameters such as the traffic speed can vary significantly and thus it is of interest to consider both time and space sampling for the problem, split into charging and driving modes. To enable this sampling strategy, the continuous time dynamics are reformulated into a hybrid dynamical system in the following sections, which is illustrated in figure 4.1.

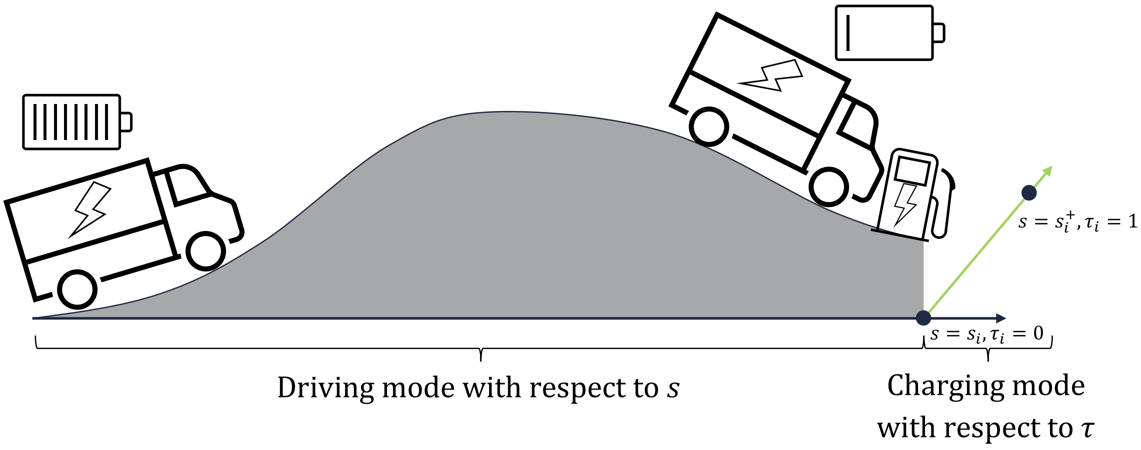

Figure 4.1: Illustration of the hybrid dynamics used in the optimization problem.

4.2.1 Driving mode

During driving mode the space samples s are considered independent of time t, meaning that decisions are made based on the current road sample. This allows the road topography to become a fixed trajectory $\alpha(s)$, and the traffic speed $v(s,t)$ becomes a time-varying parameter with a predetermined spatial variation depending on road speed limits. The states that are optimized are time t, state of charge soc, and battery temperature T_b. These states are optimized using the reference battery temperature T_b^{ref} and the friction braking force F_{brake}. To separate the states during charging and driving mode, the labels *drv* and *chg* are introduced. In summary, for the driving mode, we have the following states, inputs, and parameters

$$\mathbf{x}_{drv}(s) = \begin{bmatrix} t^{drv}(s) \\ \mathrm{soc}^{drv}(s) \\ T_b^{drv}(s) \end{bmatrix}, \quad \mathbf{u}_{drv}(s) = \begin{bmatrix} T_b^{ref,drv}(s) \\ F_{brake}(s) \end{bmatrix}, \tag{4.19}$$

$$\mathbf{p}_{drv}(s) = \begin{bmatrix} v(s) & \alpha(s) & \rho_a(s) & \theta_{wind}(s) & v_{wind}(s) & C_{rr}(s) & T_{amb}^{drv}(s) & L_s(s) \end{bmatrix}^\top,$$

where $\mathbf{p}_{drv}$ is a vector containing the problem parameters during driving stages. The chain rule gives the relation between time and space derivatives as

$$\frac{\mathrm{d}}{\mathrm{d}t} = \frac{\mathrm{d}s}{\mathrm{d}t}\frac{\mathrm{d}}{\mathrm{d}s} = v(s)\frac{\mathrm{d}}{\mathrm{d}s}, \quad t \in \mathcal{T}_{drv}, \; s \in \mathcal{S}_{drv}. \tag{4.20}$$

Using this, the space derivative of time t becomes

$$\frac{\mathrm{d}t^{drv}(s)}{\mathrm{d}s} = \frac{1}{v(s)}, \tag{4.21}$$

using the continuous-time dynamics, the spatial SoC dynamics become

$$\frac{\mathrm{dsoc}^{drv}(s)}{\mathrm{d}s} = -\eta_c \frac{P_b^{drv}(s) + \frac{R_{eq}(\mathrm{soc}^{drv}(s), T_b^{drv}(s)) P_b^{drv}(s)^2}{n_s^2 u_{oc}^2(\mathrm{soc}^{drv}(s), T_b^{drv}(s))}}{v(s) E_{cap}}. \tag{4.22}$$

The spatial power balance equation is given by

$$P_b^{drv}(s) = P_{hc}(T_b^{drv}(s), T_b^{ref,drv}(s)) + P_{aux}^{drv}(s) + P_{EM}(v(s), F_T(s)), \tag{4.23}$$

where $P_{stat} = 0$ since no charging can happen during the driving. For thermal management the spatial dynamics are

$$\frac{\mathrm{d}T_b^{drv}(s)}{\mathrm{d}s} = \frac{1}{c_{p,b} m_b v(s)} \Big(Q_{gen}(\cdot) + Q_{act}(T_b^{drv}(s), T_b^{ref,drv}(s)) \Big) \tag{4.24}$$

The driving dynamics in equations (4.21), (4.22) and (4.24) are summarized as the vector-valued function $\mathbf{f}_{drv}(\cdot)$, defined as

$$\frac{\mathrm{d}\mathbf{x}_{drv}(s)}{\mathrm{d}s} = \mathbf{f}_{drv}(\mathbf{x}_{drv}(s), \mathbf{u}_{drv}(s), \mathbf{p}_{drv}(s)). \tag{4.25}$$

The power balance equation (4.23) is summarized as the function $h_{drv}(\cdot)$ defined as

$$P_b^{drv}(s) = h_{drv}(\mathbf{x}_{drv}(s), \mathbf{u}_{drv}(s), \mathbf{p}_{drv}(s)). \tag{4.26}$$

4.2.2 Charging mode

During charging mode, the state, input, and parameters for each charging station $i \in \mathcal{I}$ are separated and denoted

$$\mathbf{x}^i_{chg}(\tau_i) = \begin{bmatrix} t_i^{chg}(\tau_i) \\ \mathrm{soc}_i^{chg}(\tau_i) \\ T_{b,i}^{chg}(\tau_i) \end{bmatrix}, \quad \mathbf{u}^i_{chg}(\tau_i) = \begin{bmatrix} t^i_{chg}(\tau_i) \\ T_{b,i}^{ref,chg}(\tau_i) \\ P_{stat,i} \end{bmatrix}, \quad \mathbf{p}^i_{chg}(\tau_i) = \begin{bmatrix} T^{chg}_{amb,i}(\tau_i) \\ q^i \end{bmatrix}, \tag{4.27}$$

where the charging power $P_{stat,i}$ is treated as a control input to allow for charging at less power than the maximum. To enable dynamic charging power limits, a normalized charging time variable $\tau_i \in [0,1]$ is introduced for each charging station as

$$\tau_i = \frac{t_i^{chg}}{t^i_{chg}}, \quad i \in \mathcal{I}, \tag{4.28}$$

where $t_i^{chg} \in [0, t^i_{chg}]$ is the current time at the charger and t^i_{chg} is the total charging time at station i. The chain rule gives the relation between time derivatives and the derivative with respect to τ_i as

$$\frac{\mathrm{d}}{\mathrm{d}t} = \frac{1}{t^i_{chg}} \frac{\mathrm{d}}{\mathrm{d}\tau_i}, \quad s(t) = s_i, \tag{4.29}$$

which gives the time dynamics as

$$\frac{\mathrm{d}t(\tau_i)}{\mathrm{d}\tau_i} = t^i_{chg}. \tag{4.30}$$

The SoC dynamics during charging become

$$\frac{\mathrm{dsoc}_i^{chg}(\tau_i)}{\mathrm{d}\tau_i} = -\eta_c \frac{t^i_{chg}\left(P^{chg}_{b,i}(\tau_i) + \frac{R_{eq}(\mathrm{soc}_i^{chg}(\tau_i), T^{chg}_{b,i}(\tau_i)) P^{chg}_{b,i}(\tau_i)^2}{n_s^2 u_{oc}(\mathrm{soc}_i^{chg}(\tau_i), T^{chg}_{b,i}(\tau_i))}\right)}{E_{cap}}. \tag{4.31}$$

During charging no propulsion happens and thus the power balance equation becomes

$$P^{chg}_{b,i}(\tau_i) + P_{stat,i}(\tau_i) = P_{hc}(T^{chg}_{b,i}(\tau_i), T^{ref,chg}_{b,i}(\tau_i)) + P^{chg}_{aux,i}(\tau_i). \tag{4.32}$$

During charging, the thermal dynamics are given by

$$\frac{\mathrm{d}T^{chg}_{b,i}(\tau_i)}{\mathrm{d}\tau_i} = \frac{t^i_{chg}}{c_{p,b} m_b}\Big(Q_{gen}(\cdot) + Q_{act}(T^{chg}_{b,i}(\tau_i), T^{ref,chg}_{b,i}(\tau_i))\Big) \tag{4.33}$$

The charging dynamics at station i in equations (4.30), (4.31) and (4.33) are summarized as the vector-valued function $\mathbf{f}_{chg}(\cdot)$, defined as

$$\frac{\mathrm{d}\mathbf{x}^i_{chg}(\tau_i)}{\mathrm{d}\tau_i} = \mathbf{f}_{chg}(\mathbf{x}^i_{chg}(\tau_i), \mathbf{u}^i_{chg}(\tau_i), \mathbf{p}^i_{chg}(\tau_i)). \tag{4.34}$$

The power balance equation (4.32) is summarized as the function $h_{chg}(\cdot)$ defined as

$$P^{chg}_{b,i}(\tau_i) = h_{chg}(\mathbf{x}^i_{chg}(\tau_i), \mathbf{u}^i_{chg}(\tau_i), \mathbf{p}^i_{chg}(\tau_i)). \tag{4.35}$$

4.3 Bounds on inputs and variables

Using the hybrid dynamics formulated in section 4.4 together with the constraints formulated in section 4.1, the vector-valued functions $\mathbf{g}_{drv}(\cdot)$ and $\mathbf{g}_{chg}(\cdot)$ which define the constraints functions during the driving respectively charging modes become

$$
\begin{aligned}
\mathbf{g}_{drv}(\mathbf{x}_{drv}(s), \mathbf{u}_{drv}(s), \mathbf{p}_{drv}(s)) &= \begin{bmatrix} F_T(s) - F_T^{max}(v(s)) \\ F_T^{min}(v(s)) - F_T(s) \\ P_b^{drv}(s) - P_{b,dch}^{max}(\mathrm{soc}^{drv}(s), T_b^{drv}(s)) \\ P_{b,ch}^{min}(\mathrm{soc}^{drv}(s), T_b^{drv}(s)) - P_b^{drv}(s) \end{bmatrix}, \\
\mathbf{g}_{chg}(\mathbf{x}_{chg}^{i}(\tau_i), \mathbf{u}_{chg}^{i}(\tau_i), \mathbf{p}_{chg}^{i}(\tau_i)) &= \begin{bmatrix} P_{b,i}^{chg}(\tau_i) \\ P_{b,ch}^{min}(\mathrm{soc}_i^{chg}(\tau_i), T_{b,i}^{chg}(\tau_i) - P_{b,i}^{chg}(\tau_i)) \\ P_{stat,i}(\tau_i) - \zeta_i \min(P_{stat,i}^{max}, P_{chg}^{max}) \end{bmatrix},
\end{aligned}
\tag{4.36}
$$

where the variable ζ_i represents the decision to stop and charge at station i. The affine constraint sets for states and inputs $\mathcal{X}_{drv}, \mathcal{X}_{chg}, \mathcal{U}_{drv}$ and $\mathcal{U}_{chg}$ are defined as

$$
\begin{aligned}
\mathcal{X}_{drv} &= \{\mathbf{x}_{drv} \in \mathbb{R}^3 \mid t^{drv} \in \mathcal{T}, \mathrm{soc}^{drv} \in [\mathrm{soc}^{min}, \mathrm{soc}^{max}], T_b^{drv} \in [T_b^{min}, T_b^{max}]\}, \\
\mathcal{X}_{chg}^{i} &= \{\mathbf{x}_{chg}^{i} \in \mathbb{R}^3 \mid t_i^{chg} \in \mathcal{T}, \mathrm{soc}_i^{chg} \in [\mathrm{soc}^{min}, \mathrm{soc}^{max}], T_{b,i}^{chg} \in [T_b^{min}, T_b^{max}]\}, \\
\mathcal{U}_{drv} &= \{\mathbf{u}_{drv} \in \mathbb{R}^2 \mid T_b^{ref,drv} \in [T_b^{min}, T_b^{max}], F_{brake} \geq 0\}, \\
\mathcal{U}_{chg}^{i} &= \{\mathbf{u}_{chg}^{i} \in \mathbb{R}^3 \mid t_{chg}^{i} \in [0, t_{chg}^{max}], P_{stat,i} \in [0, P_{chg}^{max}], T_{b,i}^{ref,chg} \in [T_b^{min}, T_b^{max}]\}.
\end{aligned}
\tag{4.37}
$$

4.4 Objective function

To achieve the TCOP optimization in the hybrid dynamics formulation, the objective function in equation (4.17) is split into two parts. The driving mode objective is described in section 4.4.1 and the charging mode objective is found in section 4.4.2.

4.4.1 Driving mode

For normal space samples where no charging is performed, only space sampling is used. The objective function for these samples is defined as

$$
J_{drv}(\cdot) = \sum_{s \in \mathcal{S}_{drv}} c_\delta \delta(s) + c_d L_s(s)(F_T(s) + F_{T,loss}(s)) + c_t \Delta t(s) + c_b F_{brake}^2(s). \tag{4.38}
$$

The cost function consists of four terms

- $c_\delta \delta(s)$: a penalty on constraint violations by c_δ which is set very high to only allow constraint violations if the problem otherwise becomes infeasible.
- $c_d L_s(s)(F_T(s) + F_{T,loss}(s))$: a cost for the energy consumed while driving.
- $c_t \Delta t(s)$: a cost on the travel time during the sample.
- $c_b F_{brake}^2(s)$: a high penalty on friction brake usage, to minimize energy losses.

4.4.2 Charging mode

For samples with charging stations, the following cost function is used instead

$$
\begin{aligned}
J_{chg}(\cdot) = \sum_{i=1}^{N_{chg}} c_\delta \delta(s_i) + \zeta_i \Big(t^i_{chg} \int_0^1 \left(c^i_c(t^{chg}_i(\tau_i)) P^i_{stat}(\tau_i) + c_{cr} C_r(\tau_i)(27 - T_b)^2 \right) \mathrm{d}\tau_i \\
+ c_t t^{chg}_i(1) + c_\zeta \Big),
\end{aligned} \tag{4.39}
$$

The cost function includes

- $c_\delta \delta(s)$: a penalty on constraint violations by c_δ.
- $t^i_{chg} \int_0^1 c^i_c(t(s_i)) P^i_{stat}(\tau_i) \mathrm{d}\tau_i$: a cost on the supplied energy to the vehicle from a charging station.
- $c_{cr} C_{r,i}(\tau_i)(27 - T_{b,i})^2$: a cost on the battery C-rate and temperature deviations during charging.
- $c_t t^{chg}_i(1)$: a cost on the time spent charging and queuing.
- c_ζ: a penalty on each charging decision.

4.5 Full optimization problem

The MIP formulation for $i \in \mathcal{I}, \tau_i \in [0,1]$ is stated as

$$
\begin{aligned}
\underset{\mathbf{u}_{drv}(s), \mathbf{u}^i_{chg}(\tau_i), t_0}{\text{minimize}} \quad & J_{drv}(\cdot) + J_{chg}(\cdot) && && \text{(4.40a)} \\
\text{subject to} \quad & && && \\
\frac{\mathrm{d}\mathbf{x}_{drv}(s)}{\mathrm{d}s} &= \mathbf{f}_{drv}(\mathbf{x}_{drv}(s), \mathbf{u}_{drv}(s), \mathbf{p}_{drv}(s)) && s \in \mathcal{S}_{drv}, && \text{(4.40b)} \\
\frac{\mathrm{d}\mathbf{x}^i_{chg}(\tau_i)}{\mathrm{d}\tau_i} &= \mathbf{f}_{chg}(\mathbf{x}^i_{chg}(\tau_i), \mathbf{u}^i_{chg}(\tau_i), \mathbf{p}^i_{chg}(\tau_i)) && s \in s_i, && \text{(4.40c)} \\
0 &\geq \mathbf{g}_{drv}(\mathbf{x}_{drv}(s), \mathbf{u}_{drv}(s), \mathbf{p}_{drv}(s)) && s \in \mathcal{S}_{drv}, && \text{(4.40d)} \\
0 &\geq \mathbf{g}_{chg}(\mathbf{x}^i_{chg}(\tau_i), \mathbf{u}^i_{chg}(\tau_i), \mathbf{p}^i_{chg}(\tau_i)) && s \in s_i, && \text{(4.40e)} \\
P^{drv}_b(s) &= h_{drv}(\mathbf{x}_{drv}(s), \mathbf{u}_{drv}(s), \mathbf{p}_{drv}(s)) && s \in \mathcal{S}_{drv}, && \text{(4.40f)} \\
P^{chg}_{b,i}(\tau_i) &= h_{chg}(\mathbf{x}^i_{chg}(\tau_i), \mathbf{u}^i_{chg}(\tau_i), \mathbf{p}^i_{chg}(\tau_i)) && s \in s_i, && \text{(4.40g)} \\
\mathbf{x}_{drv}(s) \in \mathcal{X}_{drv}, &\quad \mathbf{u}_{drv}(s) \in \mathcal{U}_{drv} && s \in \mathcal{S}_{drv}, && \text{(4.40h)} \\
\mathbf{x}^i_{chg}(\tau_i) \in \mathcal{X}^i_{chg}, &\quad \mathbf{u}^i_{chg}(\tau_i) \in \mathcal{U}^i_{chg} && s \in s_i, && \text{(4.40i)} \\
\mathbf{x}^i_{chg}(0) &= \mathbf{x}_{drv}(s_i) - \zeta_i \mathbf{x}^i_{detour}, && && \text{(4.40j)} \\
\mathbf{x}_{drv}(s^+_i) &= \mathbf{x}^i_{chg}(1) - \zeta_i \mathbf{x}^i_{detour}, && && \text{(4.40k)} \\
\mathbf{x}_{drv}(s_0) \in \mathcal{X}_0, &\quad \mathbf{x}_{drv}(s_N) \in \mathcal{X}_N && && \text{(4.40l)}
\end{aligned}
$$

where s_0 and s_N denote the initial respective final space sample of the trip, s^+_i represents the space sample of a charging station when the vehicle is leaving the station, $\mathcal{X}_{drv}$ and $\mathcal{X}_{chg}$ represent the feasibility sets of the states during the different modes, $\mathcal{X}_0$ and $\mathcal{X}_N$ are the initial respective final feasibility sets, $\mathcal{U}_{drv}$ and $\mathcal{U}_{chg}$ are the feasibility sets for the control inputs. The parameter $\mathbf{x}^i_{detour}$ is used to approximate the state changes resulting from the detour to charging station i from space sample s_i. Thus the constraints (4.40j) and (4.40k) represent the mode transition between driving and charging modes at the charging stations. These transitions consist of three parts, first the truck drives a detour distance L^i_{detour} from the route to the station. Once at the station, it queues for the time q^i before accessing the charger. This queuing is simulated by running the charging dynamics for the time q^i with the charging power 0. After charging it drives back the same distance L^i_{detour} to the route.

4.6 Hierarchical formulation

To solve the full optimization problem, it is split into two levels. The first level optimizes the battery SoC trajectory using the charging times t^i_{chg} and the mission starting time t_0. During this optimization stage, the control of battery temperatures is excluded with T_b set constant to 25 °C, and time is not treated as a state. This stage of the optimization problem is solved using stochastic dynamic programming where the traveling speed and the queuing times at charging stations are considered stochastic, the stochastic aspect is explained more in detail in section 4.7. If, at any stage, the speed is too high then it will be lowered until the constraints of the problem are satisfied. The second stage of the optimization problem will optimize the battery temperature and fine-tune the SoC trajectory given the starting time, charging decisions, speed profile, and SoC from the upper level. To solve this problem an NLP will be formulated using the full optimization problem formulation described previously but excluding the charging decisions. This NLP is then solved using the FORCESPRO NLP solver. In contrast to the upper level, the lower level does not consider any uncertain parameters. A diagram of the hierarchical decomposition can be found in figure 4.2, where the inputs and outputs of each layer are shown.

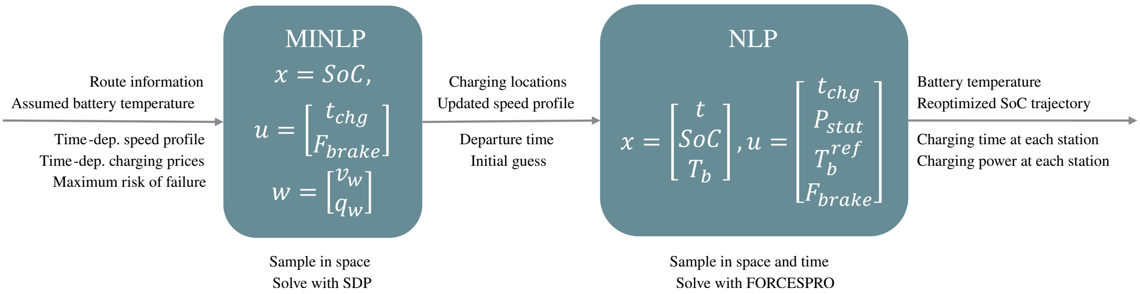

Figure 4.2: Hierarchical decomposition of the mission management optimization problem, showing the two layers and their states, inputs and outputs as well as the sampling structures and the solutions strategies of each layer.

4.6.1 Upper level - station selection

During the upper-level optimization, charging times are considered as control inputs at the stages where charging stations are placed. Only space sampling will be used to reduce the computational effort and the battery temperature will be approximated as constant $T_b(s) = 25\,^\circ\mathrm{C}$. In this stage, it is assumed that the truck always charges at maximum power, and thus P_{stat} is not considered as a control input in this level. Stochastic disturbances are also introduced, which represent uncertainties in the vehicle speed and the queuing times at charging stations. This gives the following states and inputs being used

$$\mathbf{x}_u(s) = \begin{bmatrix}\mathrm{soc}(s)\end{bmatrix}, \quad \mathbf{u}_u(s) = \begin{bmatrix} t_{chg}(s) \\ F_{brake}(s) \end{bmatrix}, \quad \mathbf{w}(s) = \begin{bmatrix} v_w(s) \\ q_w(s) \end{bmatrix}, \tag{4.41}$$

where $\mathbf{w}(s)$ represents stochastic disturbances and T_b^{ref} is not used as an input since the battery temperature is kept constant. The stochastic parameter v_w is a stochastic disturbance on the speed v which represents the the influence of the surrounding traffic on the speed of the truck, and q_w is the queuing time at the charging stations which is considered stochastic in this layer of the optimization. Both are explained more thoroughly in section 4.7. Since the truck is assumed to always travel at the traffic speed v, the time can be directly calculated from the charging times at each station sample and the traffic speed and thus does not need to be treated as a state. A fixed arrival time t_N is also introduced to optimize the departure time t_0 in this stage. The SoC dynamics are given as before

$$\frac{\mathrm{dsoc}(s)}{\mathrm{d}s} = -\frac{1}{v(s)} \frac{P_b(s) + \frac{R_{eq}(\mathrm{soc}(s),25)P_b^2(s)}{n_s^2 u_{oc}^2(\mathrm{soc}(s),23)}}{E_{cap}} = f(\cdot), \tag{4.42}$$

for all samples except for samples that contain a charging station. The battery power $P_b(s)$ is determined from the power balance equation

$$P_b(s) = P_{hc}(s) + P_{aux}(s) + P_{EM}(v(s, v_w(s)), F_T(s)), \tag{4.43}$$

which is adapted from the full optimization power balance equation (4.23). For samples s_i with charging stations, the update equation for the subsequent sample s_i^+ where potential charging is finished becomes

$$\mathrm{soc}(s_i^+) = \mathrm{soc}(s_i) - \zeta(s_i)\mathrm{soc}_{detour}(s_i) - t_{chg}(s_i) \int_0^1 \frac{P_b(\tau) + \frac{R_{eq}(\mathrm{soc}(\tau),25)P_b^2(\tau)}{n_s^2 u_{oc}^2(\mathrm{soc}(\tau),25)}}{E_{cap}} \mathrm{d}\tau, \tag{4.44}$$

where

$$P_b(\tau) = P_{hc}(\tau) + P_{aux}(\tau) - P_{stat}(s_i). \tag{4.45}$$

Solving the upper-level optimization step using SDP involves two steps, backward iteration to generate an optimal control policy for each stage and SoC level which is described in algorithm 1, and forward simulation to apply the control policy for a given initial conditions described in algorithm 2. To perform this optimization, the problem states and inputs need to be discretized. For this purpose, Euler forwards discretization is performed in both space and time using spatial discretization step sizes $L_s(s)$ and temporal steps $\Delta\tau$. The state soc is discretized in n_{soc} equal steps from 0.1 to 0.87 and the input t_{chg} is discretized in n_{tchg} steps from 0 to t_{chg}^{max}. Also define the stage cost function $l(\cdot)$such that

$$J(\cdot) = \sum_{s \in \mathcal{S}} l(s, \mathrm{soc}(s), \mathbf{u}(s), \mathbf{p}(s)) + J_N(\mathrm{soc}(s_N)) \tag{4.46}$$

To ensure that the problem remains feasible, a penalty is applied if at any stage and state pair $(s, \mathrm{soc}(s))$, the successor state $\mathrm{soc}(s^+)(s) = \mathrm{soc}(s) + f(\cdot)$ for the input $\mathbf{u}(s)$ does not fulfill the constraints $\mathbf{g}(\cdot)$ with a probability ε. This represents a maximum risk of failure for the mission and is formulated as

$$l(s, \mathrm{soc}(s), \mathbf{u}(s)) = \begin{cases} l_{drv}(s, \mathrm{soc}(s), \mathbf{u}(s)) + l_{chg}(s, \mathrm{soc}(s), \mathbf{u}(s)), & \Pr(\mathbf{g}(s^+) \geq 0) < \varepsilon \\ V_{max}, & \text{otherwise,} \end{cases} \tag{4.47}$$

where V_{max} is the maximum value of the cost function, $\mathbf{g}(s^+)$ represents the state and input constraints in section 4.3 and $l_{drv}(\cdot), l_{chg}(\cdot)$ are the stage costs for driving and charging which are adapted from section 4.4

$$\begin{aligned} l_{drv}(s, \mathrm{soc}(s), \mathbf{u}(s)) &= c_d L_s (F_T + F_{T,loss}) + c_t \Delta t + c_b L_s F_{brake}, \\ l_{chg}(s, \mathrm{soc}(s), \mathbf{u}(s)) &= \zeta \left(t_{chg} \int_0^1 \left(c_c(t) P_{stat}(\tau) + c_{cr} C_r(\tau)(27 - T_b) \right) \mathrm{d}\tau + c_t \Delta t + c_\zeta \right), \end{aligned} \tag{4.48}$$

where the spatial dependency s has been omitted for convenience. These cost functions, together with the terminal cost $J_N(\mathrm{soc}(s_N))$

$$J_N(\mathrm{soc}(s_N)) = \begin{cases} V_{max}, & \mathrm{soc(s)} \leq \mathrm{soc}_N^{min} \\ \frac{\mathrm{soc}(s_N) - \mathrm{soc}_N^{min}}{\mathrm{soc}^{max} - \mathrm{soc}^{min}} V_{max}, & \text{otherwise,} \end{cases} \tag{4.49}$$

where soc_N^{min} is the target final SoC, are used to find the optimal charging policy $\boldsymbol{\pi}(s, \mathrm{soc}(s))$. The policy specifies the optimal charging decisions $t^*_{chg}(s, \mathrm{soc})$ and braking decisions $F_{brake}(s, \mathrm{soc})$ such that the expected cost given the stochastic disturbances $\mathbf{w}$ is minimized. This policy is found in the backward step described in algorithm 1, where Bellman's principle of optimality [21] is utilized to iteratively construct the value function

$$V_{\boldsymbol{\pi}}(s, \mathrm{soc}(s)) = \min_{\mathbf{u}} \mathbb{E}_{\mathbf{w}} \left[\int_s^{s_N} l(\xi, \mathrm{soc}(\xi), \boldsymbol{\pi}(\xi, \mathrm{soc}(\xi)), \mathbf{p}(\xi)) \mathrm{d}\xi + J_N(\mathrm{soc}(s_N)) \right]. \tag{4.50}$$

The policy is then given as the optimal sequence of inputs $\mathbf{u}$ which is defined in the value function $V_{\boldsymbol{\pi}}(s, \mathrm{soc}(s))$, which means that

$$\boldsymbol{\pi}(s, \mathrm{soc}(s)) = \operatorname*{argmin}_{\mathbf{u}} \mathbb{E}_{\mathbf{w}} \left[\int_s^{s_N} l(\xi, \mathrm{soc}(\xi), \boldsymbol{\pi}(\xi, \mathrm{soc}(\xi)), \mathbf{p}(\xi)) \mathrm{d}\xi + J_N(\mathrm{soc}(s_N)) \right], \tag{4.51}$$

for each stage s and discretized SoC value $\mathrm{soc}(s)$. To apply the policy for SoC values in between the grid points in the SoC grid, piece-wise cubic interpolation is performed using MATLAB's `pchip` interpolation algorithm [57].

Algorithm 1 Backward recursion of the dynamic programming. Note that for brevity, no constraint validation is shown in the algorithm. At all stages the constraints are checked to be satisfied with probability $1-\varepsilon$, if not then the cost is set to V_{max}.

```
Define state and control domains $\mathrm{SOC} : n_{soc} \times 1,\ T_{chg} : n_{tchg} \times 1$.
Form 2D matrices $V,\ T,\ T^*_{chg} : n_{soc} \times N$.
Set terminal cost and time $V(:, s_N) = V_N,\ T(:, s_N) = t_N$.
Define disturbances $W_v,\ W_q : n_w \times N$ with probabilities $P_v,\ P_q : n_w \times N$.
for $s = s_{N-1}, ..., s_0$ do
    for $\mathrm{soc} \in \mathrm{SOC}$ do
        $i_{soc} \leftarrow \mathrm{index}(\mathrm{soc}, \mathrm{SOC})$        ▷ Index of SoC state in state vector
        $t^*_{chg} \leftarrow 0$
        $V_{temp} \leftarrow V_{max} : n_{soc} \times 1$.
        $T_{temp} \leftarrow -T_{max} : n_{soc} \times 1$.
        if $s \in \mathcal{S}_{chg}$ then        ▷ Stage contains a charging station
            $i_{stat} \leftarrow \mathrm{index}(s, \mathcal{S}_{chg})$        ▷ Index of charging station
            for $t_{chg} \in T_{chg}$ do
                $[\mathrm{soc}^+,\ \Delta t] \leftarrow \tilde{f}_{chg}(\mathrm{soc}, W_q(:, s), s)$
                        ▷ Interpolate over SOC to fill in any gaps
                $V_{step} \leftarrow \mathbb{E}_{W_q(:,s)}\left[l_{chg,i_{stat}}(\mathrm{soc}, W_q(:, s), s) + V(\mathrm{soc}^+, s+1)\right]$
                if $V_{step} < V_{temp}(i_{soc})$ then
                    $V_{temp}(i_{soc}) \leftarrow V_{step}$
                    $T_{temp}(i_{soc}) \leftarrow \mathbb{E}_{W_q(:,s)}\left[T(\mathrm{soc}^+, s+1) + \Delta t\right]$
                    $t^*_{chg} \leftarrow t_{chg}$
                end if
            end for
            $[\mathrm{soc}^+,\ \Delta t] \leftarrow \tilde{f}_{drv}(\mathrm{soc}, W_v(:, s), s)$
            $V_{step} \leftarrow \mathbb{E}_{W_v(:,s)}\left[l_{drv}(\mathrm{soc}, W_v(:, s), s) + V(\mathrm{soc}^+, s+1)\right]$
            if $V_{step} < V_{temp}(i_{soc})$ then
                $V_{temp}(i_{soc}) \leftarrow V_{step}$        ▷ Optimal to not charge
                $T_{temp}(i_{soc}) \leftarrow \mathbb{E}_{W_v(:,s)}\left[T(\mathrm{soc}^+, s+1) + \Delta t\right]$
                $t^*_{chg} \leftarrow 0$
            end if
        else        ▷ Stage contains no charging station
            $[\mathrm{soc}^+,\ \Delta t] \leftarrow \tilde{f}_{drv}(\mathrm{soc}, W_v(:, s), s)$
            $V_{step} \leftarrow \mathbb{E}_{W_v(:,s)}\left[l_{drv}(\mathrm{soc}, W_v(:, s), s) + V(\mathrm{soc}^+, s+1)\right]$
            if $V_{step} < V_{temp}(i_{soc})$ then
                $V_{temp}(i_{soc}) \leftarrow V_{step}$
                $T_{temp}(i_{soc}) \leftarrow \mathbb{E}_{W_v(:,s)}\left[T(\mathrm{soc}^+, s+1) + \Delta t\right]$
            end if
        end if
        $T^*_{chg}(i_{soc}, s) \leftarrow t^*_{chg}$
    end for
    $V(:, s) = V_{temp}$
    $T(:, s) = T_{temp}$
end for
```

Algorithm 2 Forward simulation of the dynamic programming. Again the constraint validation is not shown to keep the explanation short.

```
Define state and control domains SOC : $n_{soc} \times 1$, $T_{chg} : n_{tchg} \times 1$.
Form state and control vectors soc, $t$, $t_{chg} : n_{soc} \times 1$
Get quadratic matrices $V$, $T$, $T^*_{chg} : n_{soc} \times N$ from backwards part.
Set initial values $\mathrm{soc}(s_0) = \mathrm{soc}_0$, $t(s_0) = T(\mathrm{soc}_0, s_0)$
Define probability distributions of disturbances $W_v := \mathcal{N}(v_w : \boldsymbol{\mu}_v, \boldsymbol{\Sigma}_v)$,
$W_q := \mathrm{Pois}(q_w : \boldsymbol{\lambda}_q)$.    ▷ Vector-valued parameters signify the possibility of defining different probability modes for each stage.
for $s = s_1, ..., s_N$ do    ▷ Loop from second stage until $s_N = s_N$
    if $s \in \mathcal{S}_{chg}$ then
        $t_{chg}(s) = T^*_{chg}(\mathrm{soc}(s-1))$    ▷ Charging stage
        if $t_{chg}(s) > 0$ then
            Draw $q \sim W_q(s)$    ▷ Charging
            $[\mathrm{soc}(s),\ \Delta t] \leftarrow \tilde{f}_{chg}(\mathrm{soc}(s-1), q, s)$
        else
            Draw $v \sim W_v(s)$    ▷ Not charging
            $[\mathrm{soc}(s),\ \Delta t] \leftarrow \tilde{f}_{drv}(\mathrm{soc}(s-1), v, s)$
        end if
    else
        Draw $v \sim W_v(s)$    ▷ Driving stage
        $[\mathrm{soc}(s),\ \Delta t] \leftarrow \tilde{f}_{drv}(\mathrm{soc}(s-1), v, s)$
    end if
    $t(s) = t(s-1) + \Delta t$
end for
```

4.6.2 Lower level - battery management

Given the optimal charging times t^{i*}_{chg} from the upper level, the charging stops are

$$\zeta^*_i = \begin{cases} 1, & t^{i*}_{chg} > 0, \\ 0, & \text{otherwise.} \end{cases} \tag{4.52}$$

Given ζ^*_i, define the new charging set $\mathcal{S}^*_{chg} = \mathcal{S}_{chg} \cap \{s_i \in \mathcal{S}_{chg} \mid \zeta^*_i = 1, i \in \mathcal{I}\}$ and the new driving set $\mathcal{S}^*_{drv} = \mathcal{S}_{drv} \cup \{s_i \in \mathcal{S}_{chg} \mid \zeta^*_i = 0, i \in \mathcal{I}\}$. The lower level optimization problem, for departure time t^*_0 and charging indices $s_i \in \mathcal{S}^*_{chg}$, is then formulated as

$$\underset{\mathbf{u}_{drv}(s), \mathbf{u}^i_{chg}(\tau_i)}{\text{minimize}} \quad J_{drv}(\cdot) + J_{chg}(\cdot) \tag{4.53a}$$

$$\text{subject to}$$

$$\frac{\mathrm{d}\mathbf{x}_{drv}(s)}{\mathrm{d}s} = \mathbf{f}_{drv}(\mathbf{x}_{drv}(s), \mathbf{u}_{drv}(s), \mathbf{p}_{drv}(s)) \qquad s \in \mathcal{S}^*_{drv}, \tag{4.53b}$$

$$\frac{\mathrm{d}\mathbf{x}^i_{chg}(\tau_i)}{\mathrm{d}\tau_i} = \mathbf{f}_{chg}(\mathbf{x}^i_{chg}(\tau_i), \mathbf{u}^i_{chg}(\tau_i), \mathbf{p}^i_{chg}(\tau_i)) \qquad s \in s_i, \tag{4.53c}$$

$$0 \geq \mathbf{g}_{drv}(\mathbf{x}_{drv}(s), \mathbf{u}_{drv}(s), \mathbf{p}_{drv}(s)) \qquad s \in \mathcal{S}^*_{drv}, \tag{4.53d}$$

$$0 \geq \mathbf{g}_{chg}(\mathbf{x}^i_{chg}(\tau_i), \mathbf{u}^i_{chg}(\tau_i), \mathbf{p}^i_{chg}(\tau_i)) \quad s \in s_i, \tag{4.53e}$$

$$P_b^{drv}(s) = h_{drv}(\mathbf{x}_{drv}(s), \mathbf{u}_{drv}(s), \mathbf{p}_{drv}(s)) \quad s \in \mathcal{S}^*_{drv}, \tag{4.53f}$$

$$P_{b,i}^{chg}(\tau_i) = h_{chg}(\mathbf{x}^i_{chg}(\tau_i), \mathbf{u}^i_{chg}(\tau_i), \mathbf{p}^i_{chg}(\tau_i)) \quad s \in s_i, \tag{4.53g}$$

$$\mathbf{x}_{drv}(s) \in \mathcal{X}_{drv}, \quad \mathbf{u}_{drv}(s) \in \mathcal{U}_{drv} \quad s \in \mathcal{S}^*_{drv}, \tag{4.53h}$$

$$\mathbf{x}^i_{chg}(\tau_i) \in \mathcal{X}^i_{chg}, \quad \mathbf{u}^i_{chg}(\tau_i) \in \mathcal{U}^i_{chg} \quad s \in s_i, \tag{4.53i}$$

$$\mathbf{x}^i_{chg}(0) = \mathbf{x}_{drv}(s_i) - \zeta_i^* \mathbf{x}^i_{detour}, \tag{4.53j}$$

$$\mathbf{x}_{drv}(s_i^+) = \mathbf{x}^i_{chg}(1) - \zeta_i^* \mathbf{x}^i_{detour}, \tag{4.53k}$$

$$\mathbf{x}_{drv}(s_0) \in \mathcal{X}_0, \quad \mathbf{x}_{drv}(s_N) \in \mathcal{X}_N \tag{4.53l}$$

which is now solved as an NLP using FORCESPRO by ensuring that the truck stops at each station ($\zeta_i > 0 \ \forall i$), removing the integer decisions.

4.7 Stochastic parameters

As was previously mentioned in section 4.6, the parameters that are considered stochastic in the upper-level optimization problem are the vehicle speed and the charging station queuing times. Stochastic parameters are considered at this level of the optimization problem to robustly select charging stations, which is important considering that a simplified model is used in the mission management problem which might lead to an inaccurate prediction of the actual power consumption in the truck.

The vehicle speed is considered stochastic to model the effect of an uncertain traffic situation, since during heavy traffic the truck will not be able to travel at the specified speed limit. The traffic disturbance is modeled as a multiplicative Gaussian distribution with mean $\boldsymbol{\mu}_v$ and variance $\boldsymbol{\Sigma}_v$ which are defined as vectors of length N to allow for different distributions at each driving stage. This then gives the stochastic definition of the vehicle speed

$$v = v_{limit} v_w, \quad v_w \sim \mathcal{N}(v_w : \boldsymbol{\mu}_v(s), \boldsymbol{\Sigma}_v(s)), \ s \in \mathcal{S}_{drv}. \tag{4.54}$$

The uncertainty in the velocity also leads to an uncertain power demand, since the vehicle power consumption in most cases is dominated by the term vF_T. The queuing times at each charging station are modeled as Poisson distributions with rates $\boldsymbol{\lambda}_q$. The modeling of the queuing processes is based on the article [58], where the problem of stochastic EV charging at stations is studied more in-depth. The act of queuing at each station is included in the transition equality $\mathbf{x}_{drv}(s_i) = \mathbf{x}^i_{chg}(0) - \zeta_i \mathbf{x}_{detour}$, where it can be approximated as charging for the time $q_w \sim \text{Pois}(q_w : \boldsymbol{\lambda}_q(s))$ with charging power 0. The stochastic queuing times represent an uncertain occupation status for each charging station.

4.8 Discretization

Both the SDP and the FORCESPRO NLP solver perform numerical integration to approximate solutions to the optimal control problem described in the previous sections. This requires the problem to be discretized with sufficiently small discretization steps. Denote these $h_k = t_{k+1} - t_k$, which are allowed to be non-equidistant during the driving stages. The numerical integration method which is used in this thesis is the first-order explicit Runge-Kutta method, otherwise known as the explicit Euler method. This method was selected for its simplicity and ease of implementation. Using the explicit Euler method the state update for a state x becomes

$$x(t_{k+1}) = x(t_k) + h_k f(x(t_k), u(t_k), t_k), \tag{4.55}$$

where $f(x(t_k), u(t_k), t_k)$ represents the continuous time dynamics of the state x. The drawback of using this method is that it requires small step sizes h_k to achieve sufficiently high accuracies. This is because the local integration error $\|\hat{x}(t_{k+1}) - x(t_{k+1})\|$ is of order $\mathcal{O}(h_k^2)$, which gives a global integration error $\|\hat{x}(T) - X(T)\|$ of order $\mathcal{O}(h)$ for equidistant time-steps.

5

Simulation setup

From the research questions presented in section 1.4, reiterated here for convenience

1. How can a hierarchical control structure be defined to solve the mixed integer formulation of the problem efficiently?
2. How can the station selection be made robustly to account for uncertainties in power demand?
3. How can time-varying parameters like traffic speed and charging prices at charging stations be incorporated into the problem formulation?
4. How can battery health decay be minimized at a mission management level?

the following specifications are made to formulate test cases. To evaluate the first research question the total cost is mainly used as a metric and the solution suggested by the full hierarchical solver is compared against a controller using a sigmoid smoothening technique as in Bragde and Sundberg's thesis [36], and against a simple controller which emulates driver behavior. This leads to the following two questions

a. How does the total cost of the solution from the hierarchical solver compare against the solution using the sigmoid approximation?
b. How does the total cost of the solution from the hierarchical solver compare against a driver that is not using mission management?

The test setup for evaluating the two questions above is found in section 5.1, this test is made using time-varying parameters for charging prices and traffic situations and thus also answers research question 3. For the second research question, the robustness is evaluated by simulating a plant using the same dynamics as is described in chapter 2, but with a stochastic disturbance added to the battery power demand P_b. This simulation is made using the optimal charging decisions and thermal power that is output from the hierarchical solution to evaluate how well the solution can handle model mismatches, and the test setup for this case is found in section 5.2. The station selection output from the upper layer of the hierarchical solver is also evaluated in section 5.3 for different initial SoC values. The evaluation of the fourth research question is described in section 5.4, where different additions to the cost function are discussed and how they affect the overall battery throughput, which is used as a metric to measure the degradation.

5.1 Full solver evaluation

To evaluate the efficiency of the hierarchical mission planner, it is evaluated against a sigmoid approximation solution as in [36] and a heuristic algorithm which is designed to emulate typical driver behavior which is described in algorithm 3. The evaluation is performed on the following two routes

- Gothenburg-Rødby (GR): A medium-length route of length 461.4 km with flat topography and a cool ambient temperature with mean 12.9 °C. A topographical map of the route is shown in figure 5.2a.
- Genoa-Karlsruhe (GK): A long route of length 664 km with hilly topography and a higher ambient temperature with mean 30.6 °C. A topographical map of the route is shown in figure 5.2b.

These routes are described in more detail in sections 5.1.1 and 5.1.2. Both routes are simulated for time-dependent charging prices and speed profiles, where the speed profiles are described in sections 5.1.1 and 5.1.2. Each route is simulated for 3 cases of stochastic disturbances, with the probability distributions defined in section 5.1.3

a. High consumption (always $+1\sigma$ disturbance on velocity).
b. Low consumption (always -1σ disturbance on velocity).
c. Average consumption (always average disturbance).

Both routes are discretized into 500 stages using non-uniform sampling to preserve the altitude profile of the trip. All simulations start with the initial battery temperature $T_b(s_0) = 23\,^\circ\mathrm{C}$ and the initial SoC $\mathrm{soc}(s_0) = 85\,\%$, and the final minimum SoC level is set to $\mathrm{soc}(s_N) \geq 30\,\%$. All charging stations have the same base charging price of 8 SEK/kWh, but the price is allowed to vary depending on the time of day. This is done by introducing the time-dependent charging price multiplier, which is shown in figure 5.1, where the charging price is 20% higher during peak power demand and 20% lower during off-peak demand. For all simulations, the maximum risk of failure in the SDP is set to $\varepsilon = 0.05$.

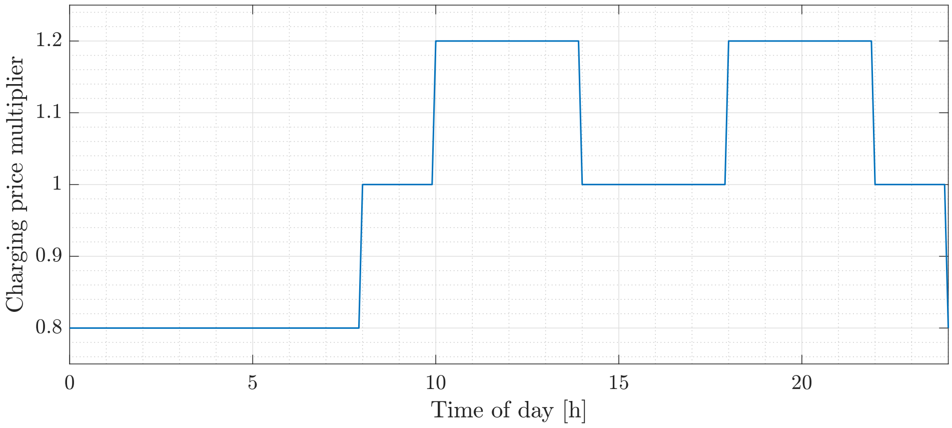

Figure 5.1: Charging price multiplier depending on the time of day. The charging price is 20% higher during peak power demand and 20% lower during off-peak demand.

Algorithm 3 Heuristic solution to the mission management problem, which is used to emulate driver behavior. It simulates the truck driving dynamics until the SoC is below 10%, and then backtracks until the last passed charging station. Once a station is found, it charges until full on that station and then continues driving, repeating the same charging decision process until the end of the trip.

```
Form 2D matrices $X : N \times n_x,\ U : N \times n_u$        ▷ Matrices of states and inputs.
$X(1,:) = \mathbf{x}_0$        ▷ Initial states.
$U(:,3) = 25$        ▷ Fix $T_b^{ref}$ at 25 °C.
$J = 0$        ▷ Initialize mission cost.
$k \leftarrow 1$        ▷ Initialize stage tracker.
$\zeta \leftarrow 0$        ▷ Initialize charging decision variable.
while $k < N$ do        ▷ Loop until end of trip.
    $\mathbf{x}_k \leftarrow X(k,:)$
    $\mathbf{u}_k \leftarrow U(k,:)$
    if $\zeta$ then
        $P_{stat} = \min(P_{stat,k}^{max}, P_{chg}^{max})$        ▷ Charge at maximum power.
        $t_{chg} = \max\left(\frac{\mathrm{soc}^{max} - \mathbf{x}_k(2)}{P_{stat}} E_{cap}, 0\right)$        ▷ Charge until full
        $\mathbf{u}_k(1:2) = [t_{chg}\ P_{stat}]$
    end if
    if $\mathbf{x}_k(2) < 0.1$ then        ▷ SoC is too low, backtrack to the last charging station.
        $\zeta = 1$
        $k = \mathcal{I}(\mathcal{I} < k)(\mathrm{end})$        ▷ Index of last charging station which has been passed.
        Go to the beginning of the next loop.
    end if
    if $\neg\zeta$ then        ▷ Driving
        $\mathbf{x}_{k+1} \leftarrow \mathbf{f}_{drv}(\mathbf{x}_k, \mathbf{u}_k, \mathbf{p}_k)$
        $J \leftarrow J + J_{drv}(\mathbf{x}_k, \mathbf{u}_k, \mathbf{p}_k)$
    else        ▷ Charging
        $\mathbf{x}_{k+1} \leftarrow \mathbf{f}_{chg}(\mathbf{x}_k, \mathbf{u}_k, \mathbf{p}_k)$
        $J \leftarrow J + J_{chg}(\mathbf{x}_k, \mathbf{u}_k, \mathbf{p}_k)$
    end if
    $X(k+1,:) \leftarrow \mathbf{x}_{k+1}$
    $U(k,:) \leftarrow \mathbf{u}_k$
    $\zeta \leftarrow 0$        ▷ Reset decision variable.
    $k \leftarrow k + 1$        ▷ Increment stage number.
end while
```

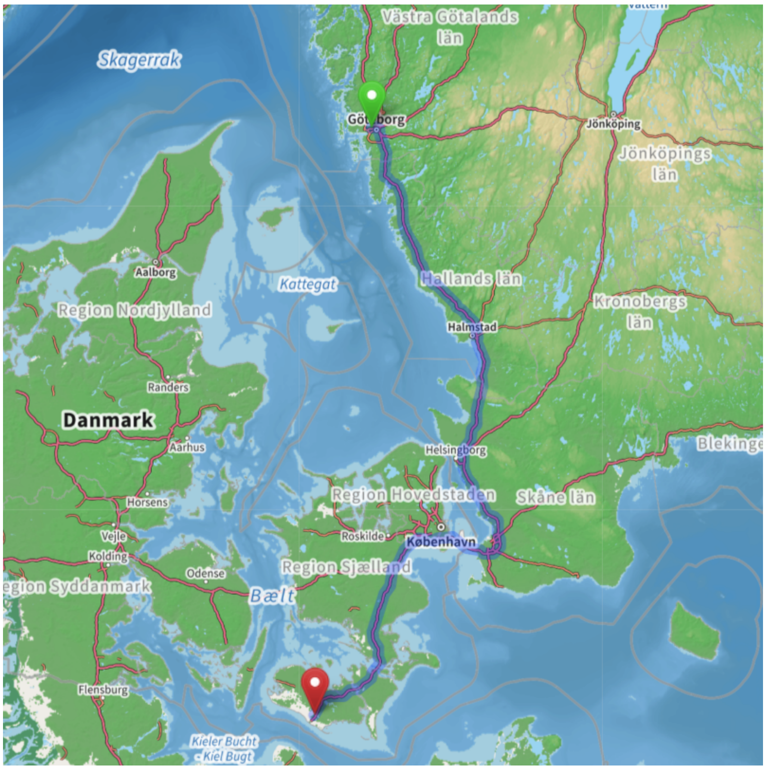

(a) Topographical relief map of the route Gothenburg-Rødby.

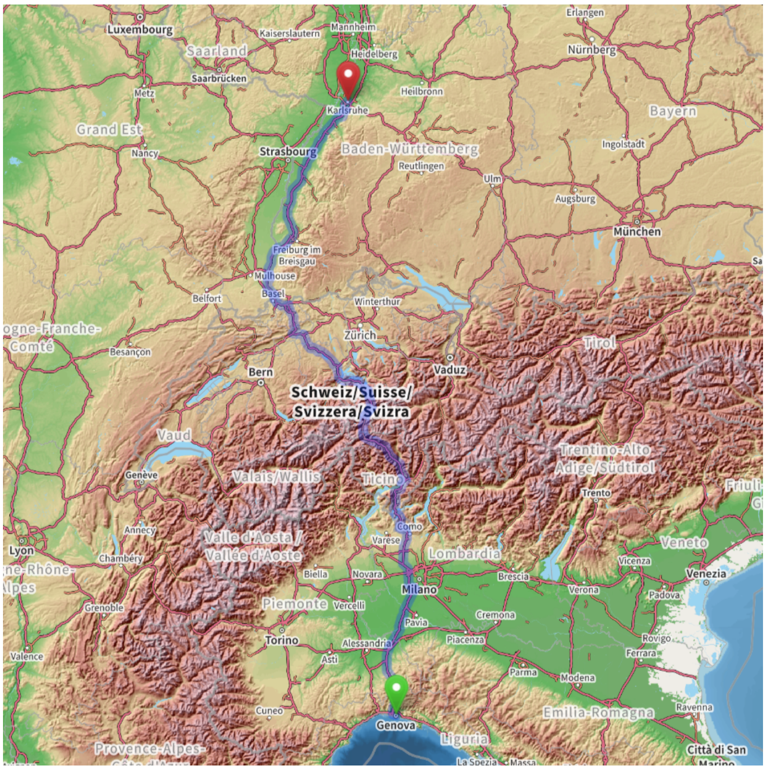

(b) Topographical relief map of the route Genoa-Karlsruhe.

Figure 5.2: Topographical relief maps of the routes which are studied in this thesis. Both maps are made available by OpenStreetMap contributors [59], retrieved from `https://www.openstreetmap.org/` on 2024-04-23. ODbL.

5.1.1 Gothenburg-Rødby

The altitude profile and speed limits of the GR route are shown in figure 5.3, together with the location of each charging station on the route. The parameters of the charging stations are found in table 5.1. The speed limits in figure 5.3 need to be pre-processed to ensure that the optimization problem remains feasible throughout the whole route since the truck is assumed to always travel at the traffic speed. This is because the road speed limits do not take into account the physical constraints of the truck, such as the maximum traction effort and the battery power bounds. This pre-processing is described in algorithm 4. For this route, the final time of day is set to $t_N = 17.00$ and the maximum trip time is $t_{max} = 9.33$ hours. Simulated congestion is also added between 270 km to 300 km from 12.00 to 14.00 for simulations with time-dependent traffic speeds.

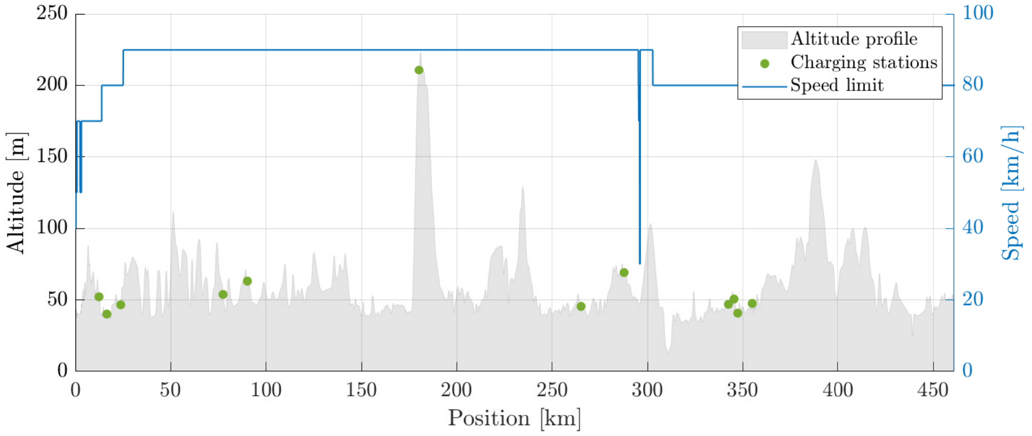

Figure 5.3: Altitude profile and speed limits of the Gothenburg-Rødby route. The locations of the charging stations listed in table 5.1 are shown as green dots in the plot.

Table 5.1: Station positions and parameters for the route Gothenburg-Rødby.

Station	Position [km]	Power capacity [kW]	Detour distance [m]	Mean queue time [minutes]
1	12.37	200	558	10
2	16.50	150	878	10
3	23.76	50	442	40
4	77.43	350.4	915	30
5	90.20	50	575	40
6	180.2	75	792	25
7	265.2	200	618	10
8	287.7	50	940	40
9	342.4	350.4	834	30
10	345.4	50	435	40
11	347.3	150	607	10
12	354.9	300	647	25

Algorithm 4 Speed limit pre-processing. Recalculates the speed limits to satisfy the constraints of the truck model. Assumes that the battery temperature is 25 °C and the SoC is 0.5 for all stages.

```
Initialize $v = v_{limit} : N \times 1$                    ▷ Start from the road speed limits.
for $s = s_0, ..., s_N$ do                                 ▷ Update the speed limit for each stage.
    $v(s) \leftarrow v(s)/3.6$                                              ▷ Convert to m/s.
    $F_T \leftarrow m_e\dot{v}(s) + F_{grad}(s) + F_{rr}(s) + F_{air}(s)$     ▷ Longitudinal dynamics
    $P_b \leftarrow P_{aux}(s) + v(s)(F_T + F_{T,loss}(F_T) + P_{hc}(s)$      ▷ Power balance equation
    if $P_b > P_{b,dch}^{max}$ then
        $v \leftarrow \frac{P_{b,dch}^{max} - P_{aux}(s) - P_{hc}(s)}{F_T + F_{T,loss}(F_T)}$
        $F_T \leftarrow m_e\dot{v}(s) + F_{grad}(s) + F_{rr}(s) + F_{air}(s)$
    end if
    if $F_T > F_T^{max}(v(s))$ then
        while $F_T > F_T^{max}(v)$ do
            $v(s) \leftarrow v(s) - 1$          ▷ Iteratively lower $v(s)$ until constraint satisfied.
            $F_T \leftarrow m_e\dot{v}(s) + F_{grad}(s) + F_{rr}(s) + F_{air}(s)$
        end while
    end if
    $v(s) \leftarrow 3.6v(s)$                                      ▷ Convert back to km/h
    $v \leftarrow \min(v, 80\,\text{km/h})$                        ▷ Enforce maximum truck speed.
end for
```

Applying the pre-processing algorithm on the road speed limits in figure 5.3 results in the updated speed limits shown in figure 5.4.

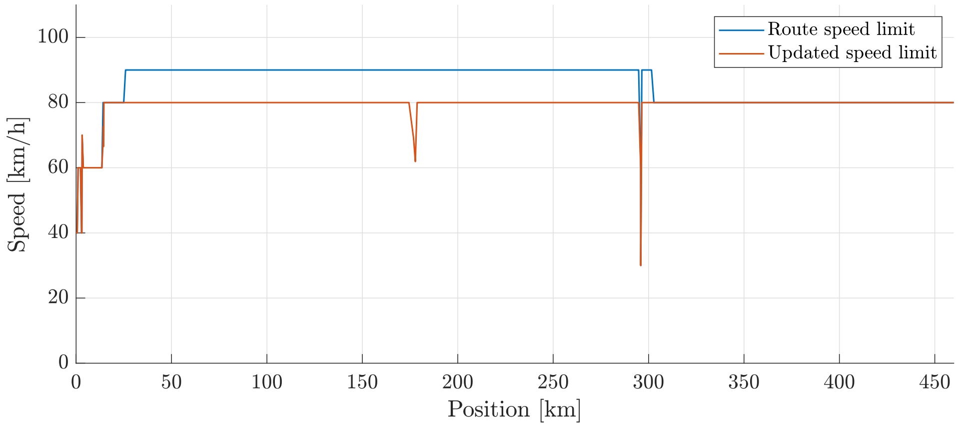

Figure 5.4: Updated speed limits compared to original speed limits for the Gothenburg-Rødby route.

5.1.2 Genoa-Karlsruhe

The altitude profile and speed limits of the GK route are shown in figure 5.5, together with the location of each charging station on the route. For the GK route, the arrival time of day is set to $t_N = 18.00$ and the maximum trip time is $t_{max} = 13.33$ hours. If time-dependent traffic speeds are enabled then a congestion is present between 250 km to 270 km from 9.30 to 11.00.

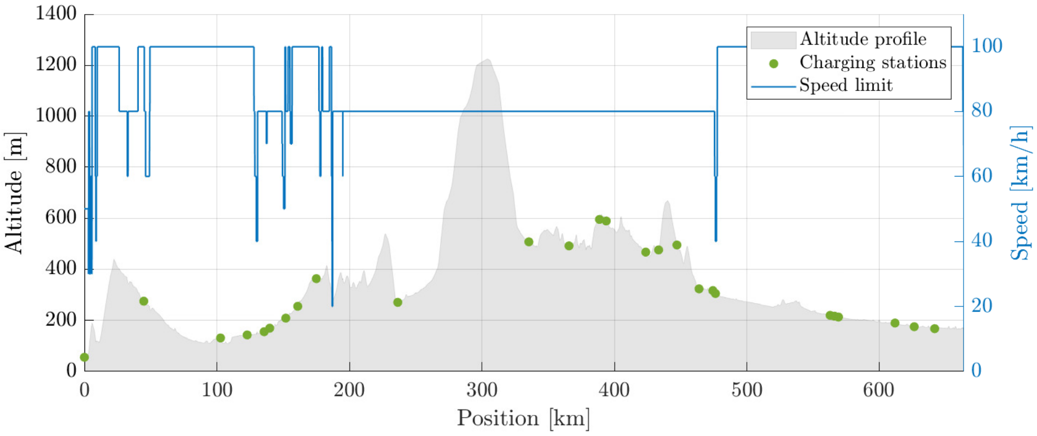

Figure 5.5: Altitude profile and speed limits of the Genoa-Karlsruhe route. The locations of the charging stations listed in table 5.2 are shown as green dots in the plot.

Applying algorithm 4 on the speed limits in figure 5.5 results in the updated speed limits in figure 5.6.

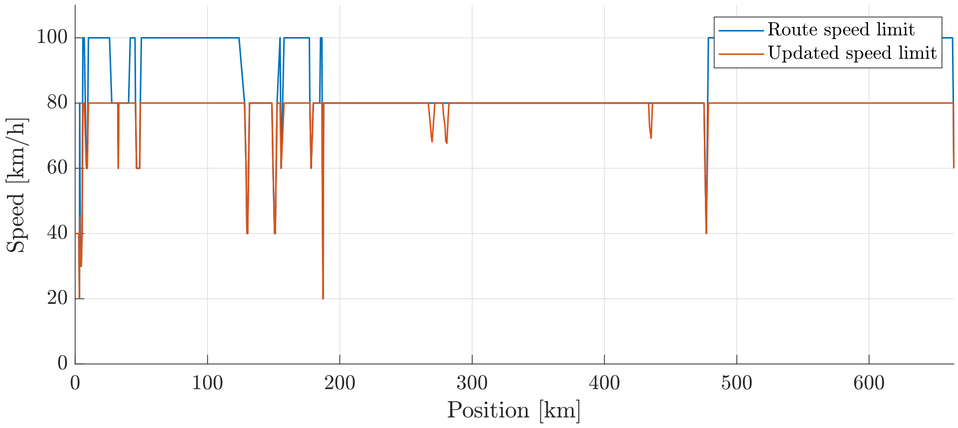

Figure 5.6: Updated speed limits compared to original speed limits for the Genoa-Karlsruhe route.

The parameters of the charging stations along the route are found in table 5.2.

Table 5.2: Station positions and parameters for the route Genoa-Karlsruhe.

Station	Position [km]	Power capacity [kW]	Detour distance [m]	Mean queue time [minutes]
1	0.01	60	1011	25
2	44.82	50	1057	35
3	102.7	60	1042	25
4	122.9	350.4	1242	30
5	135.6	300	1642	25
6	139.9	150	1881	10
7	152.0	50	1132	35
8	161.0	110	1392	15
9	175.0	50	1667	35
10	236.5	350.4	1685	30
11	335.4	350.4	642	30
12	365.7	160	814	10
13	388.7	350.4	455	30
14	393.8	100	383	10
15	423.6	300	1491	25
16	433.3	100	1867	10
17	447.1	100	197	10
18	463.8	50	1828	35
19	474.3	64	1191	25
20	476.2	50	721	35
21	562.7	300	1149	25
22	566.0	300	815	25
23	569.0	350.4	459	30
24	612.0	300	1121	25
25	626.5	150	550	10
26	641.9	300	1586	25

5.1.3 Stochastic disturbances

For each stage in the problem, the stochastic speed disturbance is sampled from the Gaussian distribution

$$v_w \sim \mathcal{N}(1, 0.05), \tag{5.1}$$

meaning that the same speed distribution is used for each sample. The stochastic queuing times are sampled from the Poisson distributions

$$q_w \sim \mathrm{Pois}(\lambda_q), \tag{5.2}$$

with the parameter λ_q given as the mean queue times in tables 5.1 and 5.2.

5.2 Model mismatch evaluation

To evaluate how well the optimization can handle model mismatches, the optimal inputs given from the mission management optimization will be evaluated on a plant model with an introduced model mismatch. Note that the mismatch is introduced after solving the optimization problem, to analyze how much the simulation using the perturbed plant deviates from the FORCESPRO output. This evaluation is done on both the GR and GK route with no time-dependent parameters, and the solution given by the full hierarchical solver is compared to the solution which is found using sigmoid smoothening instead. The model mismatch is represented by introducing a stochastic disturbance on the battery power demand P_b and the active rate flow Q_{act} at each space sample in the following way

$$\hat{P}_b = wP_b, \quad \hat{Q}_{act} = wQ_{act}, \quad w \sim \mathcal{N}(1.05, 0.2^2), \tag{5.3}$$

where $\hat{P}_b$ is the perturbed battery power and $\hat{Q}_{act}$ is the perturbed active heat flow. These perturbed values are then used in the modified plant by replacing P_b in the SoC dynamics (2.20) and Q_{act} in the thermal dynamics (2.33). 100 trials are run for each route and the root mean squared error (RMSE) of each state x and perturbed state $\hat{x}$, given by

$$\text{RMSE} = \sqrt{\frac{1}{N}\sum_{k=1}^{N}(x(k) - \hat{x}(k))^2}, \tag{5.4}$$

is used as a metric to measure the total error which is introduced by the stochastic disturbance w. The stochastic disturbances are generated using MATLAB's pseudorandom number generators with the fixed seed `rng(2)`.

5.3 Station selection evaluation

The upper layer of the solver is also evaluated separately from the full solver to study the robustness of the station selection using the SDP. This is done on the GR route with time-dependent charging prices, but using a fixed speed profile. For this evaluation, 10 trials are run for the initial SoC levels $\text{soc}(s_0) \in [85, 70, 55, 40]$ %, however, the final SoC constraint is still kept at $\text{soc}(s_N) \geq 30\,\%$ and the mean and 95% confidence interval (CI) of the resulting SoC trajectory is analyzed using the calculated value function, charging time policy and departure time policy.

5.4 Battery health evaluation

Aside from constraints on battery SoC and temperature, battery health is also considered as part of the cost function. This is included as part of the charging cost function in equation (4.39), where the term $c_{cr}C_{r,i}(27 - T_{b,i})^2$ is a penalty on both the C-rate during charging and low battery temperatures. The effect of this cost term is evaluated by analyzing the battery throughput H and average C-rate during charging, for simulations that include the C-rate term and for simulations where it is not included in the cost function. Simulations are performed on both the GR and GK routes with time-dependent parameters, and using only mean disturbances in the station selection layer.

6

Simulation results

In the following chapter, the results of the simulation setups described in chapter 5 are demonstrated. Section 6.1 outlines the results of simulations performed with the full hierarchical mission manager and compares them with solutions using the sigmoid approximation and the heuristics algorithm. In section 6.2 the results of an evaluation of the station selection layer are presented. In section 6.3 a model error evaluation is performed, by comparing the simulation output from the full hierarchical solution to a simulation using the optimal model inputs on a plant with an introduced stochastic disturbance on the energy consumption and finally in section 6.4 the battery health evaluation is shown.

6.1 Evaluation of full hierarchical solver

This section outlines the results of the full hierarchical mission management solver, for the GR route in section 6.1.1 and for the GK route in section 6.1.2. The routes are simulated for the disturbance cases described in section 5.1.

6.1.1 Gothenburg-Rødby

This section describes the results of simulating the full hierarchical mission manager on the GR route described in section 5.1.1. The driving cycle is a medium-length route, requiring only one charging stop, and it is based on real-world measurements. A summary of the simulation results on the GR route is shown in table 6.1. The cost, energy consumption, and charged energy metrics are normalized and set to 1 for the highest values. The simulations are performed for the disturbance cases described in section 5.1 and compared to solutions using the sigmoid approximation and the heuristics algorithm. Also see appendix A for more plots from these simulations. For this route, the backward step in the SDP algorithm takes approximately 4 s.

Table 6.1: Summary of mission results for the GR route. Note that the computation time for the hierarchical solvers does not include the backward time of the SDP. The results of the hierarchical solver for the disturbance cases a-c described in section 5.1 are marked with bold.

Trip description	**Mean**	**High**	**Low**	Sigmoid	Heuristic
Trip time [h]	7.22	7.21	7.24	7.33	8.57
Arrival time [hh.mm]	17.01	17.00	17.04	17.00	18.14
Trip cost (Normalized)	0.731	0.752	0.694	0.785	1
Energy consumption (Normalized)	0.960	1	0.922	0.973	0.980
Selected stations	7	7	7	4, 7	12
Charged energy (Normalized)	0.345	0.362	0.278	0.480	1
Charging time [min]	51	53.2	41.2	54.2	80
Final SoC [%]	30.00	30.00	30.00	30.00	61.85
Average T_b [°C]	24.22	23.91	24.30	24.30	24.22
Maximum T_b [°C]	27.21	25.92	25.75	28.00	47.49
Computation time [s]	16.42	17.11	19.19	16.08	7.11

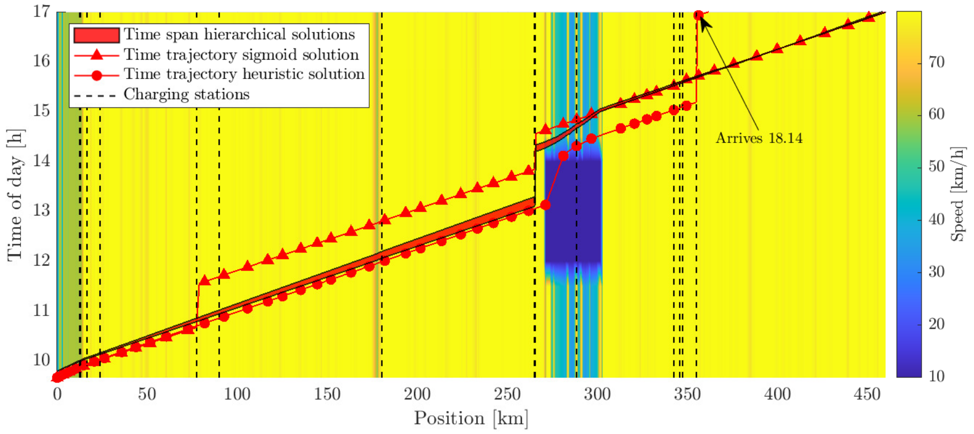

Figure 6.1: Plot of the time-varying speed limit for the GR route with the different trip time trajectories for disturbance cases a-c described in section 5.1 represented by the red area plot.

6.1.2 Genoa-Karlsruhe

This section outlines the results of simulating the full hierarchical mission manager on the GK route described in section 5.1.2. The GK route is long-range with large hills and is considered a challenging route for drivers, requiring two charging stops. Like the GR route, it is also based on real-world measurements. The results of the simulations are summarized in table 6.1, where again the cost, energy consumption, and charged energy metrics are normalized and set to 1 for the highest values. Simulations are also shown for the three disturbance cases described in section 5.1 and compared to solutions using the sigmoid approximation and the heuristics algorithm. In figure 6.2 the time-dependent speed profile is plotted against the trip time of the different solutions. Also see appendix B for more plots from these simulations. For the GK route, the backward step in the SDP algorithm takes approximately 8.2 s.

Table 6.2: Summary of mission results for the GK route. Note that the computation time for the hierarchical solvers does not include the backward time of the SDP. The results of the hierarchical solver for the disturbance cases a-c described in section 5.1 are marked with bold.

Trip description	**Mean**	**High**	**Low**	Sigmoid	Heuristic
Trip time [h]	11.58	11.58	11.58	12	11.76
Arrival time [hh.mm]	18.00	18.00	18.00	18.00	18.05
Trip cost (Normalized)	0.831	0.842	0.787	0.884	1
Energy consumption (Normalized)	0.967	1	0.923	0.978	0.980
Selected stations	10, 22	10, 22	10, 22	10, 13, 23	10, 23
Charged energy (Normalized)	0.556	0.548	0.487	0.664	1
Charging time [min]	91.6	88.9	69.9	120.5	119.7
Final SoC [%]	30.03	30.01	30.00	30.00	60.31
Average T_b [°C]	24.65	25.04	24.67	24.63	25.15
Maximum T_b [°C]	27.97	27.99	28.00	27.65	48.31
Computation time [s]	16.90	16.93	18.19	16.3	8.36

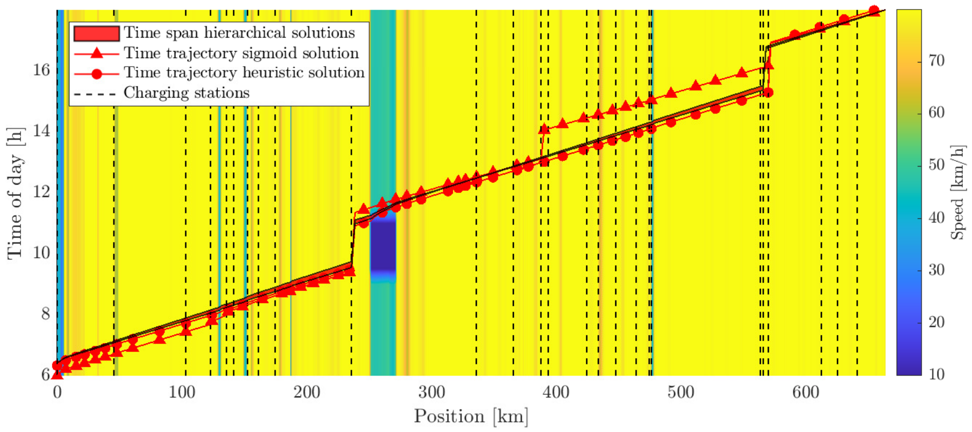

Figure 6.2: Plot of the time-varying speed limit for the GK route with the different trip time trajectories for disturbance cases a-c described in section 5.1 represented by the red area plot.

6.2 Evaluation of station selection layer

In this section, the upper layer of the hierarchical mission management solver is evaluated. The evaluation method is described in section 5.3, and is performed on the GR route using only time-dependent charging prices. In figure 6.3 the SoC and speed distribution are shown for initial SoC 85% and 70%, and in figure 6.4 the SoC and speed are shown for initial SoC 55% and 40%. Overall the uncertainty in speed remains similar over the different cases, except for in figure 6.3b, where a difference compared to the other plots is found at approximately 350 km. It can be noted that the uncertainty in SoC increases along the route, and after each charging instance (representing stochastic queuing).

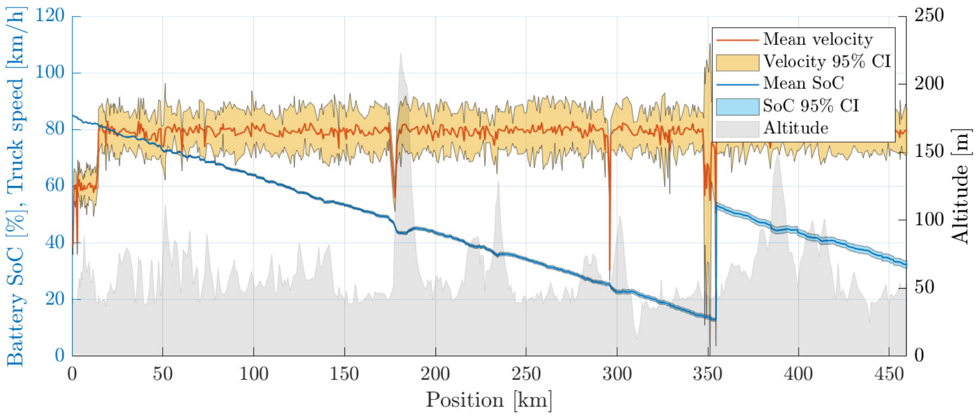

(a) SoC and speed trajectories for the initial SoC of 85%. In this case station 12 in table 5.1 is optimal to charge at.

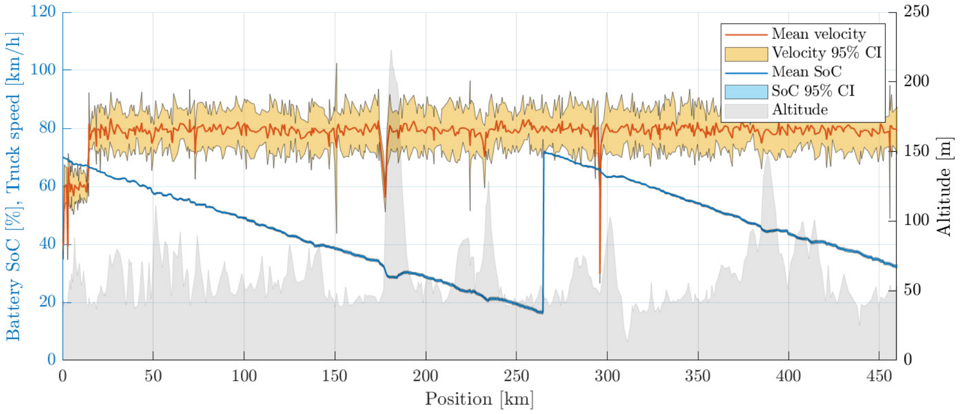

(b) SoC and speed trajectories for the initial SoC of 70%. In this case station 7 in table 5.1 is optimal to charge at.

Figure 6.3: Speed and SoC trajectory outputs from the upper layer for the GR route with time-dependent charging prices and **(a)** $\mathrm{soc}(0) = 0.85$, **(b)** $\mathrm{soc}(0) = 0.7$. Each case is simulated 10 times and the means and 95% CIs of the trajectories are plotted.

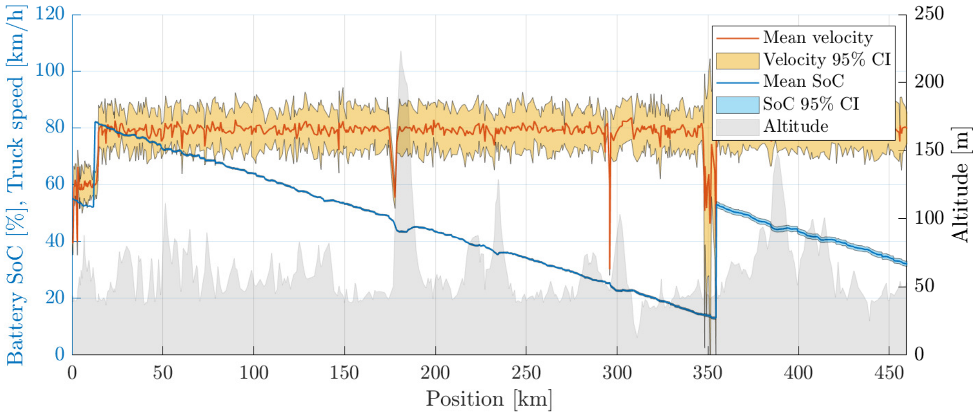

(a) SoC and speed trajectories for the initial SoC of 55%. In this case stations 1 and 12 in table 5.1 are optimal to charge at.

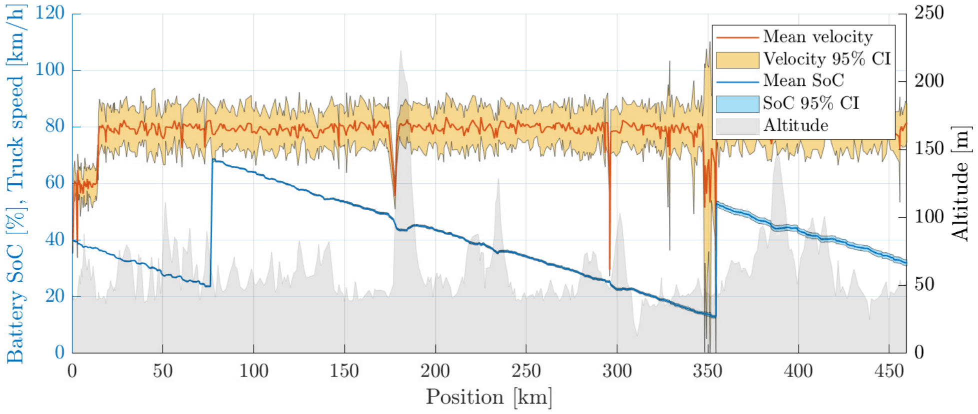

(b) SoC and speed trajectories for the initial SoC of 40%. In this case stations 4 and 12 in table 5.1 are optimal to charge at.

Figure 6.4: Speed and SoC trajectory outputs from the upper layer for the GR route with time-dependent charging prices and **(a)** $\mathrm{soc}(0) = 0.55$, **(b)** $\mathrm{soc}(0) = 0.4$. Each case is simulated 10 times and the means and 95% CIs of the trajectories are plotted.

In table 6.3 a summary of the results from the different simulations is shown. In the table, the objective value is shown as normalized such that the highest mean cost is set to 1. It can be seen that the trip time and cost increase for lower initial battery SoC, which also leads to earlier starting times for lower SoC values as well. In comparison to the results presented in section 6.1.1, it can also be noted that the friction brake usage is significantly higher and that the suggested charging times are slightly shorter. Further, in figure 6.5 the value function for the upper layer optimization problem is presented. The value function represents the cost to go from each position and SoC until the end of the trip, and the resulting SoC trajectories that minimize the value function for the initial SoC values 85%, 70%, 55%, and 40%. The charging time optimal policy which results in the value function is also plotted in figure 6.6, again together with SoC trajectories for the same initial SoC values.

Table 6.3: Comparison of mission results from the station selection layer for different initial SoC values. All uncertainties are represented by the 95% CI of the metrics, and the objective function values are normalized such that the largest mean cost is set to 1. The $F_b L_s$ metric represents total energy losses from friction brake usage.

Initial SoC [%]	85	70	55	40
Final SoC [%]	32 ± 1	32 ± 1	32 ± 1	32 ± 1
Optimal t_0 [hh.mm]	09.58	09.16	08.58	08.37
Simulated t_N [hh.mm]	17.00 ± 00.11	16.47 ± 00.06	17.07 ± 00.13	17.05 ± 00.22
Trip time [h]	7.10 ± 0.18	7.51 ± 0.1	8.14 ± 0.21	8.46 ± 0.37
Selected stations	12	7	1, 12	4, 12
Charging time [min]	42.4 ± 0.35	85.6 ± 0.84	88.1 ± 0.34	88.39 ± 0.38
Queuing time [min]	26.8 ± 12.1	11.4 ± 4.34	43.1 ± 10.8	62.77 ± 21.47
Total $F_b L_s$ [kWh]	3.32 ± 1.33	3.28 ± 1.97	2.56 ± 0.75	2.48 ± 1.58
Objective function [%]	67.29 ± 0.37	70.48 ± 0.61	97.95 ± 0.45	100 ± 0.75

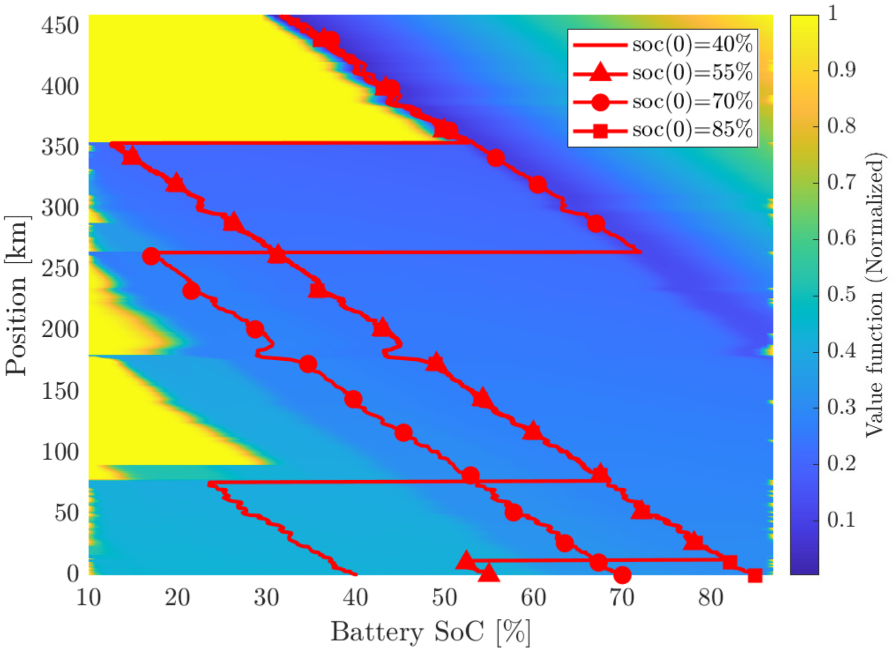

Figure 6.5: Surface plot of the value function in the station selection layer with SoC trajectories for initial SoC levels 40%, 55%, 70%, and 85%.

In figure 6.7 time mapping resulting from applying the optimal policy in figure 6.6 and the arrival time of day 17:00 is shown. This map shows the time of day for each feasible SoC and position along the trip, with infeasible regions shown as transparent. It is from this time mapping that the optimal departure times are found for each initial SoC value, and the departure time policy is plotted separately in figure 6.8. In both these plots the SoC trajectories for initial values 85%, 70%, 55%, and 40% are marked. It can be noted that the departure time follows a mostly linear relation, except for a bump near 60%.

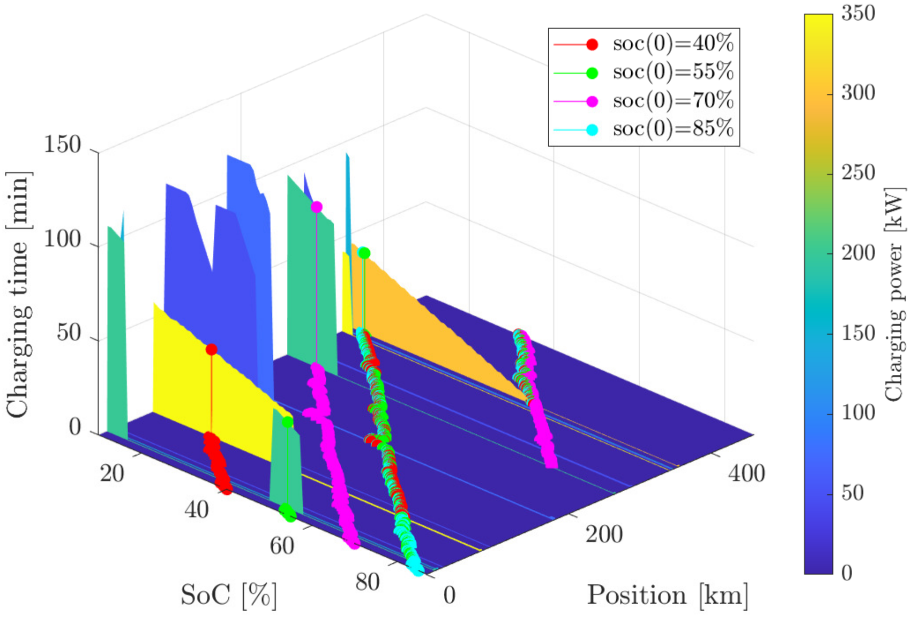

Figure 6.6: Illustration of the charging time policy in the station selection layer with SoC trajectories for initial SoC levels 40%, 55%, 70%, and 85%. The color of the graph represents the charging power capacities of the stations in table 5.1.

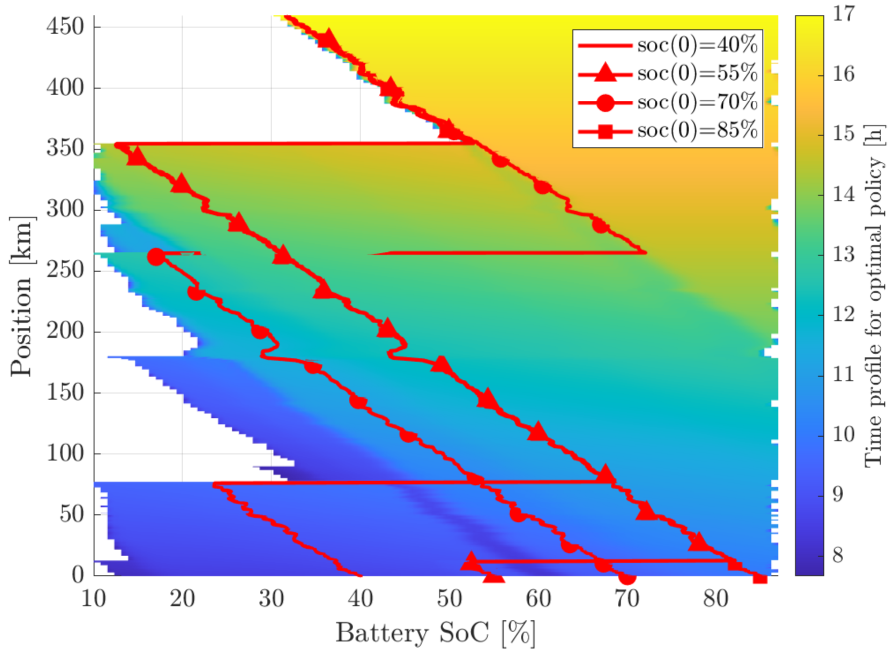

Figure 6.7: Plot of the time mapping resulting from using the policy in 6.6 and the final time $t_N = 17.00$ with plots of SoC trajectories for initial SoC levels 40%, 55%, 70% and 85%. The transparent regions of the plot represent regions of infeasibility.

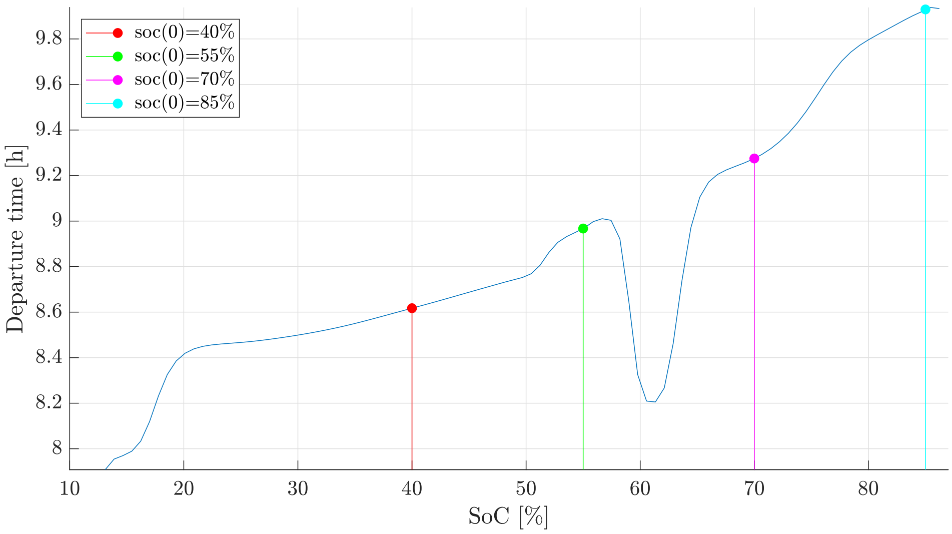

Figure 6.8: The departure time using the optimal policy shown in figure 6.6 with initial time shown for SoC levels 40%, 55%, 70% and 85%.

6.3 Model mismatch evaluation

Running the simulations with the perturbed plant model on the GR and GK route with no time-dependent parameters results in the RMSE errors of the SoC and battery temperatures in table 6.4, and the state trajectories in figures 6.9a and 6.9b. In both routes the error remains bounded and for most of the trips within the state bounds $\mathrm{soc}(s) \in [0.1, 0.87]$ and $T_b(s) \in [22, 28]$. In general, the temperature error becomes larger during periods of high power flow, such as during charging or steep road gradients, and the SoC error grows over time while the temperature error fluctuates depending on the power demand, shrinking during low power flow and increasing sharply during high power flow. This leads to the comparatively larger SoC error in the GK route, which is about 200 km longer than the GR route.

Table 6.4: Comparison of the RMSE of the SoC and battery temperature for the solutions based on the full hierarchical solver and the sigmoid approximation, with absolute errors plotted in figures 6.9a and 6.9b.

Route & Solver	GR Hierarchical	GR Sigmoid	GK Hierarchical	GK Sigmoid
RMSE SoC [%]	1.53	4.15	4.32	3.94
RMSE T_b [°C]	0.09	0.16	0.38	0.45

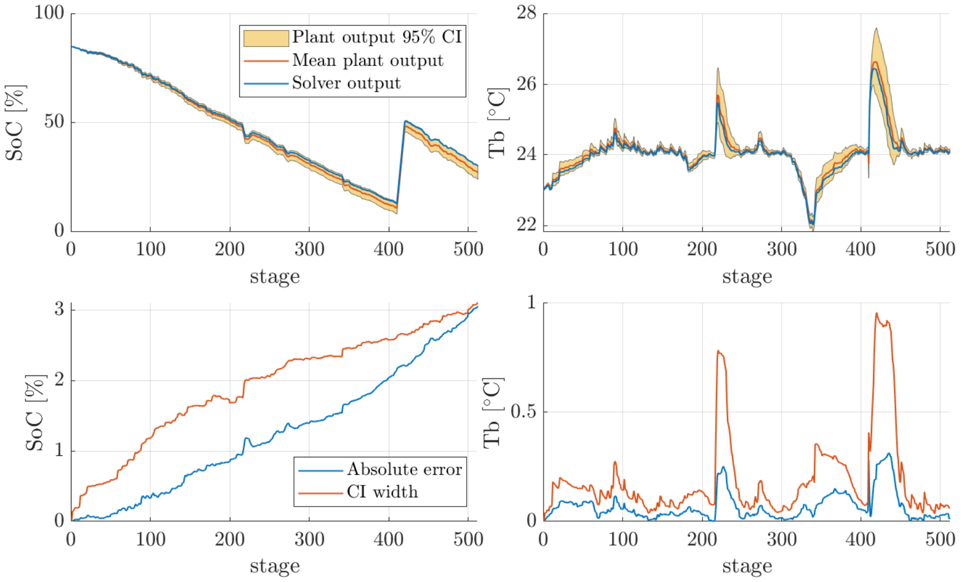

(a) Simulation using an perturbed plant model for the GR route using outputs from the hierarchical solver.

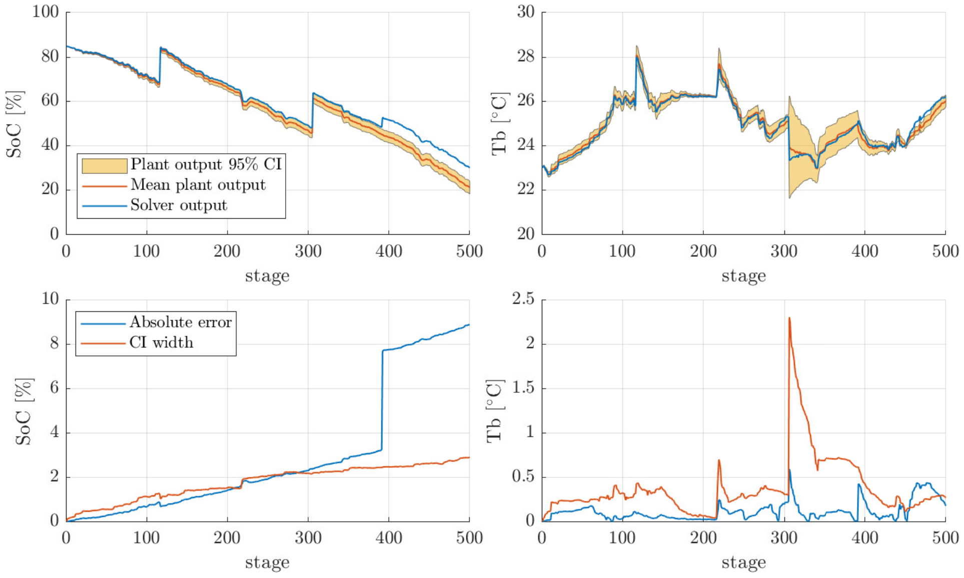

(b) Simulation using an perturbed plant model for the GR route using outputs from the sigmoid solver.

Figure 6.9: Plot SoC and battery temperature mean and 95% CI from the 100 simulations on the GR route including the model mismatch described in section 5.2, plotted against the SoC and temperature trajectories given control inputs from the FORCESPRO solver output. The absolute error plots represent the absolute distance between the mean state trajectory and the simulation output in each stage, and the size of the 95% CI is plotted in the same graphs. The hierarchical solution was used in **(a)** and the sigmoid approximation was used in **(b)**.

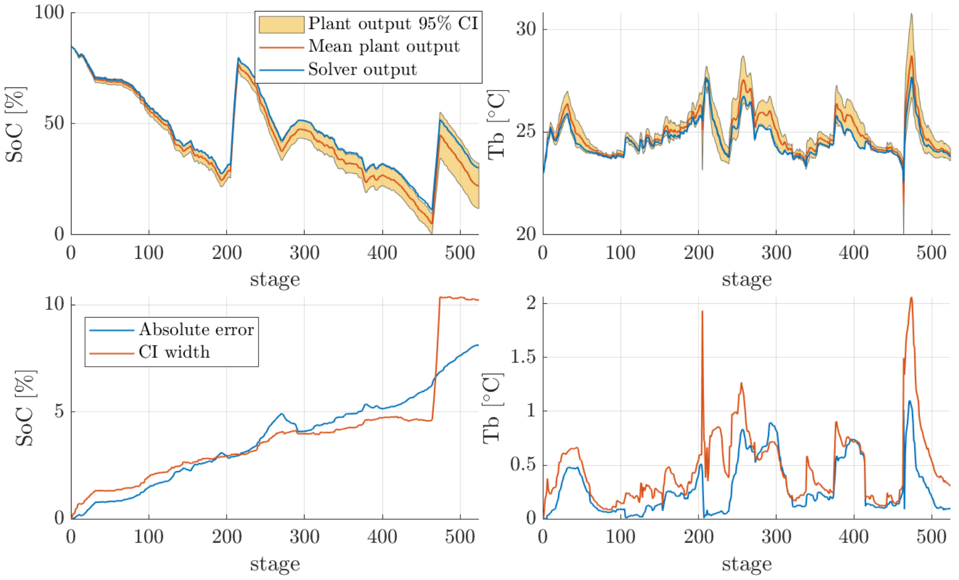

(a) Simulation using an erroneous plant model for the GK route using outputs from the hierarchical solver.

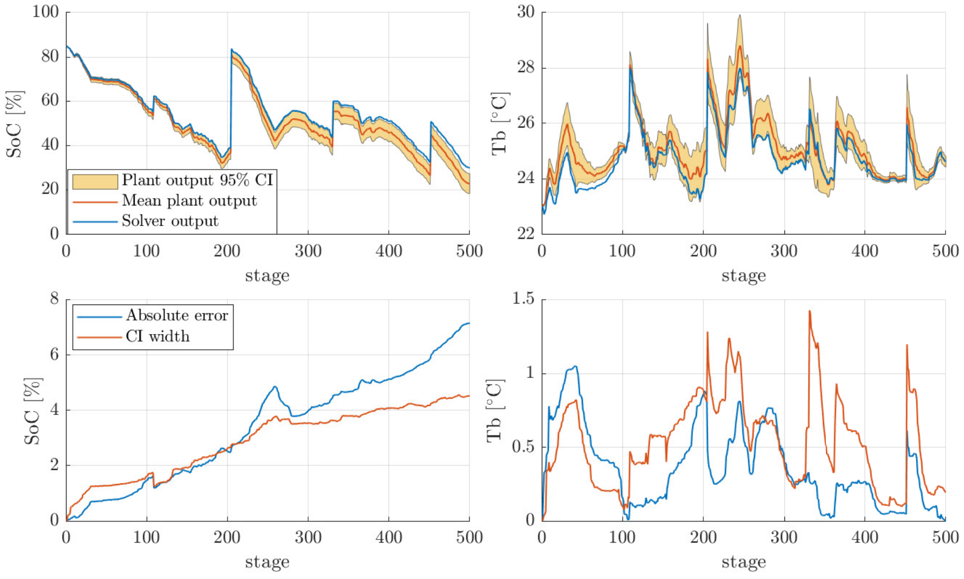

(b) Simulation using an erroneous plant model for the GK route using outputs from the sigmoid solver.

Figure 6.10: Plots of SoC and battery temperature mean and 95% CI from the 100 simulations on the GK route using the erroneous plant model described in section 5.2, plotted against the SoC and temperature trajectories given control inputs from the FORCESPRO solver output. The absolute error plots represent the absolute distance between the mean state trajectory and the simulation output in each stage, and the size of the 95% CI is plotted in the same graphs. The hierarchical solution was used in **(a)** and the sigmoid approximation was used in **(b)**.

6.4 Battery health evaluation

Two simulations were run on the GR and GK routes, with and without the inclusion of the C-rate in the charging stage cost function. The resulting normalized battery throughputs during charging are found in table 6.5, and plots of the battery temperature and C-rate during charging are found in figure 6.11.

Table 6.5: Normalized battery throughput during charging for the GR and GK routes, for the cost function including C-rate (case 1) and the cost function excluding C-rate (case 2).

Route	GR	GK
Case 1	0.9846	0.9982
Case 2	1	1

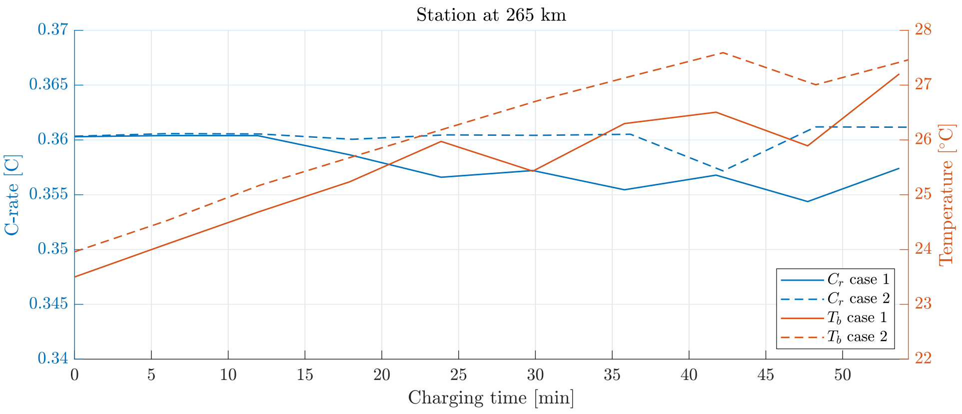

(a) C-rate and battery temperature plot during charging for the GR route.

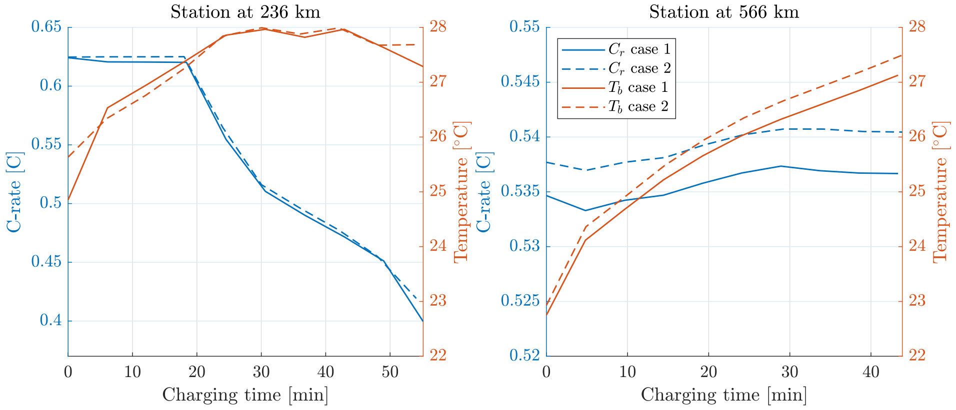

(b) C-rate and battery temperature plots during charging for the GK route.

Figure 6.11: C-rate and battery temperature trajectories during charging for the **(a)** GR route, **(b)** GK route. Two simulations are plotted for each route, one where the C-rate is included in the cost function (represented by the fully drawn lines, case 1) and one without it (represented by the dashed lines, case 2).

7

Discussion

7.1 Full solver evaluation

It can be seen in tables 6.1 and 6.2, for both routes, that the full hierarchical solution gives large savings in mainly charged energy and also in total trip costs in comparison to both the sigmoid solution to the MINLP and the heuristics solution. This result holds for all cases of added disturbances shown in section 6.1, even in those cases where the hierarchical solution is simulated for higher energy consumption. For both routes, it can be noted that the mission management solutions (hierarchical and sigmoid) handle the time-varying parameters better than the heuristics algorithm, and they also suggest charging strategies that end up closer to the target SoC of 30%. The time-varying speed limits are shown in figures 6.1 and 6.2, and in both cases the heuristics algorithm suggests charging strategies which result in the truck being stuck in the congestion - even in the GK route where the same station is selected as the mission management solvers choose. While the heuristics algorithm manages to keep the SoC within the limits $10\% - 87\%$, it does not manage to keep the battery temperature within the state bounds 22 °C to 28 °C as the maximum temperature violates those bounds. All these issues with the heuristics algorithm result from the fact that no actual optimization is being performed, which leads to no guarantee for state bounds being satisfied. However, the computation time of the heuristics algorithm is lower than the computation time of the mission management solvers.

In the case of the GR all the hierarchical solutions suggest stopping at station 7 in table 5.1, while the heuristic solver selects station 12 instead. The sigmoid solver instead suggests to stop at both stations 4 and 7. Given the time-varying speed limits defined for the GR route in section 5.1.1 it is likely that station 7 is the optimal charging station since by charging at this station the congestion is avoided and it also has the highest charging capacity in the surrounding area. The sigmoid solver however suggests charging an extra time, which results in a longer trip time since it leads to unnecessary queuing. Since the sigmoid solver does not include charging dynamics in the optimization, the temperature profile becomes discontinuous around the charging event and also reaches temperatures closer to the state bound, but the average battery temperature mostly matches the temperatures of the hierarchical solvers.

For the GK route, the hierarchical solver suggests charging twice as is seen in table

6.2, at stations that closely match the suggestions from the heuristic solver. Since the heuristic solution only charges at the last possible station and charges to full energy it means that 2 stations is the minimum amount of times that the driver can choose to charge and still make the trip, and both stations 10 and 22 are stations with high power capacity as is seen in table 5.2 which represents a close to optimal charging plan. The sigmoid solver however chooses to charge at 3 stations instead. This results in higher charging amounts and a longer trip time in comparison to the hierarchical solutions, and except for the high charging amount at the last station the plan is worse than the one suggested by the heuristics algorithm.

One cause for the extra charging stops suggested by the sigmoid solutions is that once chargers are closely spaced out together they end up having similar stage numbers and parameters after the discretization to 500 samples. Since the sigmoid activation function smoothens the charging decisions it means that there are fast derivative changes on stages where a charging decision is made, which can lead to the solver getting stuck in local minima of suboptimal charging when the stations are close together. This issue of suboptimality is avoided in the full hierarchical solver by using SDP, as that algorithm ensures that the optimal trajectories are followed given the discretized problem formulation.

7.2 Robustness

The robustness of the hierarchical solver is mainly shown through the results in section 6.3 which presents the simulations where a model mismatch has been introduced, but it can also be seen in section 6.2 where the station selection layer is evaluated. In the model mismatch evaluation, simulations have been performed using the optimal inputs from the FORCESPRO solver on a plant model which includes a mismatch that the solver was not aware of. It can be seen that the hierarchical solver is less sensitive to the perturbations in comparison to the sigmoid solver, which can be seen in table 6.4 and figures 6.9 and 6.10. It can be seen that for both routes, the SoC error increases almost linearly for the hierarchical solver, while a large error is introduced towards the end of the GR route for the sigmoid solver. The battery temperature errors however appear to be much more dependent on the actual power demand instead, becoming larger during stages of charging or when the road grade is steep and smaller during stages with low power demand. The same effect is seen for the CI:s of both the battery SoC and temperature, but in most cases, the uncertainty of the battery temperature is larger using the sigmoid solution in comparison to the hierarchical solution. This larger uncertainty in battery temperature is especially apparent in the GR route shown in figure 6.10b, where the maximum CI width is almost twice as wide as for the hierarchical solver. For the GK route, however, the absolute error and CI width of the SoC are slightly lower for the sigmoid solver. This is mainly because of the last charging instance for the hierarchical solver, where the error grows rapidly and afterward violates the state bounds on the SoC, with the CI almost reaching 0% completely depleting the battery. This shows that especially for longer and more demanding routes the plan would benefit from being reoptimized along the route to ensure that the state bounds are satisfied.

Aside from using the sigmoid activation function to avoid solving a MINLP, another difference between the sigmoid and hierarchical solvers is that the sigmoid solver does not consider any dynamics during the charging as it only uses space sampling to solve the optimization problem. This means that both the charging power and the battery reference temperature are considered constant during the whole charging period, which leads to suboptimal control of the battery SoC and temperature when the truck is charging. This is likely the main cause of the differences in the battery uncertainties since this introduces an integration error during the charging which is not accounted for and thus amplifies any inaccuracies that are present at the initial charging stage.

In the evaluation of the station selection layer in section 6.2, the performance of the SDP solver is shown for different initial SoC values. It is seen in figures 6.3 and 6.4 that the SoC is always kept comfortably within the state bounds, the lowest SoC of all four simulations being around 15%. From the results metrics presented in table 6.3 that in general, the trips become more expensive for lower initial SoC values which is also seen in the value function plot shown in figure 6.5. This is expected, since if the truck starts at a low charge then it will need to charge more along the trip, representing the longer charging times for lower SoC values requiring earlier departures. As is seen in the trip time map and the departure time policies in figures 6.7 and 6.8 this relation holds for most SoC values, except for around 60% where the departure time is earlier in comparison to both 50% and 70%. This is likely the case since if the initial SoC is around 60% then the truck does not have enough initial energy to reach station 7, and it has too high energy to make it worthwhile to stop stations 1 or 2. This means that station 6 becomes optimal to stop at, where the maximum capacity is low in comparison (only 75 kW), which then leads to a longer charging period and thus also requires an earlier departure time.

It can also be noted that in many cases the arrival time from the simulation output given by the SDP solver is after the target of 17.00, the same can also be seen in the final SoC which in all cases ends up with a mean of 32%. The likely cause of this discrepancy from the target values is that the policy suggested by the SDP is too conservative since it requires that the constraints are fulfilled in 95% of the time. Besides this, the final time is not a constraint in the optimization since it is only included in the construction of the time map shown in figure 6.7. This is however changed in the lower optimization layer, where no stochastic disturbances are considered and the final time is explicitly stated as a constraint, which leads to it being fulfilled for the full hierarchical solver as is seen in figures 6.1 and 6.2. Another interesting aspect is that the friction braking losses are higher for the trips that start with higher initial SoC, especially in comparison with the simulations from the full solver where the friction brake usage is minimal as can be seen in figures A.3 and B.3. Part of this is likely because the simplified model that is used in the upper layer does not include battery temperature in the optimization, which means that the full power range in figure 2.6 can not be utilized. Another aspect is that the conservative nature of the upper layer problem formulation guides the solution to higher SoC values to account for disturbances which also means that the battery charging power limits are lower - which in turn requires more usage of the friction brakes. This is also one likely cause for why the friction losses are higher for higher values of the initial SoC in table 6.3.

7.3 Battery health

In section 6.4 the results of the battery health evaluation are shown. It can be seen in table 6.5 and figure 6.11 that some benefits are had by including the C-rate in the charging cost functions. Overall both the C-rate and battery throughputs are decreased and the battery temperature is closer to the target of 27 °C. However, this decrease is very small especially when considering that it is only the C-rate while the truck is charging that has been considered since the charging periods only represent a small part of the total battery throughput of a route. It should also be noted that none of the stations in tables 5.1 and 5.2 can achieve any significantly high C-rate during charging, the highest capacity of all stations is 350.4 kW which for typical sizes of truck batteries in the range of 280 kWh to 565 kWh [60] representing possible C-rates of 0.62 C to 1.25 C. Greater benefits could then potentially be had by investigating routes that include MW charging stations, where C-rates exceeding 2 C are possible. It should also be noted that the C-rate was only considered during charging instances to encourage low degradation during charging. To get a full picture of the battery degradation, the C-rate during driving should also be considered. However, because the speed is not optimized in this thesis, the C-rate is not able to be controlled in the same way as during charging since the largest part of the power demand during driving comes from the EM. Thus it would likely not lead to any significantly large benefits to include the C-rate during driving using the problem formulation in this thesis, but if speed would be optimized then it would be beneficial to consider it during driving as well. In summary, the overall health benefits of the cost function benefits are inconclusive, but it still shows that the C-rate can be controlled by inclusion in the cost function. However, to achieve larger effects further tuning and investigation into other important battery parameters should also be performed.

7.4 Vehicle dynamics

To reduce the complexity and size of the optimization, several vehicle dynamics such as wheel slip, load transfers, horizontal forces, and gear selection have been disregarded. To fully capture the effect of those types of dynamics then significantly smaller spatial discretization step sizes would be necessary, which would make it intractable to perform the optimization on full trips. It is also the belief of the author that adding more complex modeling would not yield significant improvements in the optimal solution, although no study has been made on the effect. This claim is supported by the many similar models that are used for optimal charge planning and energy management in the literature, see for instance [33], [34], or [36].

7.5 Powertrain models

In the powertrain models, several simplifications were made to simplify the optimization model and reduce the number of states that were necessary. In the battery model, the equivalent circuit was simplified by assuming steady-state conditions on the internal battery voltages hold which reduced the number of states needed to represent the battery, as well as assuming that the terminal voltage and open circuit voltage are equal. Like with the vehicle dynamics, more complex models would need higher sampling frequencies than are used in this thesis to capture their effects. Because of this, it is believed that adding those dynamics to the model would not significantly change the accuracy of the predictions. Similar assumptions have been made on the battery model in for instance [34] and [35], but in comparison to their articles a different method is used to control the battery temperature in this thesis. The author believes that the accuracy of the power demand of the thermal systems is improved by using a high-fidelity model of the thermal management system to abstract the simplified models used in this thesis, instead of using constant efficiencies to represent heating/cooling. No tests have however been made to check the accuracy of the model, which could be done by simulating a higher fidelity model of the truck using the output from the hierarchical solver as a reference and comparing the power consumption.

7.6 Numerical optimization

7.6.1 Convergence

All optimizations using the FORCESPRO solver have been performed using the `nl_pdip` algorithm [55], [56] using a maximum number of solver iterations set to 1000. In all simulations using FORCESPRO, meaning simulations using the full hierarchical solver and the sigmoid solver, the maximum number of iterations has been reached. This means that the solver did not manage to find a solution that converged “well enough” within 1000 iterations. The termination criterias that are used by the solver are based on the KKT conditions in (3.8), where the stationarity condition (3.8a), the inequality constraints (3.8b), the equality constraints (3.8c) and the complementarity condition (3.8e) need to be fulfilled within certain tolerances. In this case, all tolerances are set equal to $\kappa = 0.001$. In figure 7.1 the infinity norm of KKT conditions residuals are plotted for 1000 iterations of a simulation running on the GK route, where the infinity norm of a vector is defined as $\|\mathbf{v}\|_\infty := \max_k |v_k|$. It can be seen that most conditions are not fulfilled within the tolerance κ and it can also be noted that almost no improvements in the optimality are found after around 350 iterations. This means that the KKT tolerances could be lowered while still keeping the solution quality, which would speed up the computation times. Scaling is also important to achieve good numerical performance. In general, within numerical optimization it helps if the variables are uniformly scaled within the range 0.01 to 100 [61], meaning that the problem might be more suitable if it’s discretized in kilometers instead of meters.

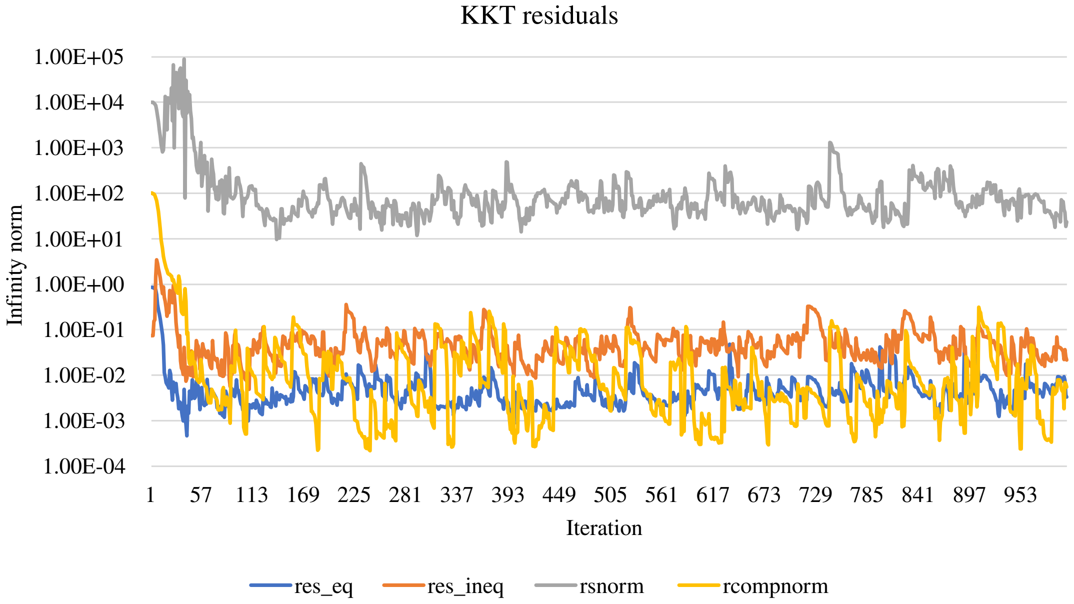

Figure 7.1: Infinity norm of the equality constraint residuals (`res_eq`), the inequality constraint residuals (`res_ineq`), the stationarity condition (`rsnorm`) and the complementarity condition violations (`rcompnorm`) for each solver iteration during optimization on the GK route. It can be noted that the residuals more or less stop converging after about ~ 350 iterations.

In figure 7.2 a comparison of single- and multiple-shooting state trajectories is shown for the same simulation on the GK route. This plot shows that while the solution might not fulfill the exit condition to the desired tolerance for an optimal solution, it is still a physical solutions since the state trajectories of the single- and multiple-shooting solutions are the same.

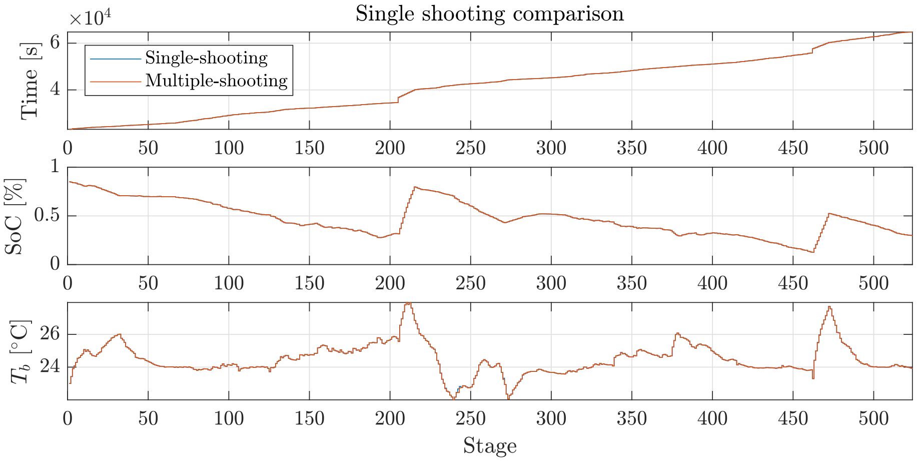

Figure 7.2: Comparison of state trajectories from the multiple-shooting simulation output of the FORCESPRO solver and a single-shooting simulation using the same plant model and optimal control inputs.

7.6.2 Computation times

The computation times of the NLP solver could be decreased partly by lowering tolerances or the maximum number of iterations, as is shown in the previous section. Another option is the change the optimization algorithm, for example to SQP. SQP algorithms are significantly faster for some optimization problems in comparison to IP methods [62]. The PDIP algorithms are however shown to be more robust than SQP, and in particular, the FORCESPRO implementation only supports affine inequality constraints. Thus, an investigation into using SQP algorithms might require an augmentation of the system model that is currently used. Other optimization software might also be used in these cases, such as ACADO [63] [64], which allows for more complex problem definitions.

7.7 Simulation

Since the mission manager is simulated using the same plant model as the optimizer uses, it is difficult to evaluate the real-world efficiency of the mission manager. It would therefore be of high interest to use the optimizer outputs in combination with a more high-fidelity model of the electric truck, to evaluate how large the model errors become and also as a further evaluation of the robustness of the station selections.

8

Conclusion

In this thesis, a supervisory controller for BEVs has been proposed which utilizes a hierarchical optimization scheme to plan charging and thermal management to minimize the total costs for a given trip. The controller outputs battery SoC, battery temperature, and battery power trajectories which can be used as references for online energy and thermal management systems, as well as plan charging stops along the route which can be suggested to the driver. The optimization is structured in two layers, where the upper layer selects optimal charging stations using SDP to solve a MINLP with simplified dynamics. The station selections are then sent to the lower layer which solves an NLP with more comprehensive dynamics to optimize the battery temperature and SoC. The station selections are made robust by optimizing for an uncertain traffic situation and charging station queuing times, and the gear selection is removed by assuming lower layer controllers always pick efficiency optimal gears at each vehicle speed and traction effort. The planner is evaluated on two routes of lengths 460 km and 660 km with recharging stations, and simulating using a 40 ton BEV truck. Its results are compared against a previously developed mission planner which solves an approximated NLP instead, and the simulations show that both costs and the total amount of recharging are lowered by using the hierarchical optimizer. For the 460 km route the cost is reduced by 7.8% and for the 660 km route it is reduced by 7.2%. It is also found that the robustness is improved in simulations where model errors are introduced and that it can handle time-dependent traffic disturbances such as congestion well.

An investigation was made into parameters that can reduce battery degradation, and it was found that the total throughput could be reduced by penalizing the battery C-rate during charging, but further investigation should be performed including adding costs to the C-rate during driving to find more conclusive results. To fully capture this effect the optimization of vehicle speed should be included in the lower layer of the optimization structure, to encourage energy-efficient driving. The study can also be extended by investigating re-optimizations along the route to analyze the solver's ability to re-plan a mission in the presence of large disturbances or deviations from the initially suggested plan. Finally, for long-range missions, the driving time limitations come into play. Thus an interesting aspect would be to introduce those limitations into the optimization to investigate how to combine the resting requirements with charging stops.

Bibliography

[1] Conference of the Parties, United Nations Framework Convention on Climate Change, "The paris agreement," 2015. [Online]. Available: `https://unfccc.int/process-and-meetings/the-paris-agreement`.

[2] European Commission, "Delivering the european green deal," 2021. [Online]. Available: `https://commission.europa.eu/strategy-and-policy/priorities-2019-2024/european-green-deal/delivering-european-green-deal_en#documents`.

[3] European Commission, "Commission welcomes completion of key 'fit for 55' legislation, putting eu on track to exceed 2030 targets," 2023. [Online]. Available: `https://ec.europa.eu/commission/presscorner/detail/en/ip_23_4754`.

[4] European Commission, "REPowerEU. Affordable, secure and sustainable energy for Europe," 2022. [Online]. Available: `https://commission.europa.eu/strategy-and-policy/priorities-2019-2024/european-green-deal/repowereu-affordable-secure-and-sustainable-energy-europe_en`.

[5] Directorate-General for Climate Action, European Commission, "Reducing CO_2 emissions from heavy-duty vehicles," 2023. [Online]. Available: `https://climate.ec.europa.eu/eu-action/transport/road-transport-reducing-co2-emissions-vehicles/reducing-co2-emissions-heavy-duty-vehicles_en`.

[6] European Parliament, Council of the European Union, *Regulation (EU) 2019/1242 of the European Parliament and of the Council of 20 June 2019 setting CO2 emission performance standards for new heavy-duty vehicles and amending regulations (EC) no 595/2009 and (EU) 2018/956 of the European parliament and of the Council and Council Directive 96/53/EC*, 2019. [Online]. Available: `https://eur-lex.europa.eu/eli/reg/2019/1242/oj`.

[7] AB Volvo. "How long-range electric trucks can already cover much of today's need." (2022), [Online]. Available: `https://www.volvotrucks.com/en-en/news-stories/insights/articles/2022/nov/long-range-electric-trucks-ready-today.html`.

[8] Scania. "Electric trucks have a range of up to 400 km." (n.d.), [Online]. Available: `https://www.scania.com/group/en/home/electrification/e-mobility-hub/electric-trucks-have-a-range-of-up-to-400-km.html`.

[9] European Alternative Fuels Observatory, Directorate-General for Mobility and Transport, "Electric vehicle recharging prices," European Commission, 2022. [Online]. Available: `https://alternative-fuels-observatory.ec.europa.eu/consumer-portal/electric-vehicle-recharging-prices`.

[10] Electromaps. "List of charging stations for electric vehicles in Sweden." (n.d.), [Online]. Available: `https://www.electromaps.com/en/charging-stations/sweden`.

[11] J. Lin, W. Zhou, and O. Wolfson, "Electric vehicle routing problem," *Transportation Research Procedia*, vol. 12, pp. 508–521, 2016, Tenth International Conference on City Logistics 17-19 June 2015, Tenerife, Spain, ISSN: 2352-1465. DOI: `10.1016/j.trpro.2016.02.007`. [Online]. Available: `https://www.sciencedirect.com/science/article/pii/S2352146516000089`.

[12] S. Shao, W. Guan, and J. Bi, "Electric vehicle-routing problem with charging demands and energy consumption," *IET Intelligent Transport Systems*, vol. 12, no. 3, pp. 202–212, 2018. DOI: `10.1049/iet-its.2017.0008`. eprint: `https://ietresearch.onlinelibrary.wiley.com/doi/pdf/10.1049/iet-its.2017.0008`. [Online]. Available: `https://ietresearch.onlinelibrary.wiley.com/doi/abs/10.1049/iet-its.2017.0008`.

[13] S. Erdoğan and E. Miller-Hooks, "A green vehicle routing problem," *Transportation Research Part E: Logistics and Transportation Review*, vol. 48, no. 1, pp. 100–114, 2012, Select Papers from the 19th International Symposium on Transportation and Traffic Theory, ISSN: 1366-5545. DOI: `10.1016/j.tre.2011.08.001`. [Online]. Available: `https://www.sciencedirect.com/science/article/pii/S1366554511001062`.

[14] R. Basso, B. Kulcsár, B. Egardt, P. Lindroth, and I. Sanchez-Diaz, "Energy consumption estimation integrated into the electric vehicle routing problem," *Transportation Research Part D: Transport and Environment*, vol. 69, pp. 141–167, 2019, ISSN: 1361-9209. DOI: `https://doi.org/10.1016/j.trd.2019.01.006`. [Online]. Available: `https://www.sciencedirect.com/science/article/pii/S1361920918304760`.

[15] R. Basso, B. Kulcsár, and I. Sanchez-Diaz, "Electric vehicle routing problem with machine learning for energy prediction," *Transportation Research Part B: Methodological*, vol. 145, pp. 24–55, 2021, ISSN: 0191-2615. DOI: `10.1016/j.trb.2020.12.007`. [Online]. Available: `https://www.sciencedirect.com/science/article/pii/S0191261520304549`.

[16] R. Basso, B. Kulcsár, I. Sanchez-Diaz, and X. Qu, "Dynamic stochastic electric vehicle routing with safe reinforcement learning," *Transportation Research Part E: Logistics and Transportation Review*, vol. 157, p. 102 496, 2022, ISSN: 1366-5545. DOI: `10.1016/j.tre.2021.102496`. [Online]. Available: `https://www.sciencedirect.com/science/article/pii/S1366554521002581`.

[17] E. W. Dijkstra, "A note on two problems in connexion with graphs," *Numerische Mathematik*, vol. 1, pp. 269–271, 1959. DOI: `10.1007/BF01386390`.

[18] Y. Marinakis, A. Migdalas, and P. M. Pardalos, "A new bilevel formulation for the vehicle routing problem and a solution method using a genetic algorithm," *Journal of Global Optimization*, vol. 38, pp. 555–580, 2007. DOI: `10.1007/s10898-006-9094-0`.

[19] H. I. Calvete, C. Galé, J. A. Iranzo, and P. Toth, "The school bus routing problem with student choice: A bilevel approach and a simple and effective metahueristic," *International transactions in operational research*, vol. 30, no. 2, pp. 1092–1119, 2021. DOI: `10.1111/itor.12951`.

[20] G.-E. Karsargyri, “Optimally controlling hybrid electric vehicles using path forecasting,” Department of Electrical Engineering and Computer Science. Massachussets Institute of Technology, 2008. [Online]. Available: `http://hdl.handle.net/1721.1/44455`.

[21] R. Bellman, “The theory of dynamic programming,” *Bulletin of the American Mathematical Society*, vol. 60, pp. 503–516, 1954. DOI: `10.1090/S0002-9904-1954-09848-8`.

[22] G.-E. Katsargyri, I. Kolmanovsky, J. Michelini, *et al.*, “Path dependent receding horizon control policies for hybrid electric vehicles,” *2009 IEEE Control Applications, (CCA) & Intelligent Control, (ISIC)*, pp. 607–612, 2009. DOI: `10.1109/CCA.2009.5280977`.

[23] L. Johannesson, E. Jonasson, J. Hellgren, and B. Egardt, “Predictive energy management of hybrid long-haul trucks,” *Control Engineering Practice*, vol. 41, pp. 83–97, 2015. DOI: `10.1016/j.conengprac.2015.04.014`.

[24] L. Johannesson, M. Nilsson, and N. Murgovski, “Look-ahead vehicle energy management with traffic predictions,” *IFAC-PapersOnLine*, vol. 48, no. 15, pp. 244–251, 2015, 4th IFAC Workshop on Engine and Powertrain Control, Simulation and Modeling E-COSM 2015, ISSN: 2405-8963. DOI: `10.1016/j.ifacol.2015.10.035`. [Online]. Available: `https://www.sciencedirect.com/science/article/pii/S2405896315019114`.

[25] S. Uebel, N. Murgovski, C. Tempelhahn, and B. Bäker, “Optimal energy management and velocity control of hybrid electric vehicles,” *IEEE Transactions on Vehicular Technology*, vol. 67, no. 1, pp. 327–337, 2018, ISSN: 0018-9545. DOI: `10.1109/TVT.2017.2727680`.

[26] L. S. Pontryagin, V. G. Boltyanskii, R. V. Gamkrelidze, and E. F. Mishchenko, *The Mathematical Theory of Optimal Processes*. New York, NY, USA: Interscience, 1962.

[27] H. Lim and W. Su, “Hierarchical energy management for power-split plug-in hevs using distance-based optimized speed and soc profiles,” *IEEE Transactions on Vehicular Technology*, vol. 67, no. 12, pp. 9312–9323, 2018, ISSN: 0018-9545. DOI: `10.1109/TVT.2018.2862945`.

[28] S. Zendegan, A. Ferrara, S. Jakubek, and C. Hametner, “Predictive battery state of charge reference generation using basic route information for optimal energy management of heavy-duty fuel cell vehicles,” *IEEE Transactions on Vehicular Technology*, vol. 70, pp. 12 517–12 528, 2021, ISSN: 0018-9545. DOI: `10.1109/TVT.2021.3121129`.

[29] C. Vagg, S. Akehurst, C. J. Brace, and L. Ash, “Stochastic dynamic programming in the real-world control of hybrid electric vehicles,” *IEEE Transactions on Control Systems Technology*, vol. 24, no. 3, pp. 853–866, 2016. DOI: `10.1109/TCST.2015.2498141`.

[30] C. Yang, S. You, W. Wang, L. Li, and C. Xiang, “A stochastic predictive energy management strategy for plug-in hybrid electric vehicles based on fast rolling optimization,” *IEEE Transactions on Industrial Electronics*, vol. 67, no. 11, pp. 9659–9670, 2020, ISSN: 0278-0046. DOI: `10.1109/TIE.2019.2955398`.

[31] A. L. Rhun, “Stochastic optimal control for the energy management of hybrid electric vehicles under traffic constraints,” Ph.D. dissertation, Optimization

and Control. Université Paris Saclay, 2019. [Online]. Available: `https://theses.hal.science/tel-02443292`.

[32] C.-C. Lin, H. Peng, and J. Grizzle, "A stochastic control strategy for hybrid electric vehicles," in *Proceedings of the 2004 American Control Conference*, vol. 5, 2004, pp. 4710–4715. DOI: `10.23919/ACC.2004.1384056`.

[33] S. Souley, K. Gillet, G. Colin, A. Simon, C. Nouillant, and Y. Chamaillard, "Optimization of the travel time of an electric vehicle with consideration of the recharging terminals," in *16th IFAC Symposium on Control in Transportation Systems, CTS 2021*, ser. IFAC PapersOnline, Lille. France, Jun. 2021. [Online]. Available: `https://hal.science/hal-03279281`.

[34] A. Hamednia, N. Murgovski, J. Forsman, M. Pourabdollah, V. Larsson, and J. Fredriksson, "Optimal thermal management, charging, and eco-driving of battery electric vehicles," *IEEE Transactions on Vehicular Technology*, vol. 72, no. 11, pp. 7265–7278, 2023. DOI: `10.1109/TVT.2023.3240279`.

[35] A. Hamednia, V. Hanson, J. Zhao, *et al.*, "Charge planning and thermal management of battery electric vehicles," *IEEE Transactions on Vehicular Technology*, vol. 72, no. 11, pp. 14 141–14 154, 2023. DOI: `10.1109/TVT.2023.3284916`.

[36] A. Bragde and D. Sundberg, "Mission management for fuel cell heavy-duty trucks," Department of Electrical Engineering. Chalmers University of Technology, 2023. [Online]. Available: `http://hdl.handle.net/20.500.12380/306509`.

[37] Directorate-General for Mobility and Transport, European Commission. "Driving time and rest periods." (2006), [Online]. Available: `https://transport.ec.europa.eu/transport-modes/road/social-provisions/driving-time-and-rest-periods_en`.

[38] I. Pena-Arenas, T. Garaix, P. Lacomme, and N. Tchernev, "A mixed integer programming formulation for the truck drivers scheduling problem considering the european union drivers rules.," *2021 IEEE 17th International Conference on Automation Science and Engineering (CASE), Automation Science and Engineering (CASE), 2021 IEEE 17th International Conference on*, pp. 101–106, 2021, ISSN: 978-1-6654-1873-7. DOI: `10.1109/CASE49439.2021.9551634`.

[39] D. Mukherjee, "Effect of pavement conditions on rolling resistance," *American Journal of Engineering Research*, vol. 3, no. 7, pp. 141–148, 2014, ISSN: 2320-0936. [Online]. Available: `https://www.ajer.org/papers/v3(7)/R037141148.pdf`.

[40] H. Stenvall, "Driving resistance analysis of long haulage trucks at Volvo," Department of Applied Mechanics. Chalmers University of Technology, 2010. [Online]. Available: `https://hdl.handle.net/20.500.12380/133658`.

[41] G. Paterlini and S. Yucel, "Rolling resistance validation," Minnesota Department of Transportantion, Tech. Rep., 2015. [Online]. Available: `https://hdl.handle.net/20.500.14153/mndot.3029`.

[42] I. Cowie, "All about batteries, part 12: Lithium Titanite (LTO)," *EETimes*, 2015. [Online]. Available: `https://www.eetimes.com/all-about-batteries-part-12-lithium-titanate-lto/`.

[43] T. Huria, M. Ceraolo, J. Gazzarri, and R. Jackey, "High fidelity electrical model with thermal dependence for characterization and simulation of high power lithium battery cells," in *2012 IEEE International Electric Vehicle Conference*, 2012, pp. 1–8. DOI: `10.1109/IEVC.2012.6183271`.

[44] C. Zou, A. Klintberg, Z. Wei, B. Fridholm, T. Wik, and B. Egardt, "Power capability prediction for lithium-ion batteries using economic nonlinear model predictive control," *Journal of Power Sources*, vol. 396, pp. 580–589, 2018, ISSN: 0378-7753. DOI: `10.1016/j.jpowsour.2018.06.034`. [Online]. Available: `https://www.sciencedirect.com/science/article/pii/S037877531830630X`.

[45] L. Timilsina, P. R. Badr, P. H. Hoang, G. Ozkan, B. Papari, and C. S. Edrington, "Battery degradation in electric and hybrid electric vehicles: A survey study," *IEEE Access*, vol. 11, pp. 42 431–42 462, 2023. DOI: `10.1109/ACCESS.2023.3271287`.

[46] J. Qu, Z. Jiang, and J. Zhang, "Investigation on lithium-ion battery degradation induced by combined effect of current rate and operating temperature during fast charging," *Journal of Energy Storage*, vol. 52, p. 104 811, 2022, ISSN: 2352-152X. DOI: `10.1016/j.est.2022.104811`. [Online]. Available: `https://www.sciencedirect.com/science/article/pii/S2352152X22008209`.

[47] Z. Gao, H. Xie, X. Yang, W. Niu, S. Li, and S. Chen, "The dilemma of c-rate and cycle life for lithium-ion batteries under low temperature fast charging," *Batteries*, vol. 8, no. 11, 2022, ISSN: 2313-0105. DOI: `10.3390/batteries8110234`. [Online]. Available: `https://www.mdpi.com/2313-0105/8/11/234`.

[48] A. Ganesan, S. Gros, and N. Murgovski, "Numerical strategies for mixed-integer-optimization of power-split and gear selection in hybrid electric vehicles," *IEEE Transactions on Intelligent Transportation Systems*, vol. 24, no. 3, pp. 3194–3210, 2023, ISSN: 1558-0016. DOI: `10.1109/TITS.2022.3229254`.

[49] L. C. Evans, *An introduction to mathematical optimal control theory version 0.2*. 1983. [Online]. Available: `http://math.berkeley.edu/%5C%5C~evans/control.course.pdf`.

[50] S. Gros and M. Diehl, *Manuscript of Numerical Optimal Control (Draft)*. 2022. [Online]. Available: `https://www.syscop.de/files/2020ss/NOC/book-NOCSE.pdf`.

[51] D. P. Bertsekas and S. E. Shreve, *Stochastic Optimal Control: The discrete time case*. Belmont, MA: Athena Scientific, 1978. [Online]. Available: `https://web.mit.edu/dimitrib/www/soc.html`.

[52] R. D. McAllister and J. B. Rawlings, "Nonlinear stochastic model predictive control: Existence, measurability, and stochastic asymptotic stability," *IEEE Transactions on Automatic Control*, vol. 68, no. 3, pp. 1524–1536, 2023. DOI: `10.1109/TAC.2022.3157131`.

[53] D. P. Bertsekas, "Dynamic Programming and Stochastic Control," *MIT OpenCourseWare*, 2015. [Online]. Available: `https://ocw.mit.edu/courses/6-231-dynamic-programming-and-stochastic-control-fall-2015/`.

[54] V. A. Bavdekar and A. Mesbah, "Stochastic nonlinear model predictive control with joint chance constraints," *IFAC-PapersOnLine*, vol. 49, no. 18, pp. 270–275, 2016, 10th IFAC Symposium on Nonlinear Control Systems NOLCOS 2016, ISSN: 2405-8963. DOI: `10.1016/j.ifacol.2016.10.176`. [Online].

Available: `https://www.sciencedirect.com/science/article/pii/S2405896316317554`.

[55] Embotech AG, *FORCESPRO*, 2014–2024. [Online]. Available: `https://forces.embotech.com/`.

[56] A. Zanelli, A. Domahidi, J. Jerez, and M. Morari, “FORCES NLP: An efficient implementation of interior-point methods for multistage nonlinear nonconvex programs,” *International Journal of Control*, vol. 93, pp. 13–29, 2020. DOI: `10.1080/00207179.2017.1316017`.

[57] C. Moler, “Numerical computing with matlab,” in The MathWorks, Inc, 2004, ch. Interpolation. [Online]. Available: `https://www.mathworks.com/content/dam/mathworks/mathworks-dot-com/moler/interp.pdf`.

[58] C. Farkas and L. Prikler, “Stochastic modelling of ev charging at charging stations,” *Renewable Energies Power Quality*, vol. 1, pp. 1046–1051, 2012.

[59] OpenStreetMap contributors, *Planet dump retrieved from https://planet.osm.org*, `https://www.openstreetmap.org`, 2017.

[60] AB Volvo. “Our electric truck range.” (2024), [Online]. Available: `https://www.volvotrucks.com/en-en/trucks/electric.html`.

[61] CasADI. “On the importance of nlp scaling.” (2018), [Online]. Available: `https://web.casadi.org/blog/nlp-scaling/`.

[62] Embotech. “Forcespro documentation, Sequential quadratic programming algorithm.” (2024), [Online]. Available: `https://forces.embotech.com/Documentation/high_level_interface/index.html#sequential-quadratic-programming-algorithm`.

[63] B. Houska, H. Ferreau, and M. Diehl, “ACADO Toolkit – An Open Source Framework for Automatic Control and Dynamic Optimization,” *Optimal Control Applications and Methods*, vol. 32, no. 3, pp. 298–312, 2011.

[64] B. Houska, H. Ferreau, M. Vukov, and R. Quirynen, *ACADO Toolkit User’s Manual*, `http://www.acadotoolkit.org`, 2009–2013.

A

Gothenburg-Rødby simulation plots

In this appendix additional simulation plots are shown for the GR route. In figure 6.1 the time-varying speed distribution of the GR route is shown with a plot of the trip time for the simulations using the hierarchical solver. In figure A.1-A.4 simulation plots of the hierarchical solutions are found, figure A.5 demonstrates the sigmoid simulation plots and plots of the heuristic solution are shown in figure A.6. First, figure A.1 shows a comparison of the speed profile, selected charging station, and altitude profile for the disturbance cases.

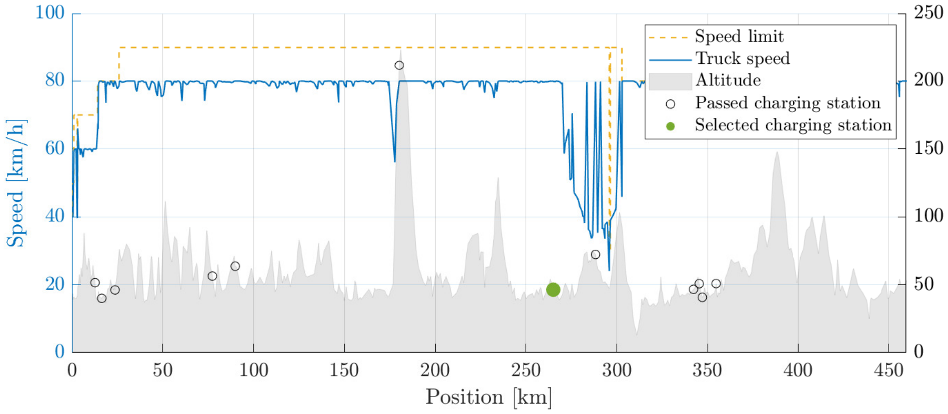

(a) Speed profile using only the mean value as a disturbance.

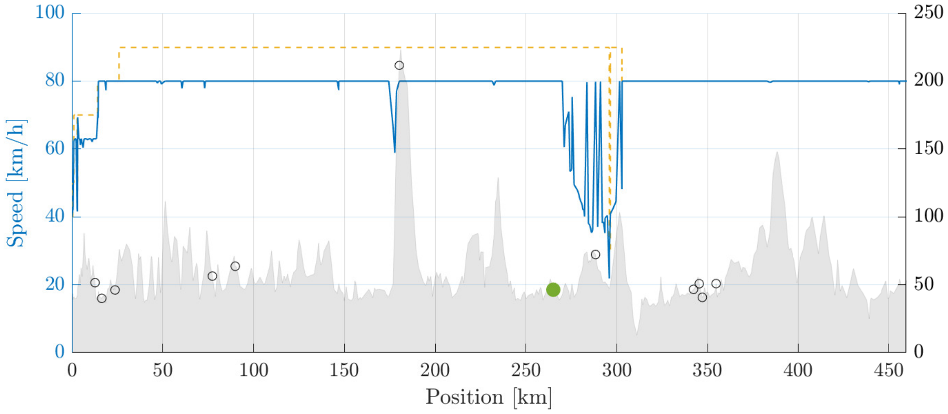

(b) Speed profile for a higher energy consumption.

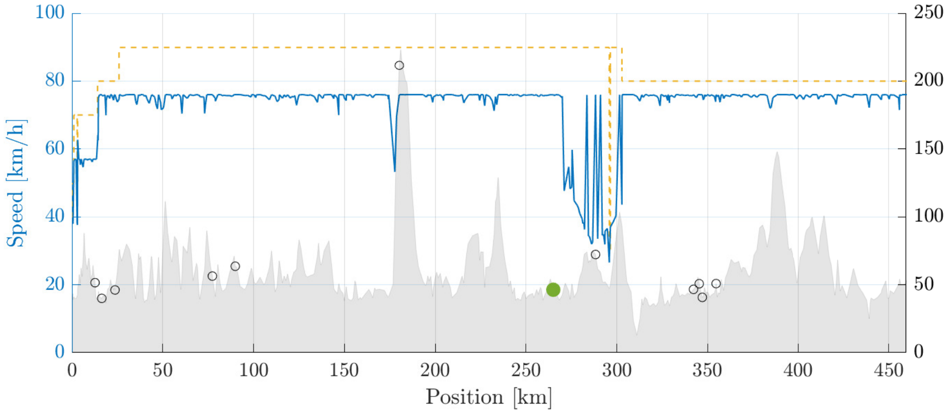

(c) Speed profile for a lower energy consumption.

Figure A.1: Altitude profile, speed limits, and truck speed for the GR route. The optimal charging station is marked green in the plots, representing station 7 in table 5.1, the other station locations are shown as the unfilled black markers. Sub figures **(a)**-**(c)** represent the disturbance cases a-c which are described in section 5.1.

Also, figure A.2 compares the battery power and SoC trajectories for the disturbance cases, as well as shows the charging time at the selected stations.

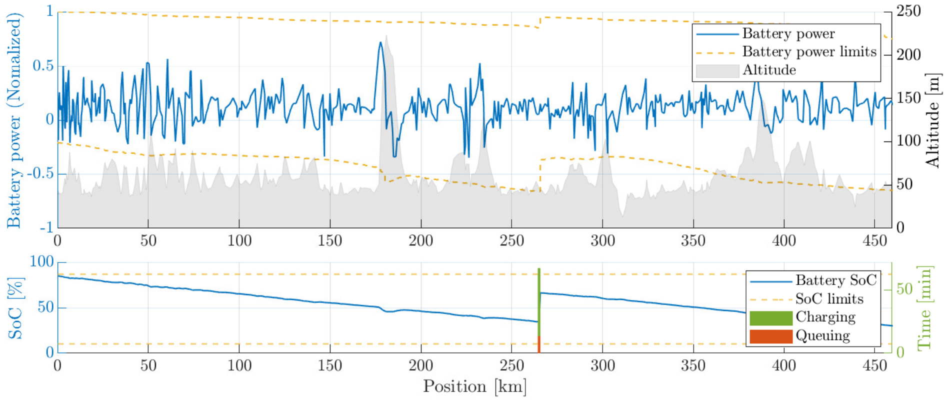

(a) Battery profile using only the mean value as a disturbance.

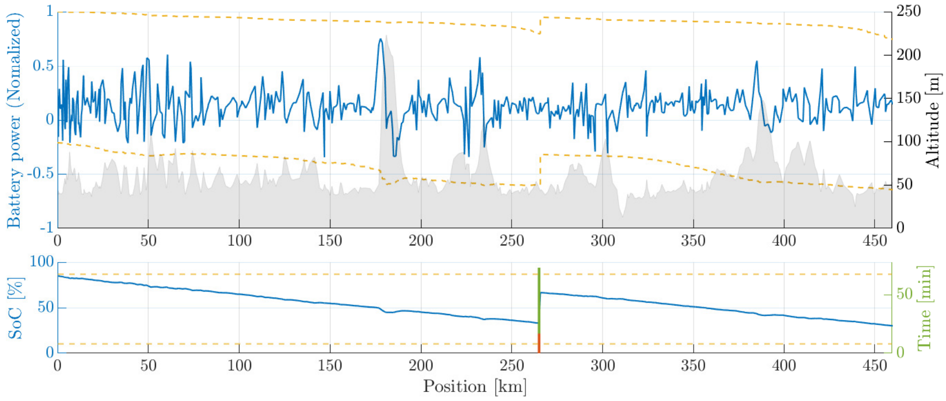

(b) Battery profile for a higher energy consumption.

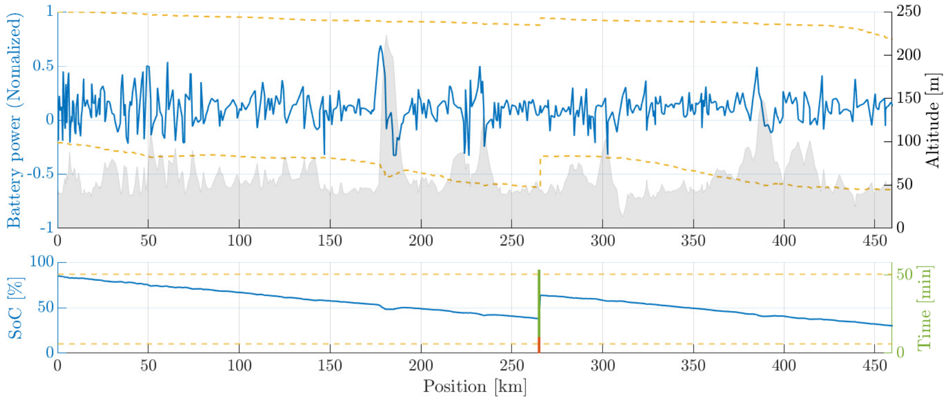

(c) Battery profile for a lower energy consumption.

Figure A.2: Battery power and SoC trajectories for the GR route with no time-dependent parameters. Sub figures **(a)**-**(c)** represent the disturbance cases a-c which are described in section 5.1. The optimal solutions are to charge for 51, 53.2 respectively 41.2 minutes at station 7, where the queuing time is 14.4, 17.9 respectively 11 minutes.

Moreover, figure A.3 illustrates the traction effort, friction brake usage, battery temperature, and battery heat flow for the simulations using the hierarchical solver.

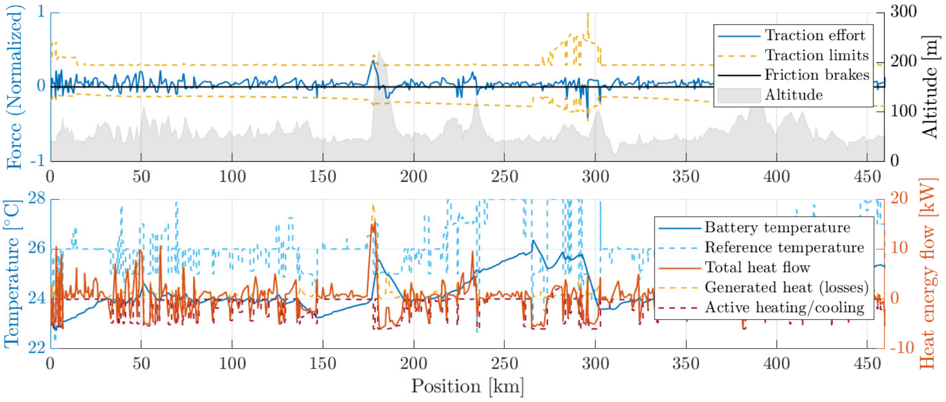

(a) Temperature profile using only the mean value as a disturbance.

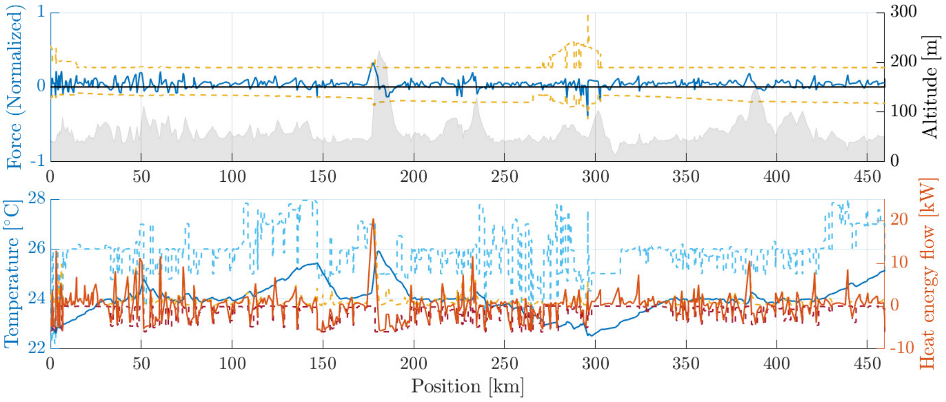

(b) Temperature profile for a higher energy consumption.

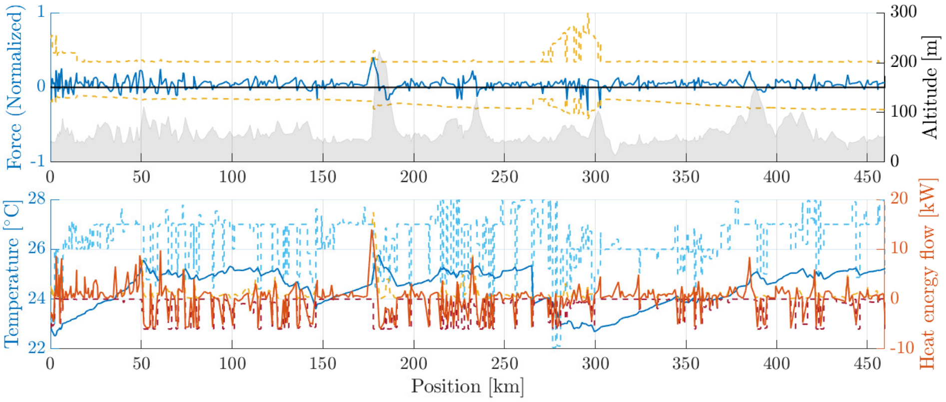

(c) Temperature profile for a lower energy consumption.

Figure A.3: Traction effort, friction brake usage, battery temperature, and heat flow for the GR route. Friction brake usage is minimal for this case and the temperature is mostly kept around $24-25\,^{\circ}$C. Sub figures **(a)**-**(c)** represent the disturbance cases a-c which are described in section 5.1.

Furthermore, figure A.4 shows the charging power and battery SoC and temperature profiles during charging for the different disturbance cases.

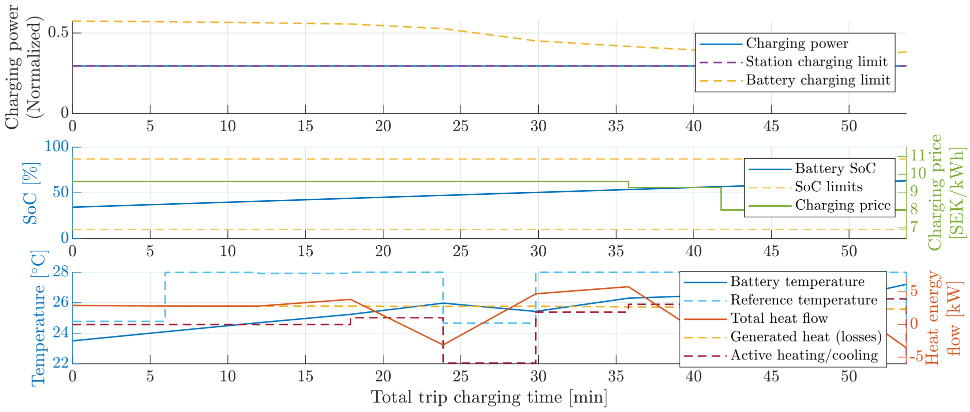

(a) Station profile using only the mean value as a disturbance.

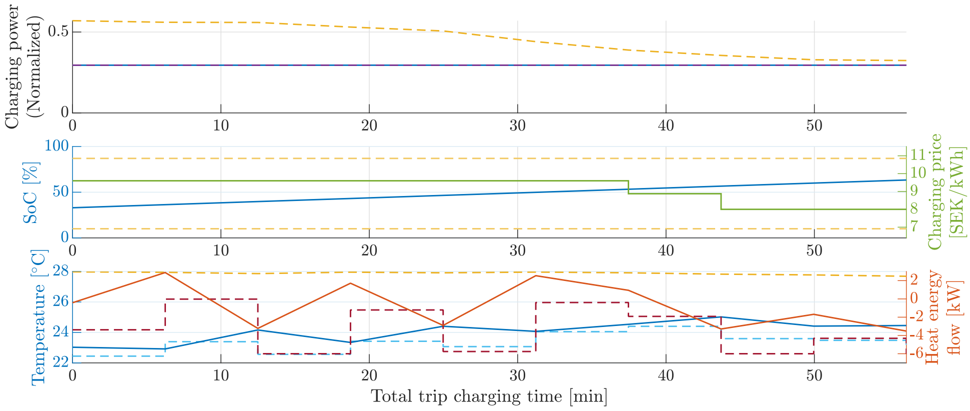

(b) Station profile for a higher energy consumption.

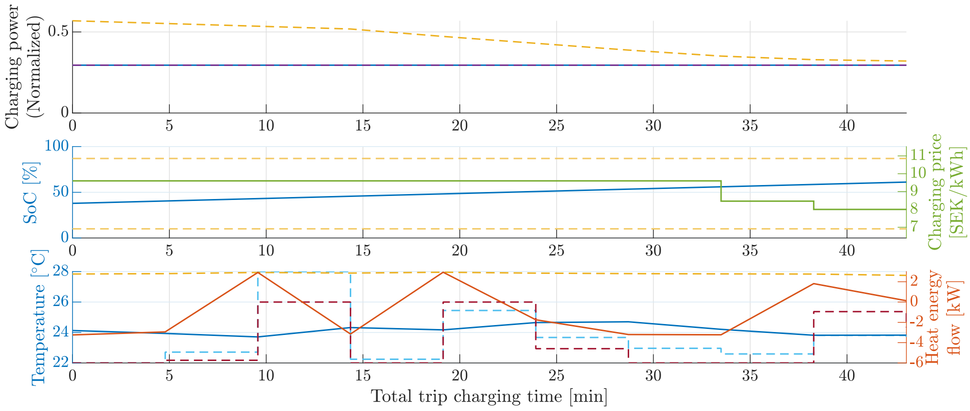

(c) Station profile for a lower energy consumption.

Figure A.4: Plots of the charging power, battery SoC, and temperature for the GR route. The plots are the state and input trajectories during charging at the selected station at 265 km. Sub figures **(a)**-**(c)** represent the disturbance cases a-c which are described in section 5.1.

In figure A.5, the speed, battery, and temperature profiles using the sigmoid solution are plotted.

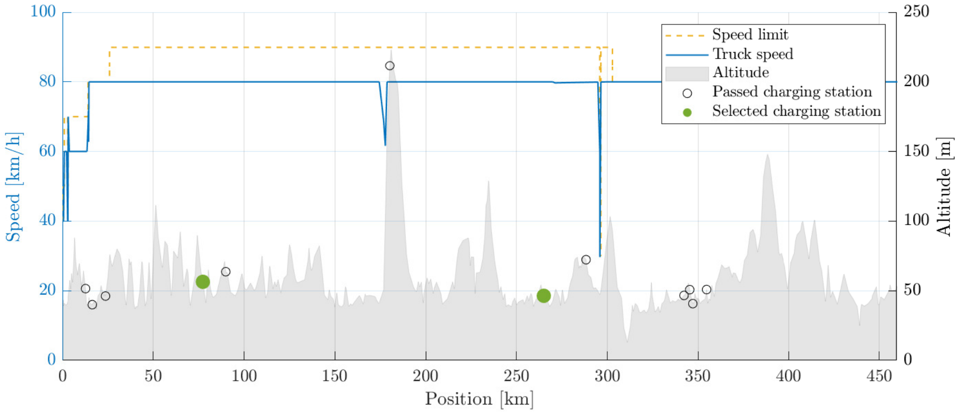

(a) Speed profile of the sigmoid solution.

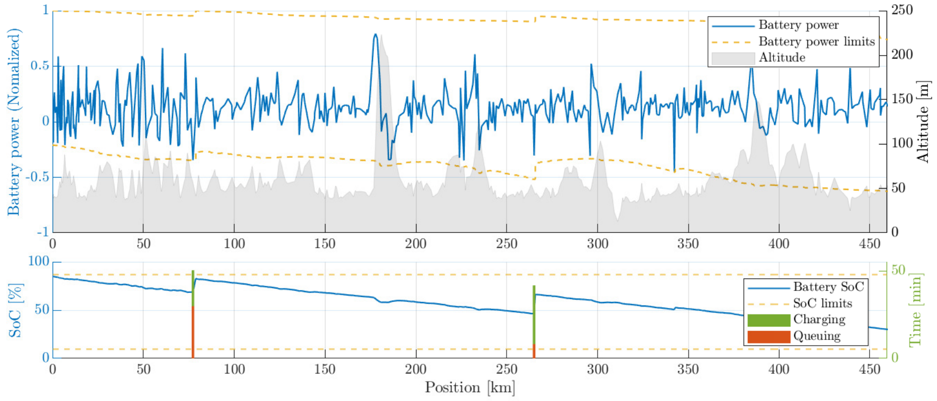

(b) Battery profile of the sigmoid solution.

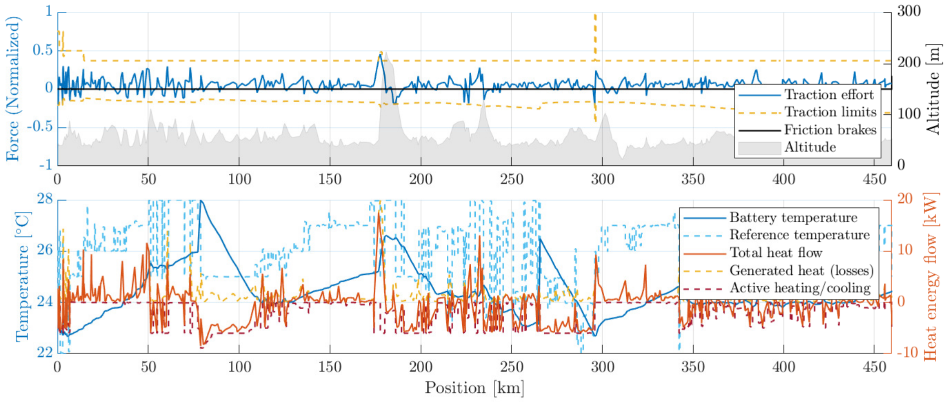

(c) Temperature profile of the sigmoid solution.

Figure A.5: Speed, battery, and temperature profiles for GR route using the sigmoid approximation to solve the problem. Note that the solution in this case is to instead charge for 20.6 minutes at station 4 and 33.6 minutes at station 7. The sigmoid solution does not include charging dynamics and thus the station profile is not present.

Finally, figure A.6 shows the speed, battery, and temperature profiles found using the heuristics algorithm.

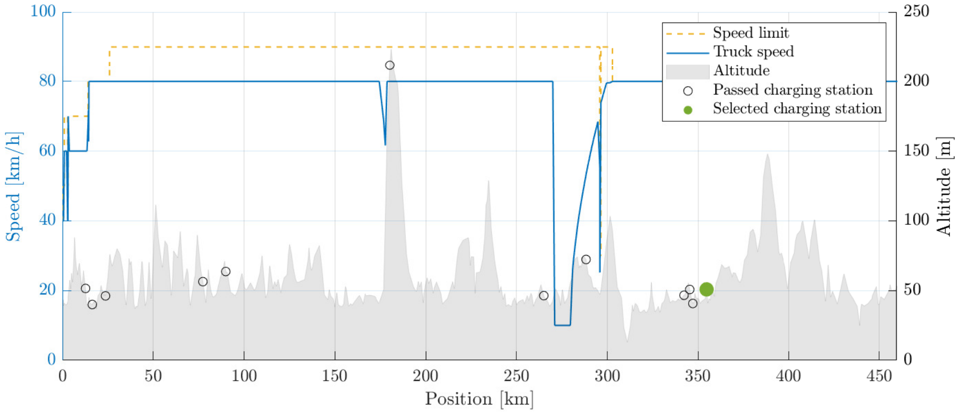

(a) Speed profile from the heuristics solution.

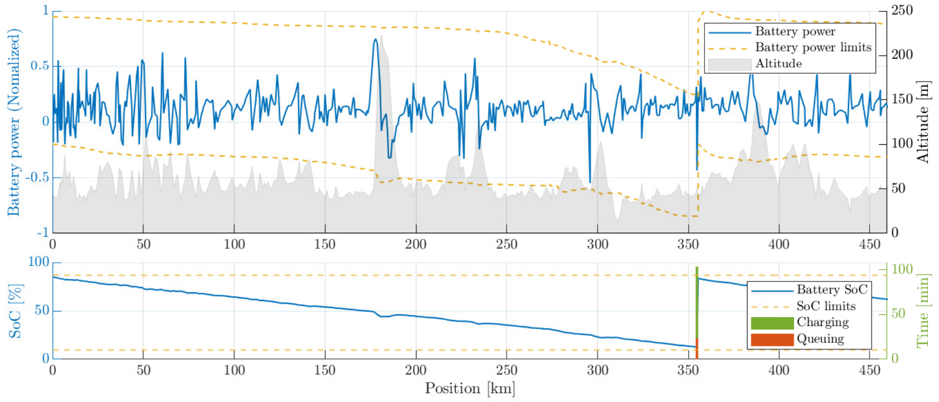

(b) Battery profile from the heuristics solution.

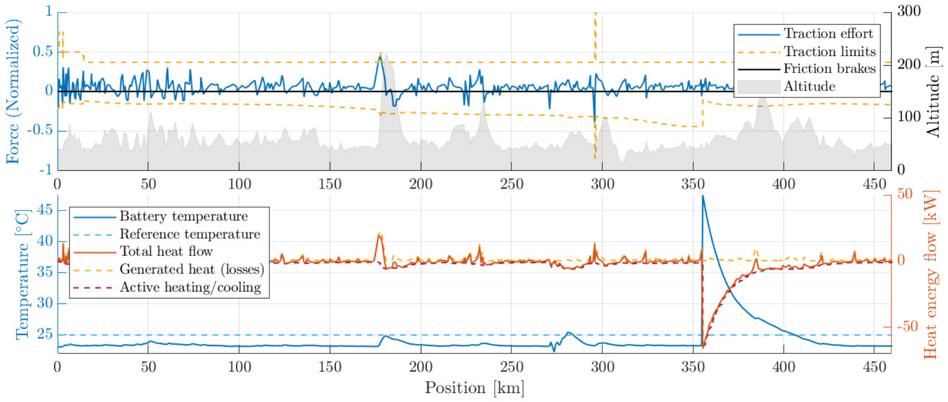

(c) Temperature profile from the heuristics solution.

Figure A.6: Speed, battery, and temperature profiles for LR route using the heuristics algorithm to solve the problem. The suggested solution in this case is to charge for 80 minutes at station 12. The heuristics solution does not include charging dynamics and thus the station profile is not present.

B

Genoa-Karlsruhe simulation plots

In this appendix additional simulation plots are shown for the GK route. In figure B.1-B.4 simulation plots of the hierarchical solutions are found, figure B.5 demonstrates the sigmoid simulation plots and plots of the heuristic solution are shown in figure B.6. First, figure B.1 shows a comparison of the speed profile, selected charging station, and altitude profile for the disturbance cases.

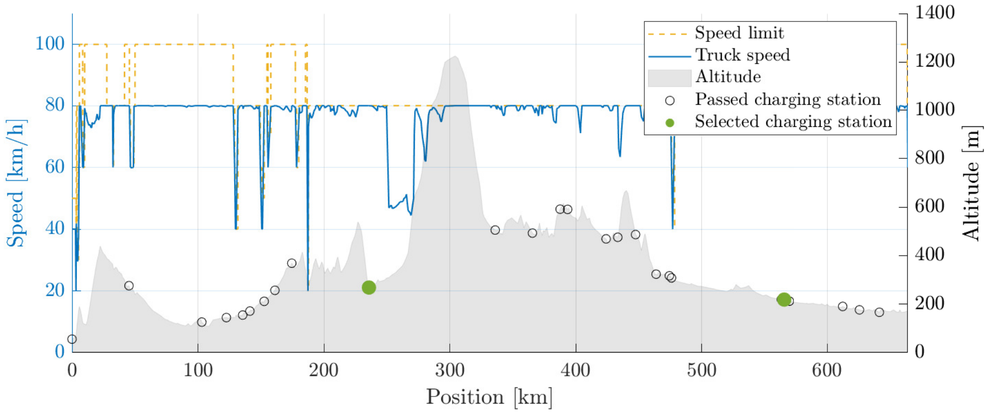

(a) Speed profile using only the mean value as a disturbance.

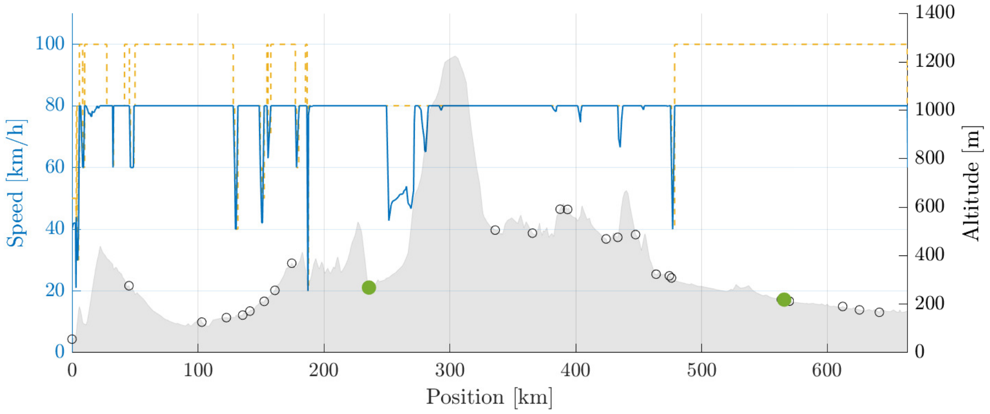

(b) Speed profile for a higher energy consumption.

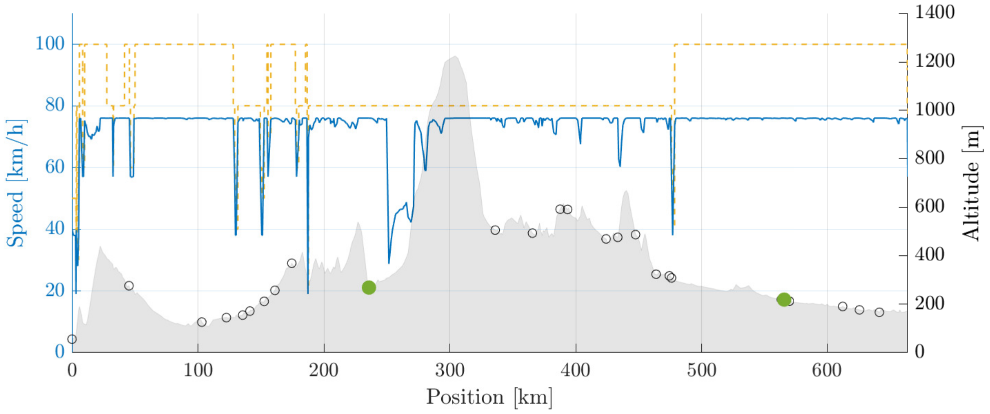

(c) Speed profile for a lower energy consumption.

Figure B.1: Altitude profile, speed limits, and truck speed for the GK route. The optimal charging stations are marked green in the plot, representing stations 10 and 22 in table 5.2, the other station locations are shown as the unfilled black markers. Sub figures **(a)**-**(c)** represent the disturbance cases a-c which are described in section 5.1.

Also, figure B.2 compares the battery power and SoC trajectories for the disturbance cases, as well as shows the charging time at the selected stations.

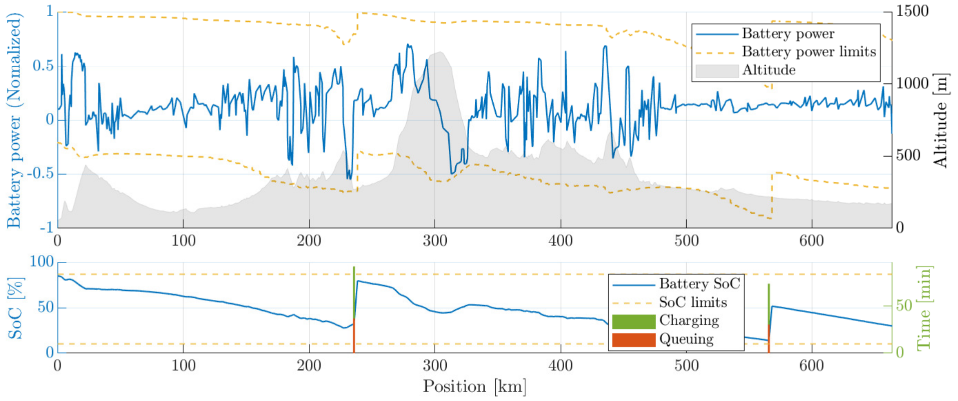

(a) Battery profile using only the mean value as a disturbance.

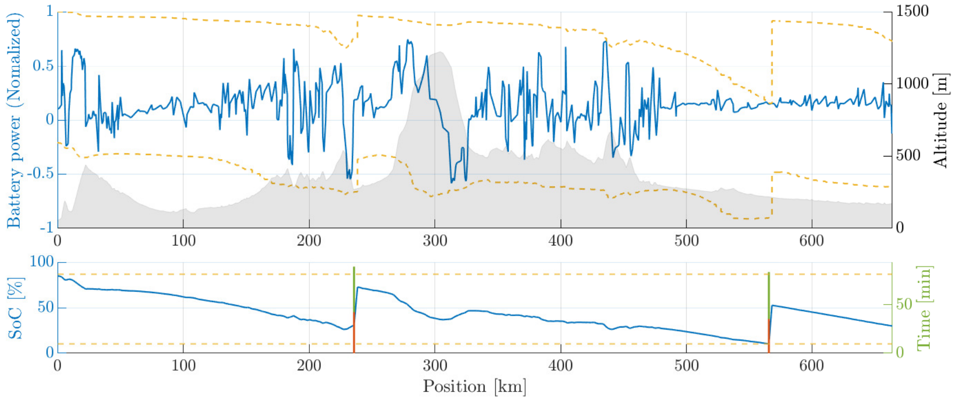

(b) Battery profile for a higher energy consumption.

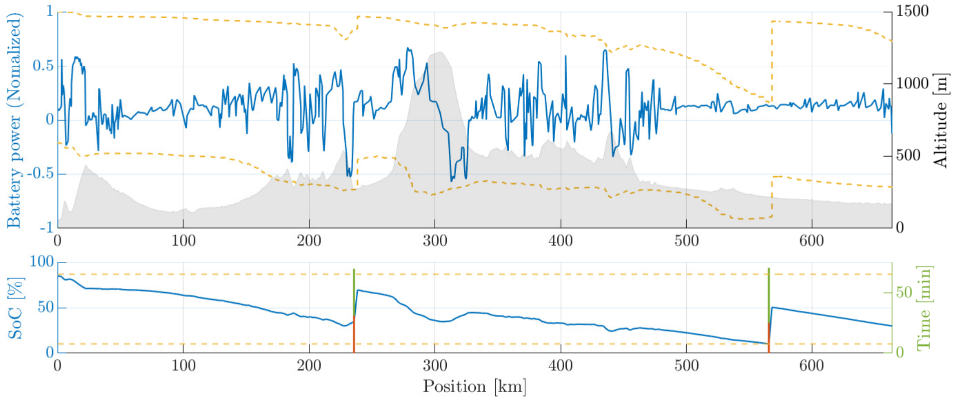

(c) Battery profile for a lower energy consumption.

Figure B.2: Battery power and SoC trajectories for the GK route. Sub figures **(a)**-**(c)** represent the disturbance cases a-c which are described in section 5.1. It is optimal to charge for 55.1, 47 respectively 38.9 minutes at station 10, where the queuing time is 36.47, 41.9 respectively 31 minutes, and for 43.3, 48.3 respectively 45.7 minutes at station 22, where the queuing time is 30, 35 respectively 25 minutes.

Moreover, figure B.3 illustrates the traction effort, friction brake usage, battery temperature, and battery heat flow for the simulations using the hierarchical solver.

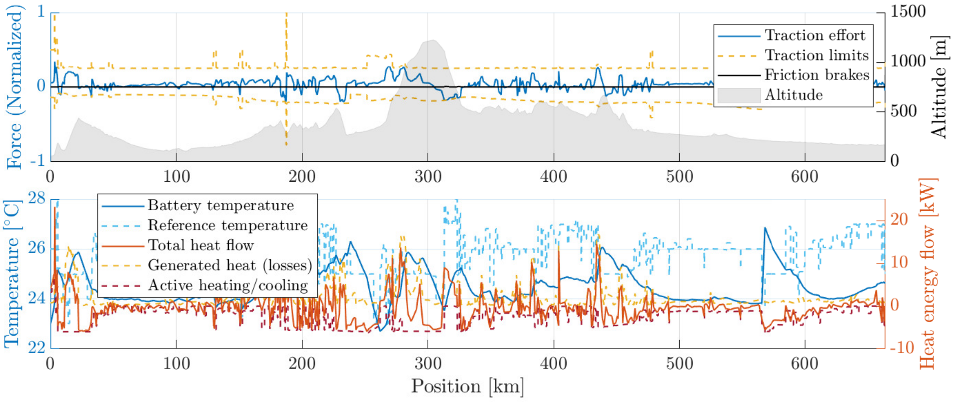

(a) Temperature profile using only the mean value as a disturbance.

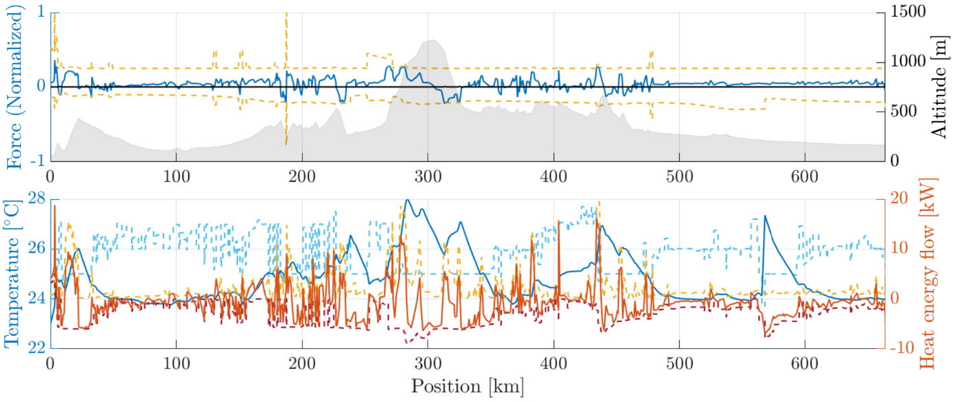

(b) Temperature profile for a higher energy consumption.

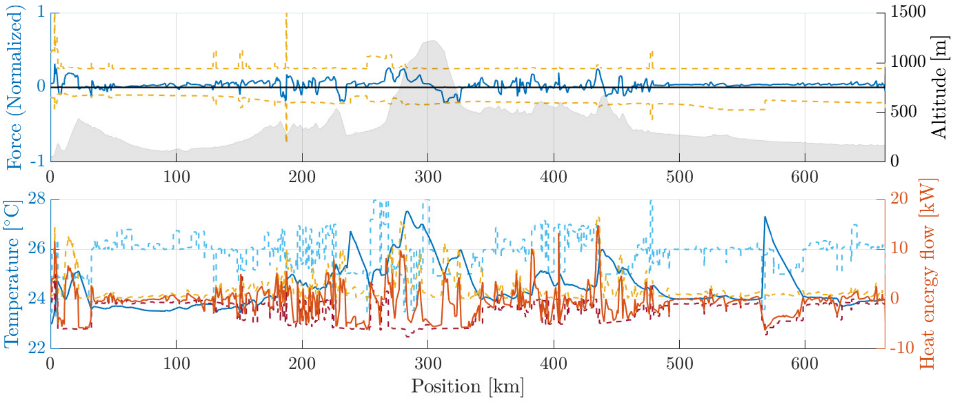

(c) Temperature profile for a lower energy consumption.

Figure B.3: Traction effort, friction brake usage, battery temperature, and heat flow for the GK route. It can be noted that the friction brake usage is minimal for this case and that the temperature is mostly kept around $24 - 25\,^\circ\mathrm{C}$. Sub figures **(a)**-**(c)** represent the disturbance cases a-c which are described in section 5.1.

Furthermore, figure B.4 shows the charging power and battery SoC and temperature profiles during charging for the different disturbance cases.

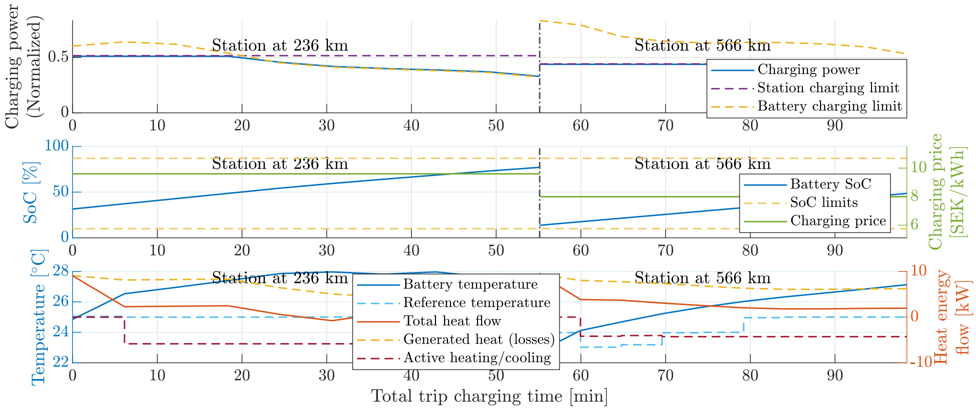

(a) Station profile using only the mean value as a disturbance.

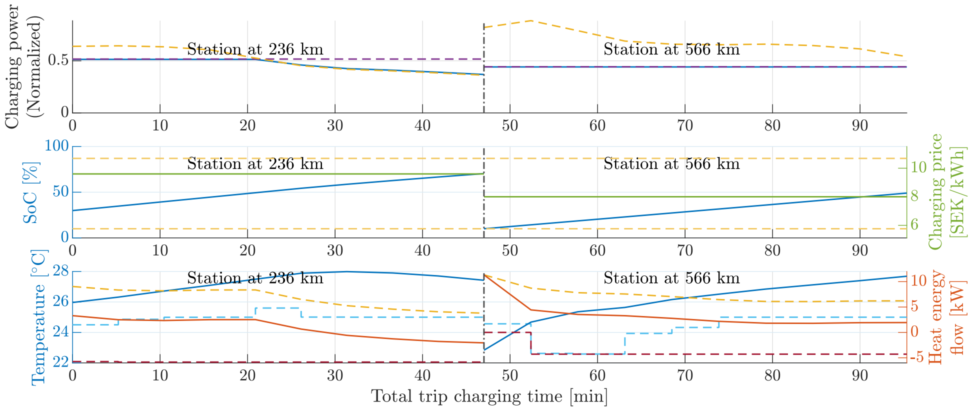

(b) Station profile for a higher energy consumption.

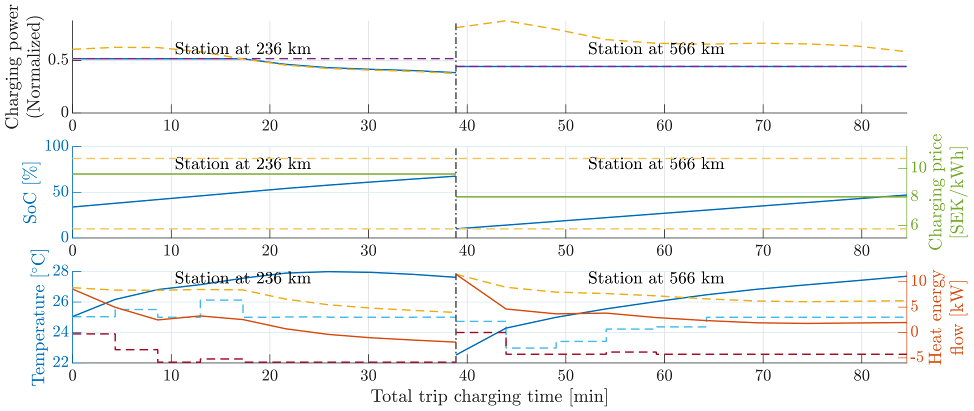

(c) Station profile for a lower energy consumption.

Figure B.4: Plots of the charging power, battery SoC, and temperature for the GK route. The plots are the state and input trajectories during charging at the selected stations at 236 and 566 km. Sub figures **(a)**-**(c)** represent the disturbance cases a-c which are described in section 5.1.

In figure B.5, the speed, battery, and temperature profiles using the sigmoid solution are plotted.

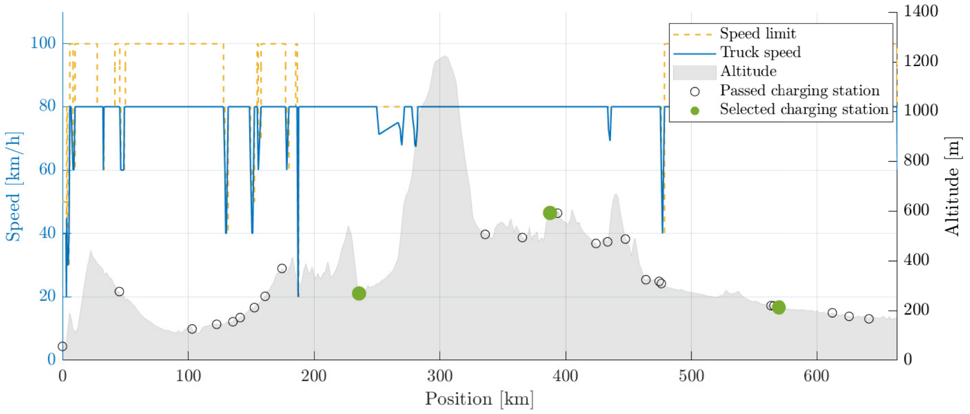

(a) Speed profile for the sigmoid solution.

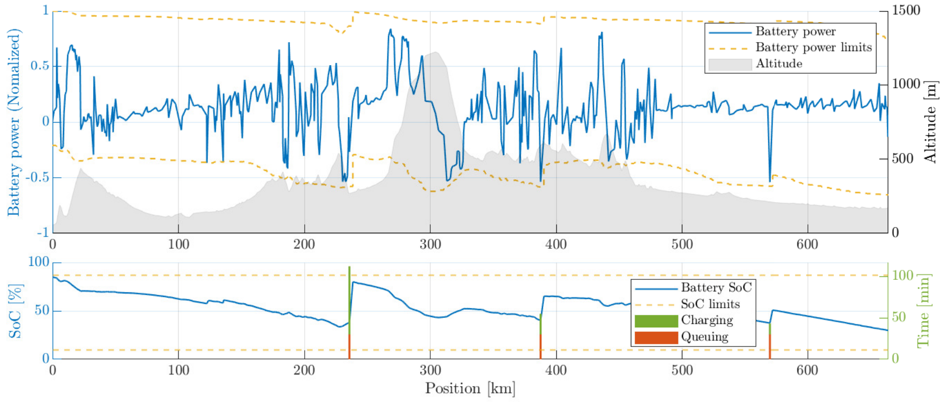

(b) Battery profile for the sigmoid solution.

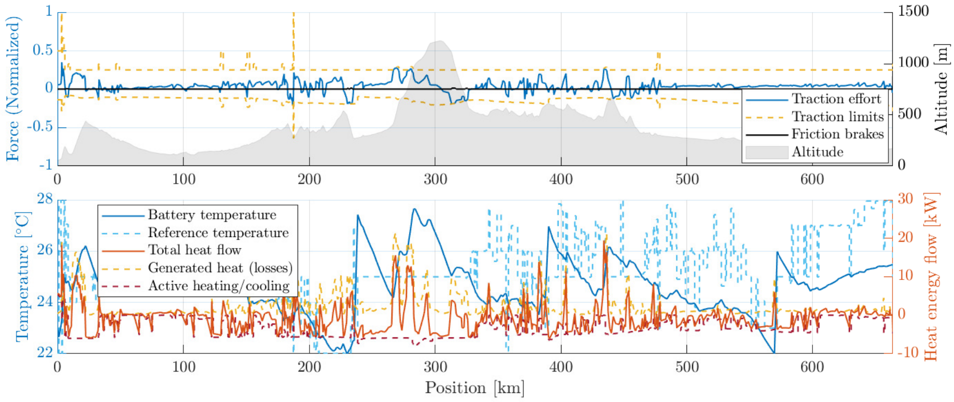

(c) Temperature profile for the sigmoid solution.

Figure B.5: Speed, battery, and temperature profiles for GK route using the sigmoid approximation to solve the problem. Note that the solution in this case is to instead charge for 82.4 minutes at station 10, 24.9 minutes at station 13 and 13.2 minutes at station 23.

Finally, figure B.6 shows the speed, battery, and temperature profiles found using the heuristics algorithm.

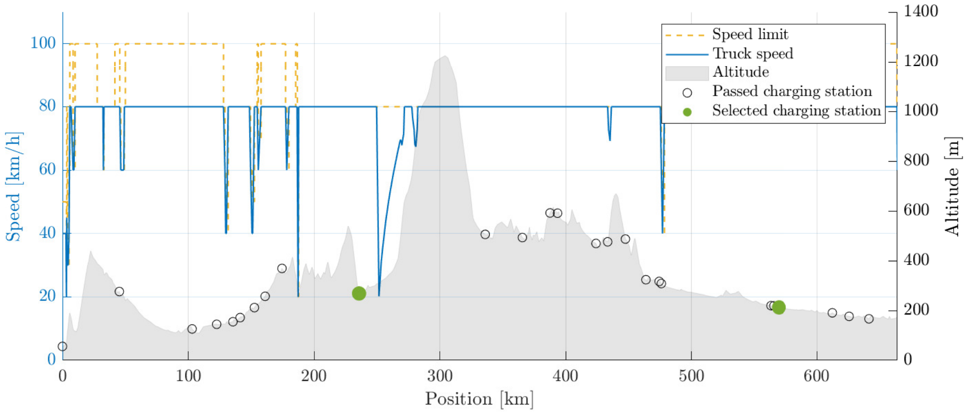

(a) Speed profile from using the heuristics algorithm.

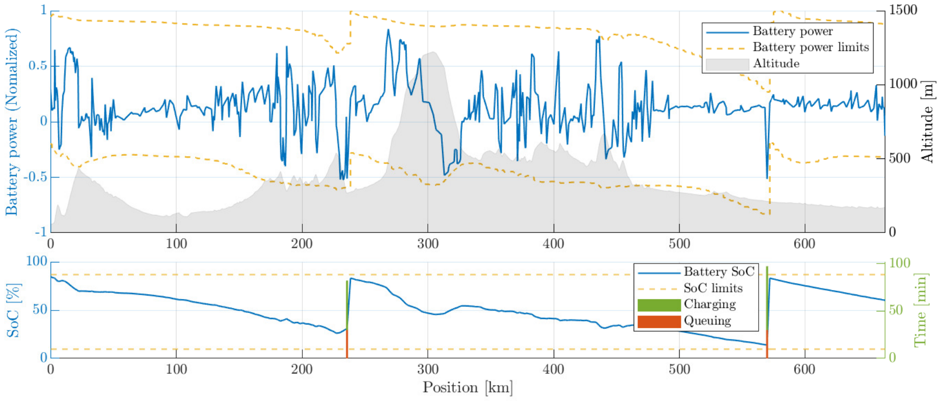

(b) Battery profile from using the heuristics algorithm.

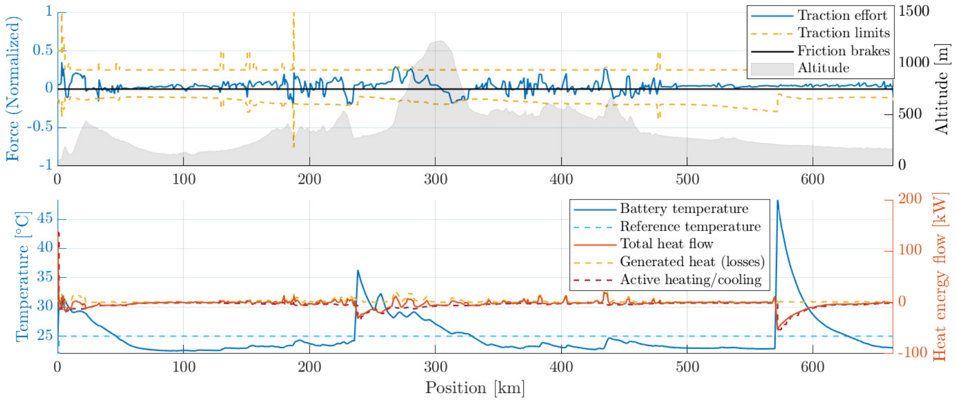

(c) Temperature profile from using the heuristics algorithm.

Figure B.6: Speed, battery, and temperature profiles for GK route using the heuristics algorithm to solve the problem. The suggested solution is to charge for 52.14 minutes at station 10 and for 67.6 minutes at station 23.

DEPARTMENT OF ELECTRICAL ENGINEERING
CHALMERS UNIVERSITY OF TECHNOLOGY
Gothenburg, Sweden
www.chalmers.se